Instability of flow around a rotating, semi-infinite cylinder in an axial stream

Srikanth Derebail Muralidhar

ÉCOLE CENTRALE LYON

N° d'ordre NNT: 2016LYSEC33

THÈSE de DOCTORAT DE L'UNIVERSITÉ DE LYON

opérée au sein de l'École centrale de Lyon

École doctorale 162
Mécanique, Énergétique, Génie civil, Acoustique

Spécialité de doctorat : Mécanique des fluides

Soutenue publiquement le 7 novembre 2016, par

Srikanth DEREBAIL MURALIDHAR

Instability of flow around a rotating, semi-infinite cylinder in an axial stream

---

Devant le jury composé de

François Gallaire	LMFI - École polytechnique fédérale de Lausanne	Rapporteur
Fabien Godeferd	LMFA - École centrale de Lyon	Président
Miguel Angel Herrada	University of Seville	Examinateur
Nigel Peake	DAMTP - Cambridge University	Rapporteur
Benoît Pier	LMFA - École centrale de Lyon	Directeur de thèse
Julian Scott	LMFA - École centrale de Lyon	Directeur de thèse

Abstract

This work concerns the steady, incompressible flow around a semi-infinite, rotating cylinder and its linear-stability properties. The effect of cylinder curvature and rotation on the stability of this flow is investigated in a systematic manner.

Prior to studying its stability, we first compute the basic flow. At large Reynolds numbers, a boundary layer develops along the cylinder. The governing equations are obtained using a boundary-layer approximation to the Navier–Stokes equations. These equations contain two non-dimensional control parameters: the Reynolds number (Re) and the rotation rate (S), and are numerically solved to obtain the velocity and pressure profiles for a wide range of control parameters. The initially thin boundary layer grows in thickness with axial distance, becoming comparable and eventually larger than the cylinder radius. Above a threshold rotation rate, a centrifugal effect leads to the presence of a wall jet for a certain range of streamwise distances. This range widens as the rotation rate increases. Furthermore, the wall jet strengthens as S increases. Asymptotic analyses of the flow at large streamwise distances and at large rotation rates are presented.

A linear stability analysis of the above flow is carried out using a local-flow approximation. Upon normal-mode decomposition, the perturbation equations are transformed to an eigenvalue problem in complex frequency (ω). The problem depends on five non-dimensional parameters: Re, S, scaled streamwise direction (Z), streamwise wavenumber (α) and azimuthal wavenumber m. The stability equations are numerically solved to investigate the unstable regions in parameter space. It is found that small amounts of rotation have strong effects on flow stability. Strong destabilization by small rotation is associated with the presence of a nearly neutral mode of the non-rotating cylinder, which becomes unstable at small S. This is further quantified using small-S perturbation theory. In the absence of rotation, the flow is stable for all Re below 1060, and for Z above 0.81. However, in the presence of small rotation, the instability becomes unconstrained by a minimum Re or a threshold in Z. The critical curves in the (Z, Re) plane are computed for a wide range of S and the consequences for stability of the flow described. Finally, a large-Z asymptotic expansion of the critical Reynolds number is obtained.

Résumé

Ce travail concerne l'écoulement incompressible et stationnaire autour d'un cylindre semi-infini en rotation, et ses propriétés de stabilité linéaire. L'effet de la courbure et de la rotation sur la stabilité de cet écoulement est étudié de manière systématique.

Avant d'étudier la stabilité, nous calculons d'abord l'écoulement de base. À grand nombre de Reynolds, une couche limite se développe le long du cylindre, ce qui permet d'utiliser l'approximation de couche limite des équations de Navier–Stokes. Ces équations dépendent de deux paramètres de contrôle sans dimension, le nombre de Reynolds (Re) et le taux de rotation (S), et sont résolues numériquement pour obtenir les profils de vitesse et de pression pour une large gamme des paramètres de contrôle. Une couche limite initialement mince s'épaissit avec la distance axiale; ainsi, son épaisseur devient comparable et finalement plus importante que le rayon du cylindre. Au-delà d'un certain taux de rotation, les effets centrifuges conduisent à un jet de paroi le long d'une portion du cylindre. L'extension axiale de ce jet augmente avec le taux de rotation. L'intensité du jet augmente aussi avec S. Des analyses asymptotiques de l'écoulement à grande distance axiale et à fort taux de rotation sont aussi présentées.

L'analyse de stabilité linéaire du précédent écoulement est effectuée dans l'approximation locale. Après une décomposition en modes normaux, les équations des perturbations sont transformées en un problème de valeur propre à fréquence complexe (ω). Ce problème dépend de cinq paramètres sans dimension: Re, S, la distance axiale normalisée (Z), le nombre d'onde axial (α) et le nombre d'onde azimutal (m). Les équations de stabilité sont résolues numériquement pour étudier les régions instables dans l'espace des paramètres. On observe que de faibles taux de rotation ont un effet important sur la stabilité de l'écoulement. Cette forte déstabilisation est associée à la présence d'un mode quasi-marginal pour le cylindre fixe et qui devient instable pour de petites valeurs de S. Ce phénomène est confirmé par une analyse en perturbation à petit S. Sans rotation, l'écoulement est stable pour tout $\mathrm{Re} < 1060$, et pour $Z > 0.81$. Mais, en présence d'une faible rotation, l'instabilité n'est plus limitée par une valeur minimale de Re ou un seuil en Z. Les courbes critiques dans le plan (Z, Re) sont calculées pour une large gamme de S et les conséquences pour la stabilité de l'écoulement discutées. Enfin, un développement asymptotique pour le nombre de Reynolds critique est obtenu, valable aux grandes valeurs de Z.

Acknowledgements

First and foremost, I owe my deepest gratitude to my supervisors, Julian Scott and Benoît Pier, without whom this thesis would have remained a dream. They have been extraordinarily supportive and tolerant. I am thankful to them for explaining to me the nuances of stability theory, boundary-layer theory and providing new perspectives on some general concepts of fluid mechanics. The regular meetings with them were useful to avoid getting stuck on technical difficulties, and the stiff deadlines resulted in the completion of this thesis almost on time (with just a delay of a month). They have always held me to a high research standard and taught me how to conduct a scientific study. Undoubtedly, these three years have been a great learning experience for me.

I would also like to express my gratitude to Rama Govindarajan for accepting me as a research assistant in Tata Institute of Fundamental Research (TIFR), where I undertook some preliminary studies of this problem. Frequent discussions with her were extremely useful in obtaining basic results, and further motivated me to undertake a doctoral study to explore this topic. It would be incomplete not to mention CEFIPRA, whose funding was significant for the short-term research project in TIFR, and later for covering the travel expenses of the European Fluid Mechanics Conference in Copenhagen.

I am thankful to the rapporteurs, Dr. Nigel Peake and Dr. François Gallaire, for having agreed to read and review this thesis. I hope it will be an interesting read, and I have tried my best to keep it short and informative. I am equally thankful in advance to the 'examinateur's, Dr. Miguel Angel Herrada and Dr. Fabien Godeferd, for agreeing to attend my 'soutenance' (thesis defence).

The laboratory of LMFA has definitely been a cradle of my research life. The regular seminars, group seminars, etc. from researchers from different universities as well from the lab have introduced me to new research topics. I am grateful to the administrative staff of the laboratory for their help with paperworks and organizing conference journeys. The bi-annual galas before the beginning of the summer and winter vacations truly are an unforgettable experience.

I thank all my friends from the laboratory, Donato, Robert, Pushkar, Quan, Baolin, Mathieu, Aleksandr, Dante, Kien, Annabelle and many more for interesting discussions on a variety of topics, ranging from politics to philosophy. I will always cherish the numerous outings with them such as Catan games, football matches, trying out different cuisines and exploring the night life in Lyon. I am also thankful to friends I met outside the laboratory such as Magali, Rony, Anastasia, Samuel, Jason, Guillaume and many more for the memorable times, and I greatly value their friendship. I equally thank Chakri, Shyam, Prabal, Aman, Nidhi, Rohini and Abhishek for keeping me in good spirits.

Finally, I am thankful to my immediate family for their continuous support during these three fruitful years. I hope their blessings will always be with me. I also thank my extended family for their encouragement throughout this endeavour.

Contents

Chapter 1

Introduction

Fluid flows are often classified as laminar or turbulent. Laminar flows are characterized by their orderliness, whereas turbulent flows have apparently random fluctuations in velocity and pressure. Flows often undergo a change of state from laminar to turbulent or vice-versa on changing flow parameters such as viscosity, velocity of the fluid, etc. This phenomenon is known as transition. Transition plays a crucial role in engineering applications that are based on, or strongly affected by fluid motions. For example, laminar flows produce less drag on a body, whereas turbulent flows are preferred in situations where mixing is important. Whether the desirable regime is laminar or turbulent, it is essential to understand the circumstances that govern transition. The first study of transition is traditionally attributed to Osborne Reynolds's famous experiment in 1883 on flow in a glass tube (Reynolds [1883]). The motion of the fluid was visualized by injecting a dye at the center of the pipe inlet. When the flow was laminar, the dye followed a straight-line path, whereas the path was irregular when the flow became turbulent. Reynolds also introduced an important non-dimensional parameter, subsequently named after him, $\mathrm{Re} = Ul/\nu$, where ν is the kinematic viscosity of the fluid and U and l are the characteristic velocity and length scales of the flow. Turbulence only occurs at large Reynolds number, the flow being laminar at small and moderate Re, before becoming turbulent above a certain transitional value.

The mechanisms inducing transition are complex and not yet fully understood. However, it is generally believed to be due to instability of the laminar flow. Instability means that small perturbations (for instance, coming from upstream, wall vibration, etc.) to a given solution of the governing equations, known as the basic flow, spontaneously grow, so that the basic flow is not realized in practice. At small Re, the flow which is realized has particularly simple properties, e.g. it is steady and possesses the spatial symmetries of the underlying flow geometry. This flow generally becomes unstable above a certain Re and is replaced by another, more complex, flow. The resulting change in flow regime may, for instance, be steady $\rightarrow$ unsteady and/or break one or more of the underlying spatial symmetries. In some flows, e.g. the pipe flow studied by Reynolds, the first instability leads directly to turbulence, whereas in others the result is a more complex laminar flow. In that case, the new flow can be taken as the basic flow and the question of its stability addressed. Possibly crossing several instability thresholds, at each of which there is a change in flow regime, transition to turbulence generally occurs at large enough Re.

The classical approach to stability analysis, namely linear theory, applies when the flow perturbation is sufficiently small. Equations governing the perturbation are derived by subtracting the Navier–Stokes equations for the basic flow from those for the perturbed flow. The perturbation equations contain a nonlinear term, which makes their solution by other than di-

rect numerical simulation unfeasible. Linear theory drops the nonlinear term, which opens up an armoury of mathematical tools for stability analysis, e.g. modal decomposition, eigenvalue problems for determination of flow stability, etc. One can then study the stability boundary in flow-parameter (Re and any other non-dimensional control parameters) space. One can also study the mechanism of instability by identifying the mode responsible for destabilization of the basic flow. Of course, when instability occurs, linear theory cannot tell us the final result of growth of the perturbation because it will lie outside the regime of small perturbations for which linear theory holds. Linear theory provides a first step in a stability analysis, usually to be followed by direct numerical simulations of the Navier–Stokes equations. The problem is that, at the large Reynolds numbers typical of instability, numerical simulations are computationally costly, particularly as searching flow-parameter space for different flow regimes requires many such simulations. Linear theory acts as a guide to interesting regions of parameter space and to the types of instabilities to be expected. There are, however, flows, such as the circular-pipe flow studied by Reynolds, for which linear theory predicts that the flow is always stable. For such flows, the observed instability requires nonlinearity.

Boundary layers arise in high-Reynolds number flows over solid surfaces. They are characterized by a thin layer near the surface in which viscosity is important and slows the fluid by viscous friction with the wall. Thinness of the layer means that the length scale for variation along the surface is large compared with that perpendicular to the wall. This disparity of scales allows approximation (the boundary-layer approximation) of the Navier–Stokes equations in which certain terms are neglected because they are small compared with the others. The resulting equations are variously known as the Prandtl (who first developed boundary-layer theory) or boundary-layer equations. These equations have been extensively applied to various flows to determine quantities such as skin friction, heat-transfer coefficient, etc.

Stability of laminar boundary layers over various types of bodies has been extensively studied to understand the growth mechanisms and possible transition paths. This is due to their importance in the design of blades and vanes of turbomachinery, land and marine vehicles, wings of aircraft, etc. The sheer complexity of the geometry in these examples makes it hard to study their stability properties in detail and simplified flows are often used as a model. The results for such relatively simple flows illustrate the interplay of physical mechanisms determining the stability of boundary-layer flows having more complex geometries.

The classical example of a laminar boundary layer is the steady flow over a flat plate which is placed in a uniform, incompressible flow with no external pressure gradient. This flow is also known as the Blasius boundary layer. Linear stability analysis of this flow was undertaken by Walter Tollmien [1928] and Hermann Schlichting [1933] to obtain the fundamental two-dimensional modes, also known as Tollmien–Schlichting (T-S) waves, which control stability according to linear theory. The Blasius boundary layer serves as a reference problem for more general boundary-layer flows due to the simplicity of the problem. Flows with additional physical effects such as rotation, stratification, external pressure gradient, etc. are often compared with the Blasius case to identify the role of such effects on the stability properties.

In this thesis we study the linear stability of the steady, axisymmetric, boundary-layer flow that develops around a semi-infinite, rotating cylinder placed in a uniform, incompressible, axial flow at large Reynolds number. The development of such a boundary layer is influenced by two important physical properties: the curvature of the cylinder and rotation, thereby being rendered more complex than the Blasius boundary layer. These two effects have often been studied separately in the literature. Examples of boundary layers over curved surfaces include flow over a concave wall, flow around a sphere, yawed cylinder, etc., and the different kinds of instability modes developing in such flows are well-documented (see the review articles of Reed *et al.* [1996] and Reed & Saric [1989] for details). Flow over a rotating disk represents a rotating

flow without curvature effects, and its instability has been well-studied, see e.g. Lingwood [1995], Pier [2007]. Flows over surfaces with both rotation and curvature include flow around a rotating sphere (Pier [2013]), rotating cones (Garrett *et al.* [2010]), rotating cylinder, etc. However, the flow over a rotating cylinder is perhaps the simplest case of a boundary layer influenced by both curvature and rotation, and is therefore of fundamental interest.

The rotating-cylinder flow also has practical applications. It can be used as a model to describe the flow around rotating arrows and rotating projectile-shaped objects. Towed sonar arrays, which are used in underwater sensing, can also be described using the non-rotating cylinder problem. More generally, it can be used as a simplified model to understand the stability properties of curved axisymmetric objects which may be rotating. This encompasses several practical flows such as turbine blades, helicopter wings, rockets, etc.

1.1 Problem description

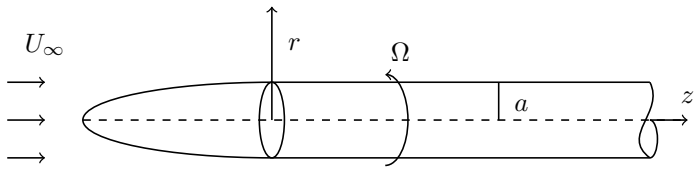

Figure 1.1: Schematic illustration of the problem.

Figure 1.1 illustrates flow around a rotating semi-infinite cylinder. The angular velocity at which the cylinder rotates is denoted by Ω, the fluid viscosity by ν, and the density of the fluid by ρ. The velocity in the free stream is denoted by U_∞. The governing equations of the flow are the incompressible Navier–Stokes equations written in cylindrical coordinates (r, z, θ). The following scales are used to non-dimensionalize the equations: lengths using the cylinder radius a, velocities using U_∞, time using a/U_∞ and pressure differences using ρU_∞^2.

The cylinder is preceded by a smooth nose in order to avoid the flow separation which would occur if the cylinder was sharply truncated. In this study we will see that the effect of the nose on the dynamics of the flow along the cylinder is negligible, except in a relatively small region close to the nose (at streamwise distances comparable to the radius). Non-dimensionalization results in two important control parameters, namely the Reynolds number (Re) and rotation rate (S), which are defined as

$$\mathrm{Re} = \frac{U_\infty a}{\nu}, \tag{1.1}$$

$$S = \frac{\Omega a}{U_\infty}. \tag{1.2}$$

As usual, the Reynolds number measures the importance of inertial forces compared with viscous forces, whereas the rotation rate compares the cylinder rotational velocity to the free-stream velocity.

1.2 Literature review

1.2.1 Basic-flow studies

Early work on the basic flow over a semi-infinite cylinder (which may or may not be rotating) involved formulating the governing equations using a boundary-layer approximation and obtaining an analytical approximate solution to these equations. Seban & Bond [1951] obtained the solution for the non-rotating problem using a power series in $z^{\frac{1}{2}}$, where z is the streamwise coordinate. At leading order, they recovered the Blasius solution which describes the flow over a flat plate. This is due to the fact that as z tends to 0, the boundary layer becomes thin in comparison to the cylinder radius and the curvature effects of the cylinder are negligible. Thus, the Blasius flow is to be expected near the inlet. Seban & Bond [1951] also computed the next two terms of the series solution, which are sufficient to describe the flow near the inlet. The corresponding velocity profiles had small deviations from the Blasius solution. As only the first three terms were considered, the solution ceased to be valid as z was increased to larger values due to the significance of higher-order terms. They also provided series solution for quantities such as the displacement thickness and skin-friction coefficient. Note however that Kelly [1954] showed that the coefficients in the series solution of displacement thickness were erroneous and computed the correct coefficients.

Glauert & Lighthill [1955] used the Pohlhausen method to obtain an approximate solution which was valid for values of z larger than those obtained by Seban & Bond [1951]. They further developed an asymptotic series solution in inverse powers of $\log z$ to describe the flow at large z. The boundary-layer equations for the non-rotating problem were numerically solved for the first time by Jaffe & Okamura [1968] to obtain the velocity profiles along with quantities such as skin-friction coefficient and displacement thickness for a range of values of z. Their results showed good agreement with those of Glauert & Lighthill [1955]. Cebeci [1970] and Sawchuk & Zamir [1992] used different numerical methods to obtain accurate solutions at values of z larger than Jaffe & Okamura [1968]. Sawchuk & Zamir [1992] solved the equations using the Keller–Box method (developed by Keller & Cebeci [1972]) to obtain numerical results for z up to 10^6 and their results were in good agreement with the asymptotic approximations of Glauert & Lighthill [1955].

The case of the rotating cylinder has received less attention in the literature than it probably merits. To the best of our knowledge, Petrov [1976] appears to be the first to conduct some preliminary studies of this flow. The boundary-layer equations were simplified by assuming that the boundary-layer thickness is small in comparison to the cylinder radius. Thus, the results are applicable only in a region close to the inlet of the cylinder. Velocity profiles were obtained by numerically solving these equations using the method of finite differences. One of the interesting results in Petrov [1976] is the plot of streamwise velocity profiles for large values of rotation rate S which show a non-monotonic behaviour, with the maximum velocity occurring near the cylinder surface. The profiles qualitatively correspond to those observed in a planar wall-jet flow (as studied by Glauert [1956]), though this phenomena was not highlighted nor explained in the paper. Herrada *et al.* [2008] solved the boundary-layer equations for the rotating case without assuming small boundary-layer thickness, but the values of rotation rate covered by them (S between 0 and 1) are not large enough to see the wall-jet behaviour. Furthermore, there are no studies of the asymptotic behaviour at large values of z (similar to that of Glauert & Lighthill [1955] for non-rotating case) or at large values of S for the rotating-cylinder case. This motivated us to conduct a systematic study of the boundary-layer flow along a rotating cylinder. One of the goals of this thesis is to characterize the wall-jet behaviour, and to understand the effect of changing z or S on the wall jet. This study further aims to provide the asymptotic solution at

large values of z and S, thereby providing a complete parametric study of the steady flow over a rotating cylinder.

1.2.2 Stability studies

As mentioned earlier, the linear stability of the Blasius boundary layer, which is the limiting case of $z \to 0$ of the cylinder problem, was studied by Tollmien [1928] and Schlichting [1933]. They computed the fastest growing mode, which is a two-dimensional wave-like perturbation known as the Tollmien–Schlichting (T-S) mode. Linear theory was further used to compute the critical value of the Reynolds number above which the flow becomes unstable. Mack [1976] numerically solved the stability equations of the Blasius boundary layer to obtain modes other than the T-S mode. For the Blasius case, Squire's theorem (see Drazin [2002]) guarantees that two-dimensional modes are the first to become unstable on increasing the Reynolds number.

The non-rotating cylinder was studied by Tutty *et al.* [2002], who found that the flow is stable for Reynolds numbers below 1060, and that nonaxisymmetric modes are the first to become unstable on increasing Re above this value. This reflects the fact that there is no equivalent of Squire's theorem for the cylinder problem. Another interesting feature of the non-rotating cylinder case is that above the critical Re of 1060, the flow is unstable only for a finite range of z. Secondary stability of the non-rotating case was studied by Vinod & Govindarajan [2012].

Linear stability analysis of the rotating cylinder problem was first studied by Kao & Chow [1991]. However, their basic-flow equations are erroneous and their results for the non-rotating case do not agree with those of Tutty *et al.* [2002]. Herrada *et al.* [2008] solved the correct equations and obtained stability results for a range of rotation rate between $0.1 - 1$. Their results indicate that the rotating cylinder becomes unstable at lower values of Re than the non-rotating case at each z. The critical curves which separate the stable region from the unstable region in the (Z, Re) plane, where $Z = z/\mathrm{Re}$, were observed to be monotonically decreasing for the range of physical parameters covered in their study. This poses a crucial question: Are the critical curves monotonically decreasing even when Z is increased to values larger than those covered in Herrada *et al.* [2008], or is there a value of Z beyond which the flow is stable for all values of Re? This brings us to another important goal of this thesis, which is to conduct a systematic investigation of the linear stability of the rotating-cylinder flow, including a larger range of rotation rates and streamwise distances than those covered by Herrada *et al.* [2008]. Studying the range $S < 0.1$ might provide clues on how the flow changes from being stable to unstable at large Z on introduction of rotation. The study of $S > 1$ is also worth exploring as we know from Petrov [1976] that a wall jet can appear.

1.2.3 Experimental work

The Blasius boundary layer was experimentally studied by Schubauer & Skramstad [1948], in which the two-dimensional T-S mode predicted by linear stability theory was first observed. Figure 1.2 shows an example of visualization of a T-S wave growing along a flat plate in a different experiment by Werle [1970] at ONERA. Thus linear theory is useful in predicting the initial structure and the rate of amplification of the modes. The T-S mode eventually becomes unstable to secondary disturbances further downstream, leading to the formation of vortex patterns that break down to turbulent spots on further increasing streamwise distance.

There are only a handful of experimental studies on the rotating cylinder in the literature. The most notable work is that of Kegelman *et al.* [1983], who studied flow around a rotating body consisting of a secant-ogive nose followed by a cylindrical section which ends with a boat tail (see figure 1.3). The length of the cylindrical section, non-dimensionalized using the radius, was

Figure 1.2: a) Flow visualization of the T-S mode on a flat plate.

around 0.98. Experiments were conducted for S between $0-2$ and Re of the order of 10^6. Flow visualizations were provided for various values of the rotation rate showing different instability modes that developed along the cylinder section. For the non-rotating cylinder, figure 1.3a shows

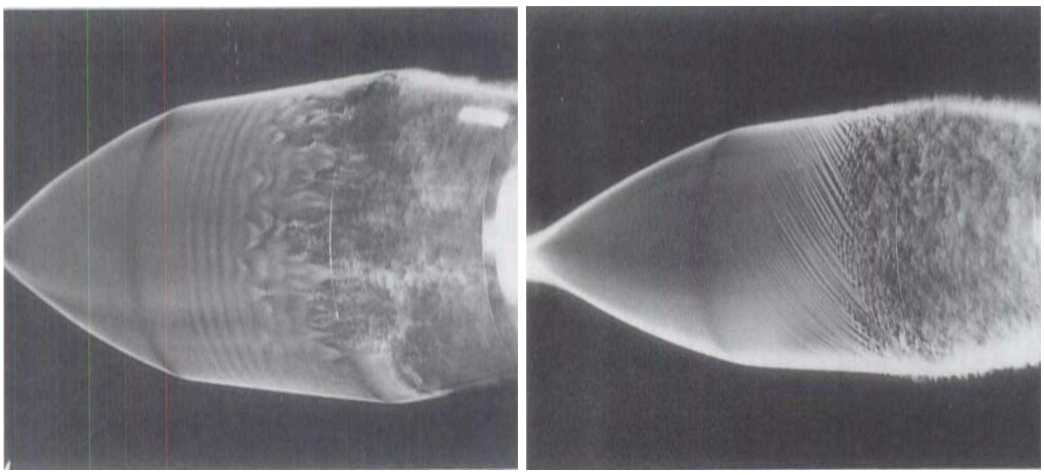

(a) (b)

Figure 1.3: Visualization of instability modes at a) $\mathrm{Re} = 4.18 \times 10^6$ for the non-rotating case, b) at $\mathrm{Re} = 1.26 \times 10^6$ and $S = 0.848$ by Kegelman *et al.* [1983].

the presence of an axisymmetric T-S wave at $\mathrm{Re} = 4.18 \times 10^6$. The T-S wave changes into a vortex-truss pattern and eventually the flow breaks down to turbulence as streamwise distance increases. Figure 1.3b shows a visualization of instability when $S = 0.848$ and $\mathrm{Re} = 1.26 \times 10^6$, where spiral waves are observed to develop striations as z is increased. This kind of instability is known as a cross-flow instability and occurs in swept-wing and rotating-disk flows. These cross-flow modes eventually break down and the flow becomes fully turbulent further downstream. The two figures show that rotation plays an important role in the stability of the flow. However, these

experimental results are not quantitatively comparable with our theoretical ones for two reasons. Firstly, as noted earlier, the flow is sensitive to the nose geometry at distances comparable to the cylinder radius. Such details are forgotten at larger streamwise distances and it is this region we will focus on. The cylinder length in the experiments being comparable with its radius, comparison with our results is inappropriate. The second difference is that the experimental Reynolds numbers are much higher than those we study.

Other experimental studies of the rotating cylinder include the work of Sawada *et al.* [2012], who studied overall aerodynamic properties, such as the coefficients of drag and lift, of rotating archery arrows. Most professional arrows have vanes (helical fletching) which induces rotation of the arrow as it travels forward. Such rotating arrows provide examples of long, thin, rotating cylinders. Sawada *et al.* [2012] studied two different nose shapes: a sharp pointed nose and a bullet shaped nose, at different Reynolds numbers. The aerodynamic properties were found to be little affected by the shape of the nose over the parameter range considered in their study. A similar study was conducted by Miyazaki *et al.* [2013]. However, neither paper gives details of the flow or its instability properties and these papers are thus of less relevance to the present study than Kegelman *et al.* [1983].

1.3 Organization of the thesis

The rest of this thesis is structured in the following manner. The boundary-layer approximation is discussed in chapter 2 using examples of a two-dimensional planar surface and the semi-infinite, rotating-cylinder problem which is the object of this thesis. The methodology involved in the derivation of the linear stability equations will be discussed in chapter 3. The technique of local approximation is also explained in that chapter, and is crucial in developing the linear stability equations for a slowly-evolving (in z) flow such as the rotating-cylinder flow. Following these two introductory chapters, the numerical techniques used to solve the basic-flow and stability equations are explained in chapter 4. That chapter concludes with the results of various checks and validations that were performed to test the numerical implementation.

The main findings of this dissertation are presented in chapters 5 and 6 in the form of two articles: chapter 5 published in Proceedings of the Royal Society of London A (Derebail Muralidhar *et al.* [2016b]), chapter 6 published in Physical Review Fluids (Derebail Muralidhar *et al.* [2016a]). The results concerning the basic flow are presented in chapter 5. That article also discusses the asymptotic analysis at large values of Z and S. The results of the linear stability analysis are presented in chapter 6. In particular, critical curves for different values of S are presented, and the effects of very low rotation rates on the critical curves are discussed. The chapter also provides a scaling law for the behaviour of the critical curves at sufficiently large values of streamwise distances.

The results of both the articles are summarized in chapter 7. That chapter also discusses possible directions for future work.

Chapter 2

Boundary-layer approximation

In this chapter we review the concepts of boundary-layer theory, the basic assumptions used in deriving the boundary-layer equations, and their application in two specific cases of interest. Classical Prandtl theory and the boundary-layer approximation are explained using the example of a steady, two-dimensional boundary layer over a plane surface. The Blasius boundary layer is then discussed as a special case in which the outer flow is uniform. The boundary-layer approximation is also described for a rotating/non-rotating body of revolution and the case of rotating-cylinder flow. The discussion is based on the classical texts on boundary-layer theory by Schlichting [1979], Batchelor [1967] and Rosenhead [1963].

2.1 2-D boundary layer over a plane surface

The principal notion behind boundary-layer theory is that, at high Reynolds number, flow around a body can be divided into two regions: a thin region close to the surface of the body, known as the boundary layer, where the viscosity of the fluid cannot be neglected, and the region outside the boundary layer where the fluid behaves as if it were inviscid (Prandtl [1904]). This is also known as Prandtl theory. At the surface of the body, the fluid must satisfy a no-slip condition, i.e. the relative velocity between the fluid and the body is zero. This gives rise to a boundary layer which can be thought of as a region in which the flow is slowed as a result of viscous friction and the no-slip condition at the surface. In the outer region, the flow is described using inviscid equations. In the boundary layer, the importance of viscous diffusion can be expected to be comparable to convection. The governing equations of the flow in the boundary layer are derived by making an approximation to the Navier–Stokes equations, known as boundary-layer approximation. This approximation relies on the assumption that the boundary layer is thin in comparison to the length scale for streamwise development.

To illustrate the boundary-layer approximation, let us consider two-dimensional steady flow of incompressible fluid having viscosity ν and density ρ over a plane surface. Cartesian coordinates (x, y) are adopted to describe this system, where x means distance along the surface (the streamwise direction) and y is distance from the surface. Let L denote a length scale characteristic of streamwise development and δ the boundary-layer thickness, which is much smaller than L according to Prandtl theory (see figure 2.1). Thus, the basis of the boundary-layer approximation is the assumption that $\delta \ll L$.

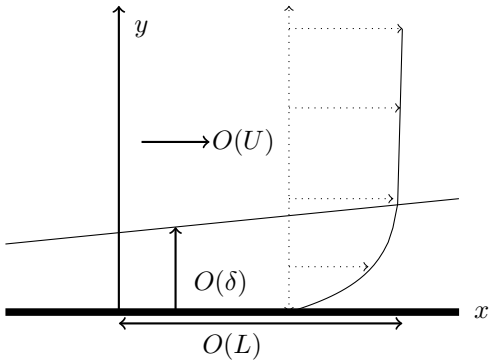

Figure 2.1: Schematic representation of a 2−D boundary layer on a planar surface, showing order-of-magnitude scales and a velocity profile. Note that the boundary-layer thickness has been exaggerated to make it visible. In reality, we require $\delta \ll L$.

The equations of motion are

$$u_x\frac{\partial u_x}{\partial x}+u_y\frac{\partial u_x}{\partial y}=-\frac{1}{\rho}\frac{\partial p}{\partial x}+\nu\left(\frac{\partial^2 u_x}{\partial x^2}+\frac{\partial^2 u_x}{\partial y^2}\right), \tag{2.1}$$

$$u_x\frac{\partial u_y}{\partial x}+u_y\frac{\partial u_y}{\partial y}=-\frac{1}{\rho}\frac{\partial p}{\partial y}+\nu\left(\frac{\partial^2 u_y}{\partial x^2}+\frac{\partial^2 u_y}{\partial y^2}\right), \tag{2.2}$$

$$\frac{\partial u_x}{\partial x}+\frac{\partial u_y}{\partial y}=0, \tag{2.3}$$

where u_x and u_y are the velocity components and p is the pressure. The following order-of-magnitude estimates are employed:

$$u_x=O(U),\quad \frac{\partial}{\partial x}=O(L^{-1}),\quad \frac{\partial}{\partial y}=O(\delta^{-1}), \tag{2.4}$$

where U is an order-of-magnitude scale characterising the streamwise velocity. Using (2.4) in the incompressibility condition (2.3) gives

$$u_y=O(\frac{\delta}{L}U). \tag{2.5}$$

Thus, the streamwise velocity component, u_x, is dominant since $\delta/L \ll 1$. Employing (2.4) and (2.5) to estimate the order of magnitudes of terms in equation (2.1),

$$\underbrace{u_x\frac{\partial u_x}{\partial x}}_{U^2/L}+\underbrace{u_y\frac{\partial u_x}{\partial y}}_{U^2/L}=-\frac{1}{\rho}\frac{\partial p}{\partial x}+\underbrace{\nu\frac{\partial^2 u_x}{\partial x^2}}_{\nu U/L^2}+\underbrace{\nu\frac{\partial^2 u_x}{\partial y^2}}_{\nu U/\delta^2}. \tag{2.6}$$

Comparing the two viscous terms in equation (2.6), we see that the first is $O(\delta^2/L^2)$ smaller than the second and is thus neglected. Balancing the convective and viscous terms in equation (2.6) gives

$$\left(\frac{\delta}{L}\right)^2=O(\frac{\nu}{UL}), \tag{2.7}$$

$$\frac{\delta}{L}=O(\mathrm{Re}^{-1/2}), \tag{2.8}$$

where $\mathrm{Re} = UL/\nu$ represents the Reynolds number. This indicates that the assumption, $\delta/L \ll 1$, used in boundary-layer approximation, is valid when Re is sufficiently large. Balancing the pressure gradient terms gives the scaling of pressure variations as

$$p = O(\rho U^2). \tag{2.9}$$

Order-of-magnitude estimates of each term in equation (2.2) can be obtained using (2.4), (2.5) and (2.9):

$$\underbrace{u_x \frac{\partial u_y}{\partial x}}_{\delta U^2/L^2} + \underbrace{u_y \frac{\partial u_y}{\partial y}}_{\delta U^2/L^2} = -\underbrace{\frac{1}{\rho}\frac{\partial p}{\partial y}}_{U^2/\delta} + \underbrace{\nu \frac{\partial^2 u_y}{\partial x^2}}_{\nu\delta U/L^3} + \underbrace{\nu \frac{\partial^2 u_y}{\partial y^2}}_{\nu U/\delta L}. \tag{2.10}$$

Comparison of terms and using (2.7) shows that $\partial p/\partial y$ dominates the others by a factor of L^2/δ^2.

Thus, the final boundary-layer equations are

$$u_x \frac{\partial u_x}{\partial x} + u_y \frac{\partial u_x}{\partial y} = -\frac{1}{\rho}\frac{\partial p}{\partial x} + \nu \frac{\partial^2 u_x}{\partial y^2}, \tag{2.11}$$

$$\frac{\partial p}{\partial y} = 0, \tag{2.12}$$

$$\frac{\partial u_x}{\partial x} + \frac{\partial u_y}{\partial y} = 0. \tag{2.13}$$

These equations are also known as the Prandtl equations and describe the leading-order behaviour of the flow variables when appropriate boundary conditions are applied. In fact, this procedure yields the first term in an asymptotic expansion in powers of $\mathrm{Re}^{-\frac{1}{2}}$.

The boundary conditions come from the no-slip condition and matching to the outer (inviscid) flow:

$$u_x = 0, u_y = 0 \quad y = 0, \tag{2.14}$$

$$u_x \to U(x), p \to P(x) \quad y \to \infty, \tag{2.15}$$

where $U(x)$ and $P(x)$ represent the velocity and pressure just outside the boundary layer (more precisely, the $y \to 0$ limit of the inviscid flow). An initial condition for u_x must also be specified at some location x_0 (usually referred to as the inlet condition). The boundary-layer equations require less boundary conditions, in particular no outlet conditions, than the original Navier–Stokes equations. This is due to the parabolic nature of the boundary-layer equations.

Using equation (2.12), (2.15) and Bernoulli's theorem applied to the inviscid flow along the surface streamline leads to

$$\frac{\partial p}{\partial y} = 0 \implies p = p(x) = P(x), \tag{2.16}$$

$$-\frac{1}{\rho}\frac{\partial p}{\partial x} = -\frac{1}{\rho}\frac{\mathrm{d}P}{\mathrm{d}x} = U\frac{\mathrm{d}U}{\mathrm{d}x}. \tag{2.17}$$

Thus, pressure is eliminated from the boundary-layer equations, which become

$$u_x \frac{\partial u_x}{\partial x} + u_y \frac{\partial u_x}{\partial y} = U\frac{\partial U}{\partial x} + \nu \frac{\partial^2 u_x}{\partial y^2}, \tag{2.18}$$

$$\frac{\partial u_x}{\partial x} + \frac{\partial u_y}{\partial y} = 0, \tag{2.19}$$

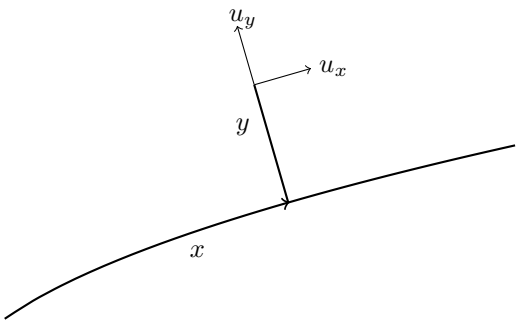

Figure 2.2: Curvilinear coordinates and associated velocity components.

with the boundary conditions

$$u_x = 0, u_y = 0 \quad y = 0, \tag{2.20}$$

$$u_x \to U(x) \quad y \to \infty, \tag{2.21}$$

and the inlet condition, which specifies $u_x(y)$ at x_0. If the inlet profile and $U(x)$ are given, the above boundary-value problem determines the flow within the boundary layer. In addition to its influence on the number and type of boundary conditions, the parabolic character of the boundary-layer equations means that they can only be stably integrated in the direction of the streamwise flow. This creates problems in cases where $u_x(y)$ changes sign at fixed x, because there is then no stable direction for integration. This is the case in the presence of boundary-layer separation, to which, following separation, the boundary-layer approximation can no longer be applied. This is the main limitation on boundary-layer theory.

The restriction to a planar surface, used here for simplicity's sake, is in fact unnecessary, provided that the coordinates x and y are taken to be curvilinear and defined as shown in figure 2.2. For any given point near the surface, x is distance along the surface of the point nearest the given one and y is the distance from the surface. Equations (2.18)–(2.21) continue to hold.

We have assumed the flow to be two-dimensional. Various generalizations can be made, e.g. flow over axisymmetric body of revolution (a case we will discuss later) or more general three-dimensional flows. Approximations of boundary-layer type can also be used in cases where there is no solid boundary, e.g. jets and wakes. The important requirement is that there is a direction (or directions) in which the scale for spatial variation is much smaller than for other directions. This allows approximation of the full equations of motion using order-of-magnitude arguments.

2.1.1 Blasius boundary layer

Perhaps the best known case is flow over a semi-infinite flat plate placed in a uniform stream of fluid of velocity U_∞, parallel to the plate (see figure 2.3). The plate is of negligible thickness and occupies the region $x > 0$, $y = 0$ of the x-axis. The incident flow is $(U_\infty, 0, 0)$. At distances, x, from the leading edge such that the Reynolds number, $\mathrm{Re}_x = U_\infty x/\nu$, is large, the boundary layer is thin compared with x and the boundary-layer equations hold. Because $U(x) = U_\infty$ is

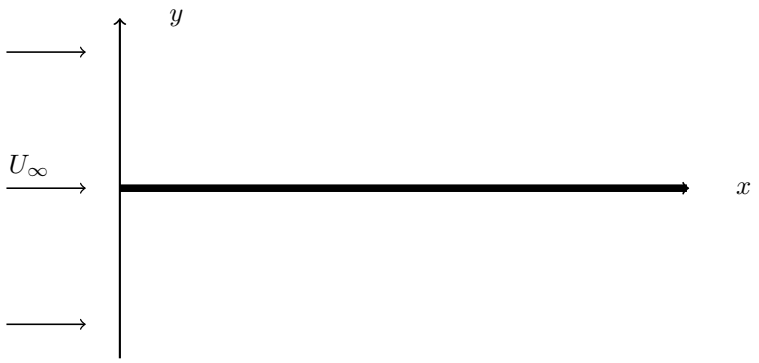

Figure 2.3: Illustration of the Blasius problem.

constant, the problem is governed by

$$u_x \frac{\partial u_x}{\partial x} + u_y \frac{\partial u_x}{\partial y} = \nu \frac{\partial^2 u_x}{\partial y^2}, \tag{2.22}$$

$$\frac{\partial u_x}{\partial x} + \frac{\partial u_y}{\partial y} = 0, \tag{2.23}$$

$$u_x = 0, u_y = 0 \quad x > 0, y = 0, \tag{2.24}$$

$$u_x \to U_\infty \quad x > 0, y \to \infty. \tag{2.25}$$

and the inlet condition

$$u_x = U_\infty \quad x = 0. \tag{2.26}$$

This problem was addressed by Blasius, who showed that it has the similarity solution (see Batchelor [1967]),

$$u_x = U_\infty f'(\eta), \quad u_y = \frac{1}{2}\left(\frac{\nu U_\infty}{x}\right)^{\frac{1}{2}} (\eta f' - f), \tag{2.27}$$

where

$$\eta = \left(\frac{U_\infty}{\nu x}\right)^{\frac{1}{2}} y, \tag{2.28}$$

and the function $f(\eta)$ is the solution of

$$f''' + \frac{1}{2} f f'' = 0, \tag{2.29}$$

with the boundary conditions

$$f(0) = f'(0) = 0, f'(\infty) = 1. \tag{2.30}$$

This problem can be solved numerically: figure 2.4 shows the velocity profile, $f'(\eta)$. It is apparent that u_x goes from 0 at $y = 0$ (the no-slip condition) to U_∞ at $y = \infty$ (the external flow). It does so over a distance $O(\delta)$, where

$$\delta \propto \sqrt{\frac{\nu x}{U_\infty}}. \tag{2.31}$$

Thus, the boundary-layer thickness grows like $x^{1/2}$. Comparing δ with the distance, $L = O(x)$, for streamwise development, $\delta/L = O(\mathrm{Re}_x^{-1/2})$. This is consistent with our earlier results and

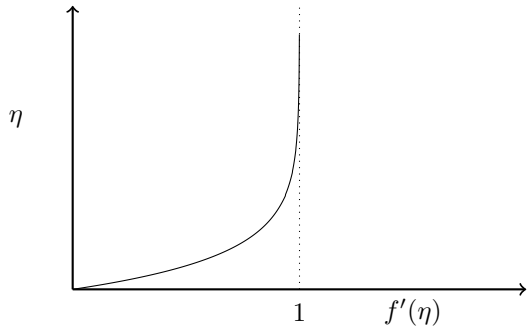

Figure 2.4: The Blasius profile.

shows that δ/L is indeed small if Re_x is large. Relation (2.31) can be interpreted as follows. A fluid particle takes a time $t = O(x/U_\infty)$ to travel from the leading edge to location x. During this time, viscous diffusion thickens the boundary layer to $O((\nu t)^{1/2})$, leading to (2.31). A commonly used measure of boundary-layer thickness is the displacement thickness

$$\delta_1 = \int_0^\infty \left(1 - \frac{u_x(x)}{U}\right) \mathrm{d}y. \tag{2.32}$$

The Blasius solution leads to

$$\delta_1 = 1.72\sqrt{\frac{\nu x}{U_\infty}}, \tag{2.33}$$

a more precise result than the order-of-magnitude scaling (2.31).

Before bringing this section to a close, note that the Blasius solution only applies while the boundary layer remains laminar. The Blasius flow becomes unstable at sufficiently large Re_x and transition to turbulence occurs. This is a further limitation of Prandtl theory, though approximations of boundary-layer type can be constructed to simplify the mean-flow equations of a turbulent boundary layer and turbulence modelling used for the Reynolds-stress terms in these equations. The study of the instability mechanisms leading to transition is one of the important motivations for the present work.

2.2 Axisymmetric boundary layers

2.2.1 Rotating body of revolution

Let us consider flow around a body of revolution which is rotating at angular velocity Ω and is placed in a uniform axial stream of velocity U_∞. Curvilinear coordinates (x, y, θ) are used, where x and y are defined as in figure 2.2 and θ is the azimuthal angle. The radius, $R(x)$, defines the shape of the body (see figure 2.5). Axisymmetry implies that derivatives of flow quantities with respect to θ are zero.

The presence of a solid boundary causes the development of a boundary layer and the inviscid flow just outside this layer is denoted by $U(x)$. Note that U is not a constant quantity and is obtained by solving the inviscid equations. The governing equations of the boundary layer can be obtained using order-of-magnitude estimates to derive a boundary-layer approximation, where the thickness of the boundary layer is assumed small in comparison to R. The boundary-layer

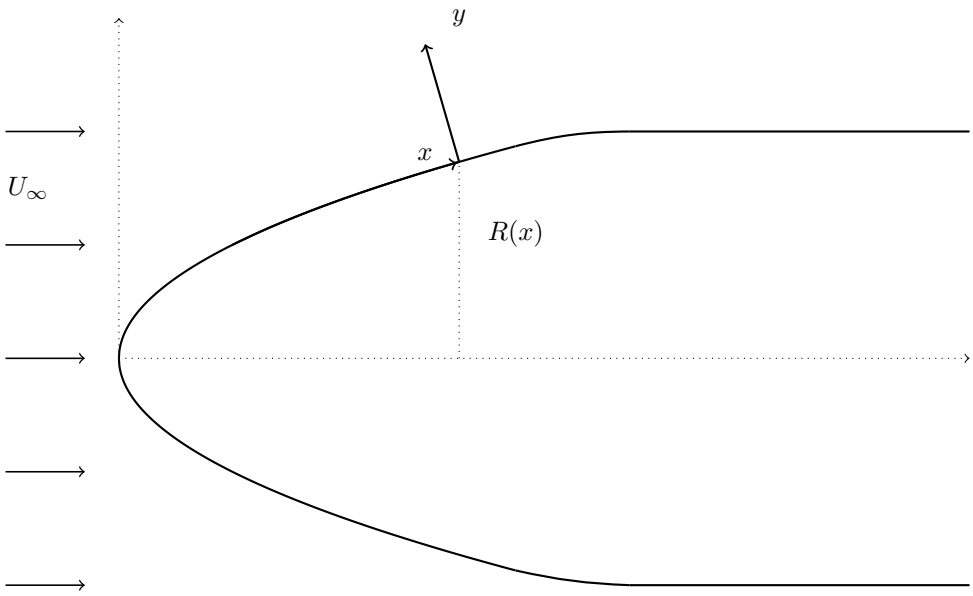

Figure 2.5: Illustration of flow around a rotating body of revolution.

equations (Mangler [1945]) are

$$u_x\frac{\partial u_x}{\partial x}+u_y\frac{\partial u_x}{\partial y}-\frac{u_\theta^2}{R}\frac{\mathrm{d}R}{\mathrm{d}x}=-\frac{1}{\rho}\frac{\partial p}{\partial x}+\nu\frac{\partial^2 u_x}{\partial y^2}, \tag{2.34}$$

$$u_x\frac{\partial u_\theta}{\partial x}+u_y\frac{\partial u_\theta}{\partial y}+\frac{u_\theta u_x}{R}\frac{\mathrm{d}R}{\mathrm{d}x}=\nu\frac{\partial^2 u_\theta}{\partial y^2}, \tag{2.35}$$

$$\frac{\partial u_x}{\partial x}+\frac{u_x}{R}\frac{dR}{dx}+\frac{\partial u_y}{\partial y}=0, \tag{2.36}$$

$$\frac{\partial p}{\partial y}=0, \tag{2.37}$$

$$\tag{2.38}$$

with the boundary conditions

$$u_x=u_y=0, u_\theta=\Omega R \quad y=0, \tag{2.39}$$

$$u_x\to U, u_\theta\to 0 \quad y\to\infty. \tag{2.40}$$

As before, the pressure gradient along x is obtained from the inviscid flow as

$$-\frac{1}{\rho}\frac{\partial p}{\partial x}=U\frac{\mathrm{d}U}{\mathrm{d}x}. \tag{2.41}$$

Equation (2.34) is similar to the case of a planar surface, with an additional term proportional to u_θ^2/R, representing a centrifugal effect on the development of the boundary layer due to rotation. The evolution of the boundary layer is also dependent on the shape of the body through the term $(1/R)dR/dx$. There is no variation of pressure across the boundary layer, and it is determined by the outer flow leading to (2.41). For a non-rotating body of revolution, the

boundary-layer equations are simply obtained by setting $u_\theta = 0$. Note that equations (2.34)–(2.41) describe the flow over the nose region in the cylinder problem introduced in chapter 1. These equations will be revisited in chapter 5 to discuss the effect of the nose on the flow along the cylinder.

2.2.2 Semi-infinite cylinder

The assumption of small boundary-layer thickness in comparison to R is not an essential part of the boundary-layer approximation and can be relaxed. This relaxation is crucial to develop the governing equations for axisymmetric bodies which are sufficiently long downstream that the boundary-layer thickness becomes comparable to, and eventually larger than, R. Let us consider steady flow along a rotating, semi-infinite cylinder. This is a special case of a body of revolution where R is a constant denoted by a. The external flow is the uniform flow denoted by U_∞. Cylindrical coordinates (z, r, θ) are appropriate for the problem. The Navier–Stokes equations and the scales used for their non-dimensionalization (a as length scale and U_∞ as velocity scale) were already introduced in chapter 1. Assuming that the boundary-layer thickness is small in comparison to z, a boundary-layer approximation is used to derive the governing equations. In the case of a non-rotating cylinder ($\Omega = 0$), the non-dimensionalized boundary-layer equations (Glauert & Lighthill [1955]) are

$$u_z \frac{\partial u_z}{\partial z} + u_r \frac{\partial u_z}{\partial r} = \frac{1}{\mathrm{Re}} \left(\frac{\partial^2 u_z}{\partial r^2} + \frac{1}{r} \frac{\partial u_z}{\partial r} \right), \tag{2.42}$$

$$\frac{\partial u_z}{\partial z} + \frac{1}{r} \frac{\partial r u_r}{\partial r} = 0, \tag{2.43}$$

$$u_z = 0, u_r = 0 \quad z > 0, r = 1, \tag{2.44}$$

$$u_z \to 1 \quad z > 0, r \to \infty, \tag{2.45}$$

where $\mathrm{Re} = U_\infty a/\nu$. In equation (2.42), the second term in brackets is negligible if the boundary-layer thickness is small compared with a. Under the same condition, the second term in equation (2.43) can be approximated by $\partial u_r/\partial r$. Making these approximations, equations (2.42)–(2.45) become the usual Prandtl equations for a flat plate. However, this is no longer the case once the boundary-layer thickness is comparable with a.

In the case of a rotating cylinder, the boundary-layer approximation gives

$$u_z \frac{\partial u_z}{\partial z} + u_r \frac{\partial u_z}{\partial r} = -\frac{\partial p}{\partial z} + \frac{1}{\mathrm{Re}} \left(\frac{\partial^2 u_z}{\partial r^2} + \frac{1}{r} \frac{\partial u_z}{\partial r} \right), \tag{2.46}$$

$$\frac{u_\theta^2}{r} = \frac{\partial p}{\partial r}, \tag{2.47}$$

$$u_z \frac{\partial u_\theta}{\partial z} + u_r \frac{\partial u_\theta}{\partial r} + \frac{u_\theta u_r}{r} = \frac{1}{\mathrm{Re}} \left(\frac{\partial^2 u_\theta}{\partial r^2} + \frac{1}{r} \frac{\partial u_\theta}{\partial r} - \frac{u_\theta}{r^2} \right), \tag{2.48}$$

$$\frac{\partial u_z}{\partial z} + \frac{1}{r} \frac{\partial r u_r}{\partial r} = 0, \tag{2.49}$$

$$u_z = 0, u_r = 0, u_\theta = S \quad z > 0, r = 1, \tag{2.50}$$

$$u_z \to 1, u_\theta \to 0, p \to 0 \quad z > 0, r \to \infty, \tag{2.51}$$

where $S = \Omega a/U_\infty$ is the rotation rate, which is a measure of the relative importance of cylinder rotation and axial flow. Note that the pressure now can vary significantly across the boundary layer, as is apparent from equation (2.47). This represents a centrifugal effect due to rotation and manifests itself as an axial pressure gradient in equation (2.46). Interestingly, significant axial

pressure gradients are also observed for swirling-jet flows (Görtler [1954], Loitsyanskii [1953]). Detailed discussion of the properties of the rotating cylinder flow is the subject of chapter 5.

Chapter 3

Linear stability analysis

This chapter briefly presents some elements of linear stability theory, with the aim of providing a foundation for chapters 4 and 6.

The starting point is the incompressible Navier–Stokes equations in non-dimensional form

$$\frac{\partial \mathbf{U}}{\partial t} + (\mathbf{U}.\nabla)\mathbf{U} = -\nabla P + \frac{1}{\mathrm{Re}}\nabla^2\mathbf{U}, \tag{3.1}$$

$$\nabla.\mathbf{U} = 0. \tag{3.2}$$

These equations are completed by initial and boundary conditions. The most common type of boundary, and the one considered here, is solid. At such a boundary, no-slip implies that the velocity of the fluid is specified (equal to the velocity of the solid).

3.1 Perturbation equations

Suppose we are interested in the stability of a flow $\bar{\mathbf{U}}$, $\bar{P}$ (referred to as the basic flow), which is a solution of (3.1), (3.2) and the boundary conditions. Any other flow is written

$$\mathbf{U} = \bar{\mathbf{U}} + \mathbf{u}, \quad P = \bar{P} + p, \tag{3.3}$$

where $\mathbf{u}$, p denote the perturbation to the basic flow. Both the perturbed and basic flows satisfy (3.1), (3.2) and the boundary conditions, the difference between the two flows being the result of differing initial conditions. The time evolution of the perturbation determines stability of the basic flow: the flow is unstable if the perturbation grows, in which case the basic flow is not realised.

Subtracting equations (3.1), (3.2) and the boundary conditions applied to the perturbed and basic flows yields the governing problem for the perturbation:

$$\frac{\partial \mathbf{u}}{\partial t} + (\bar{\mathbf{U}}.\nabla)\mathbf{u} + (\mathbf{u}.\nabla)\bar{\mathbf{U}} + (\mathbf{u}.\nabla)\mathbf{u} = -\nabla p + \frac{1}{\mathrm{Re}}\nabla^2\mathbf{u}, \tag{3.4}$$

$$\nabla.\mathbf{u} = 0, \tag{3.5}$$

with the boundary conditions

$$\mathbf{u} = 0. \tag{3.6}$$

If the perturbation is sufficiently small (infinitesimal), the nonlinear term $(\mathbf{u}.\nabla)\mathbf{u}$, in (3.4) is negligible compared to the others. Dropping this term,

$$\frac{\partial \mathbf{u}}{\partial t} + (\bar{\mathbf{U}}.\nabla)\mathbf{u} + (\mathbf{u}.\nabla)\bar{\mathbf{U}} = -\nabla p + \frac{1}{\mathrm{Re}}\nabla^2\mathbf{u}, \tag{3.7}$$

which, with (3.5) and the boundary condition (3.6), determine the time evolution of the perturbation. This is often referred to as linear stability theory and is henceforth adopted.

3.2 Steady flows and modes

If the basic flow is steady, as supposed from here on, the perturbation can be expressed as a superposition of (normal) modes of the form

$$\mathbf{u} = \mathbf{v}(\mathbf{x})\mathrm{e}^{-\mathrm{i}\omega t}, \quad p = q(\mathbf{x})\mathrm{e}^{-\mathrm{i}\omega t}, \tag{3.8}$$

where ω can be complex,

$$\mathrm{i}\omega\mathbf{v} = (\bar{\mathbf{U}}.\nabla)\mathbf{v} + (\mathbf{v}.\nabla)\bar{\mathbf{U}} + \nabla q - \frac{1}{\mathrm{Re}}\nabla^2\mathbf{v}, \tag{3.9}$$

$$\nabla.\mathbf{v} = 0, \tag{3.10}$$

and

$$\mathbf{v} = 0 \tag{3.11}$$

at the boundary. $\mathbf{v} = q = 0$ is always a solution of (3.9)–(3.11), but certain values of ω (the eigenvalues) allow a nonzero solution. These are the values which yield modes. The spatial structure of a mode is determined by the eigenfunctions $\mathbf{v(x)}$ and $q(\mathbf{x})$.

Writing $\omega = \omega_r + \mathrm{i}\omega_i$, the modal time dependence

$$\mathrm{e}^{-\mathrm{i}\omega t} = \underbrace{\exp[\omega_i t]}_{\text{Growth/decay}} \underbrace{(\cos\omega_r t - \mathrm{i}\sin\omega_r t)}_{\text{Oscillations}} \tag{3.12}$$

is the product of a real exponential and a term which has sinusoidal oscillations of frequency ω_r. If $\omega_i > 0$, the mode is growing. If such a mode can be found, i.e. there is an eigenvalue with $\omega_i > 0$, the flow is unstable. Thus, characterization of flow stability comes down to an eigenvalue calculation. The quantity ω_i is often referred to as the growth rate.

Given a mode, ω, $\mathbf{v(x)}$, $q(\mathbf{x})$, the complex conjugate of (3.8) yields another one, $-\omega^*$, $\mathbf{v}^*\mathbf{(x)}$, $q^*(\mathbf{x})$, where $*$ denotes complex conjugation. Note that a mode and its conjugate have the same growth rate, ω_i; in particular, if one is growing, so is the other. The construction of a physically meaningful (i.e. real) solution of (3.5)–(3.7) from modes, which are complex solutions, requires that a mode be accompanied by its conjugate. Thus, the two are not physically distinct and can be treated as a single entity.

3.3 Spatial symmetries

Suppose that the modal eigenvalue problem, (3.9)–(3.11), is invariant under translation in the Cartesian coordinate z. This requires that $\bar{\mathbf{U}}$ be independent of z and that the flow domain occupy the infinite domain $-\infty < z < \infty$. Modes then have the more specific form

$$\mathbf{u} = \mathbf{v}(x,y)\mathrm{e}^{\mathrm{i}(\alpha z - \omega t)}, \quad p = q(x,y)\mathrm{e}^{\mathrm{i}(\alpha z - \omega t)}, \tag{3.13}$$

where α is a real parameter known as the wavenumber. The $\mathrm{e}^{\mathrm{i}\alpha z}$ dependence corresponds to a single Fourier component, from which a general function of z can be constructed by superposing modes with all values of α using Fourier synthesis. Translational invariance means that different Fourier components decouple and can be treated separately.

Rather than Cartesian coordinates, axisymmetric flows are better treated using cylindrical coordinates, (z, r, θ), whose axis of symmetry coincides with that of the flow. Axisymmetry means that the cylindrical components of $\bar{\mathbf{U}}$ are independent of θ and that the flow domain has axisymmetric boundaries. The corresponding modal form is

$$\begin{pmatrix} u_z \\ u_r \\ u_\theta \end{pmatrix} = \begin{pmatrix} v_z(z,r) \\ v_r(z,r) \\ v_\theta(z,r) \end{pmatrix} \mathrm{e}^{\mathrm{i}(m\theta-\omega t)}, \quad p = q(z,r)\mathrm{e}^{\mathrm{i}(m\theta-\omega t)}, \tag{3.14}$$

where m is an integer known as the azimuthal wavenumber. An integer value of m is necessary so that the mode has 2π-periodicity with respect to θ.

Symmetries other than axisymmetry and translational invariance are possible, for instance spatial (or temporal) periodicity, which leads to Floquet modes, or reflection symmetry, which implies modes with even or odd parity. However, we are interested in the case of combined translational invariance and axisymmetry, for which the modes have the form

$$\begin{pmatrix} u_z \\ u_r \\ u_\theta \end{pmatrix} = \begin{pmatrix} v_z(r) \\ v_r(r) \\ v_\theta(r) \end{pmatrix} \mathrm{e}^{\mathrm{i}(\alpha z+m\theta-\omega t)}, \quad p = q(r)\mathrm{e}^{\mathrm{i}(\alpha z+m\theta-\omega t)}. \tag{3.15}$$

Thus, the eigenfunctions, $v_z(r)$, $v_r(r)$, $v_\theta(r)$, $q(r)$, depend on just the one spatial coordinate, r, while we have free choice of the modal parameters α and m; the former can take any real value, while the latter must be an integer. These parameters determine which Fourier component of the perturbation is being studied. Symmetry requires that the cylindrical components of $\bar{\mathbf{U}}$ are independent of both z and θ. Assuming $\bar{U}_r = 0$ (which is consistent with (3.2)) and using (3.15) in (3.5) and (3.7), written in terms of cylindrical coordinates, gives

$$\mathrm{i}\left(\alpha\bar{U}_z + \frac{m\bar{U}_\theta}{r} - \omega\right) v_z + \bar{U}_z' v_r + \mathrm{i}\alpha q = \frac{1}{\mathrm{Re}}\left[v_z'' + \frac{1}{r}v_z' - \left(\alpha^2 + \frac{m^2}{r^2}\right) v_z\right], \tag{3.16}$$

$$\begin{aligned}\mathrm{i}\left(\alpha\bar{U}_z + \frac{m\bar{U}_\theta}{r} - \omega\right) v_r - \frac{2\bar{U}_\theta}{r}v_\theta + q' = \frac{1}{\mathrm{Re}}\Bigg[&v_r'' + \frac{1}{r}v_r' \\ &- \left(\alpha^2 + \frac{m^2+1}{r^2}\right) v_r - \frac{2\mathrm{i}m}{r^2}v_\theta\Bigg],\end{aligned} \tag{3.17}$$

$$\begin{aligned}\mathrm{i}\left(\alpha\bar{U}_z + \frac{m\bar{U}_\theta}{r} - \omega\right) v_\theta + \left(\bar{U}_\theta' + \frac{\bar{U}_\theta}{r}\right) v_r + \frac{\mathrm{i}m}{r}q = \frac{1}{\mathrm{Re}}\Bigg[&v_\theta'' + \frac{1}{r}v_\theta' \\ &- \left(\alpha^2 + \frac{m^2+1}{r^2}\right) v_\theta + \frac{2\mathrm{i}m}{r^2}v_r\Bigg],\end{aligned} \tag{3.18}$$

$$\mathrm{i}\alpha v_z + v_r' + \frac{1}{r}v_r + \frac{\mathrm{i}m}{r}v_\theta = 0, \tag{3.19}$$

where the primes denote derivatives with respect to r. Equations (3.16)–(3.19), together with appropriate boundary conditions, yield an eigenvalue problem for determination of ω and the eigenfunctions $v_z(r)$, $v_r(r)$, $v_\theta(r)$, $q(r)$.

3.4 The rotating-cylinder problem and local analysis

As described earlier, the specific problem studied in this thesis is a semi-infinite rotating cylinder of radius a placed in a uniform, axial stream of velocity U_∞. The length, velocity and time scales used to non-dimensionalize the problem are a, U_∞ and a/U_∞. As noted in the previous

chapter, we are interested in the case of large $\mathrm{Re} = U_\infty a/\nu$ and large streamwise distances, $z = O(\mathrm{Re})$, such that the boundary-layer thickness has increased to $O(a)$. The boundary-layer approximation can be used to determine the basic flow. The component $\bar{U}_r$ is small compared with $\bar{U}_z$ and $\bar{U}_\theta$, which are functions of $Z = z/\mathrm{Re}$ and r obtained by numerical solution of the boundary-layer equations. Recall that the basic flow also depends on the non-dimensional rotation rate $S = \Omega a/U_\infty$, where Ω is the angular velocity of the cylinder.

The basic flow is steady and axisymmetric, but is not strictly translation invariant with respect to z. However, there is a separation of scales: the radial scale being small compared with the axial one. This means that, although the basic flow varies with z, it does so slowly and can be locally approximated as if it were translationally invariant. Furthermore, smallness of $\bar{U}_r$ compared with $\bar{U}_z$ and $\bar{U}_\theta$ allows us to approximate it as zero. Thus, (3.16)–(3.19) provide a local approximation of the stability problem. The boundary conditions are

$$v_z(1) = v_r(1) = v_\theta(1) = 0, \tag{3.20}$$

$$v_z(\infty) = v_r(\infty) = v_\theta(\infty) = 0. \tag{3.21}$$

Note that the asymptotic (at large Re) separation of radial and axial scales provides the basis of both the boundary-layer approximation of the basic flow and the local stability analysis.

The basic flow appears in (3.16)–(3.18) via the velocity profiles $\bar{U}_z(r)$ and $\bar{U}_\theta(r)$, which, as noted above, depend on Z and S. Although, thanks to use of the scaled variable $Z = z/\mathrm{Re}$, the Reynolds number does not influence the basic flow, it appears explicitly in (3.16)–(3.18), as do α and m. Thus, the parameters of the stability problem are α, m, Re, S and Z. Once these parameters are specified, (3.16)–(3.21) form an eigenvalue problem, which is solved numerically as described in the next chapter. Formally, the result can be expressed as

$$\omega = \omega(\alpha, m, \mathrm{Re}, S, Z). \tag{3.22}$$

Re, S and Z are physical parameters, the latter expressing the axial location for which stability is studied. On the other hand, α and m are modal parameters which can be freely chosen. One should scan over all values of α and m looking for a growing mode ($\omega_i > 0$). If one is found, the flow is unstable for the given Re, S and Z. Note that the conjugate of a growing mode with $\alpha < 0$ has $\alpha > 0$ and is also growing. This allows us to restrict attention to $\alpha \geq 0$.

3.5 Spatial stability

The above discussion has focused on temporal stability analysis, in which α is a real parameter and ω a complex frequency determined by an eigenvalue problem. For completeness sake, we should also mention another approach, namely spatial analysis, in which ω is a real parameter and α a complex eigenvalue determined by the requirement that (3.16)–(3.21) have a nonzero solution. The idea is that the perturbation is generated by a time-harmonic source at some location z, yielding disturbances which propagate both upstream and downstream and may grow with propagation distance, leading to spatial instability.

The difficulty with spatial analysis is that, for a given real ω, there are usually possible complex $\alpha = \alpha_r + \mathrm{i}\alpha_i$ in both $\alpha_i < 0$ and $\alpha_i > 0$, the former representing a mode which grows towards increasing x, while the latter grows towards decreasing x. Each complex α is associated with either upstream or downstream propagation from the source, but it is far from straightforward to identify the direction of propagation. Without this information, spatial stability analysis cannot be conclusive.

As discussed in Huerre & Monkewitz [1990], the identification of upstream and downstream propagating modes requires spatio-temporal analysis, in which both ω and α are complex and

related by the requirement that (3.16)–(3.21) have a nonzero solution. At large positive ω_i, upstream propagating modes lie in $\alpha_i > 0$, while downstream propagating ones have $\alpha_i < 0$. Thus, the separation into the two types of modes is clear. Analytical continuation of $\alpha(\omega)$ down to the real ω-axis then yields the upstream and downstream modes of the spatial problem. Implementation of this procedure is complicated and analytic continuation may break down if a so-called pinch occurs (coincidence of an upstream and downstream $\alpha(\omega)$ for some ω in $\omega_i > 0$). This leads to absolute instability and spatial stability analysis is not then appropriate. Absolute instability means that at large times, the perturbation grows and is dominated by the pinch-point ω, rather than settling down to the frequency imposed by the source.

In summary, temporal analysis determines the stability/instability of the flow. If it is stable according to such analysis, it can be shown that neither absolute nor spatial instability can occur. On the other hand, if temporal instability occurs, the next stage is spatio-temporal analysis to see if the flow is convectively or absolutely unstable. Only in the convective case does it make sense to study spatial instability. This thesis is devoted to temporal instability alone.

Chapter 4

Numerical methods

In this chapter, the numerical techniques used to solve the basic-flow and linear-stability equations for flow around a rotating cylinder are presented. The governing equations of the basic flow are the boundary-layer equations, (2.46)–(2.51), of chapter 2. The corresponding linear-stability equations, (3.16)–(3.21), have been formulated in chapter 3. These equations form the basis of the numerical methods used in solving the basic-flow and stability problems. Variable transformations used to improve numerical accuracy are presented in section 4.1, while section 4.2 describes numerical discretization of the radial coordinate. Section 4.3 concerns the numerical schemes employed to solve the basic-flow equations, while section 4.4 discusses the methods used to solve the stability problem. Finally, section 4.5 presents results of various checks used for verifying the different numerical tools, along with validation results for the basic-flow and stability computations.

4.1 Variable transformations

The thickness of the Blasius boundary layer is known to grow as the square-root of the distance from the leading edge. Since similar behaviour is expected here, the following transformation of coordinates is adopted:

$$\zeta = \left(\frac{2z}{\mathrm{Re}}\right)^{\frac{1}{2}} = (2Z)^{\frac{1}{2}}, \quad \sigma = \frac{r-1}{\zeta}. \tag{4.1}$$

The advantage of this transformation is that it avoids the singular behaviour as $z \to 0$ arising from the boundary-layer thickness going to zero in this limit. The variable σ incorporates the thickening of the boundary layer as z increases via the factor $1/\zeta$. Note that σ varies from 0 to ∞, whereas r varies from 1 to ∞. The spatial derivatives transform as

$$\frac{\partial}{\partial z} = \frac{1}{\zeta \mathrm{Re}}\left(\frac{\partial}{\partial \zeta} - \frac{\sigma}{\zeta}\frac{\partial}{\partial \sigma}\right), \tag{4.2}$$

$$\frac{\partial}{\partial r} = \frac{1}{\zeta}\frac{\partial}{\partial \sigma}. \tag{4.3}$$

The basic-flow quantities (u_z, u_r, u_θ, p) are transformed using

$$V_r = \zeta r u_r \mathrm{Re}, \quad V_z = u_z, \quad V_\theta = r u_\theta, \quad P = r^2 p. \tag{4.4}$$

The factors of r and r^2 are included in the definitions of V_r, V_θ and P to improve convergence of the numerical scheme used to solve the basic-flow equations. The factor of ζ in V_r removes the infinite singularity of u_r as $z \to 0$.

4.2 Radial discretization

The infinite domain $0 < \sigma < \infty$ is transformed to a finite one using

$$x = \frac{\sigma - \hat{\sigma}}{\sigma + \hat{\sigma}} \quad \sigma \in [0, \infty] \to x \in [-1, 1]. \tag{4.5}$$

N Chebyshev collocation points are then defined by

$$x_n = \cos\left(\frac{n\pi}{N-1}\right) \quad 0 \le n \le N-1, \tag{4.6}$$

where $n = 0$ corresponds to radial infinity ($\sigma = r = \infty$) and $n = N-1$ to the cylinder surface ($\sigma = 0, r = 1$). $\hat{\sigma}$ is a numerical parameter allowing some control over the distribution of collocation points over the radial coordinate: half of the collocation points cover the interval $0 \le \sigma \le \hat{\sigma}$.

As usual, the problem unknowns, i.e. here the velocity and pressure, are represented by their values at the collocation points. Radial derivatives follow by polynomial approximation, as described later for the basic-flow and stability problems. Note that the value of N used for the stability calculation is the same as for the basic flow, to avoid interpolation.

4.3 Numerical treatment of the basic flow

Following coordinate transformation and rescaling of variables as discussed in section 4.1, the basic flow equations (2.46)–(2.51) become

$$\zeta V_z \frac{\partial V_z}{\partial \zeta} + \left(\frac{V_r - \zeta}{r} - \sigma V_z\right)\frac{\partial V_z}{\partial \sigma} = \frac{1}{r^2}(\sigma\frac{\partial P}{\partial \sigma} - \zeta\frac{\partial P}{\partial \zeta}) + \frac{\partial^2 V_z}{\partial \sigma^2}, \tag{4.7}$$

$$\frac{\zeta}{r}\left(V_\theta^2 + 2P\right) = \frac{\partial P}{\partial \sigma}, \tag{4.8}$$

$$\zeta V_z \frac{\partial V_\theta}{\partial \zeta} + \left(\frac{V_r + \zeta}{r} - \sigma V_z\right)\frac{\partial V_\theta}{\partial \sigma} = \frac{\partial^2 V_\theta}{\partial \sigma^2}, \tag{4.9}$$

$$\zeta\frac{\partial V_z}{\partial \zeta} - \sigma\frac{\partial V_z}{\partial \sigma} + \frac{1}{r}\frac{\partial V_r}{\partial \sigma} = 0, \tag{4.10}$$

along with the boundary conditions

$$V_z = V_r = 0, V_\theta = S \quad \sigma = 0, \tag{4.11}$$

$$V_z \to 1, V_\theta \to 0, P \to 0 \quad \sigma \to \infty. \tag{4.12}$$

Equations (4.7)–(4.12) represent a nonlinear, parabolic system of partial differential equations. These equations are completed by an inlet condition obtained by solving the equations at $\zeta = 0$.

When $\zeta = 0$, $r = 1$ from equation (4.1). Equation (4.8) gives $\partial P/\partial\sigma = 0$ and applying the boundary condition for P gives $P = 0$. Thus, the inlet equations are

$$(V_r - \sigma V_z)\frac{\partial V_z}{\partial \sigma} = \frac{\partial^2 V_z}{\partial \sigma^2}, \tag{4.13}$$

$$(V_r - \sigma V_z)\frac{\partial V_\theta}{\partial \sigma} = \frac{\partial^2 V_\theta}{\partial \sigma^2}, \tag{4.14}$$

$$\frac{\partial V_r}{\partial \sigma} - \sigma\frac{\partial V_z}{\partial \sigma} = 0, \tag{4.15}$$

$$V_z = V_r = 0, V_\theta = S \quad \sigma = 0, \tag{4.16}$$

$$V_z \to 1, V_\theta \to 0 \quad \sigma \to \infty. \tag{4.17}$$

Equations (4.13)-(4.17) represent the flow over a flat plate with spanwise velocity S. V_θ is determined using equation (4.14), once V_z and V_r are computed using (4.13) and (4.15).

It may be of interest to note that (4.13)–(4.15) have the analytical solution

$$V_z = g'(\sigma), \quad V_r = \sigma g'(\sigma) - g(\sigma), \quad V_\theta = S(1 - g'(\sigma)), \tag{4.18}$$

where $g(\sigma)$ is the solution of the Blasius problem

$$g''' + gg'' = 0, \tag{4.19}$$

$$g(0) = g'(0) = 0, \quad g'(\infty) = 1. \tag{4.20}$$

Thus, the flow approaches a generalized (generalized in the sense that the plate has spanwise motion) version of the Blasius flow as $\zeta \to 0$.

The transformation, (4.5), to a finite radial domain is applied to (4.7)–(4.10) and (4.13)–(4.15) prior to discretization, which is described in the next two subsections.

4.3.1 Radial discretization

The transformed radial coordinate x is discretized using a Chebyshev collocation method, as described in section 4.2. The velocity components V_z and V_θ are represented at each of these grid points, while pressure is defined at all grid points, apart from the surface point, $\sigma = 0$. V_r is defined at all the grid points, except the outer one, $\sigma = \infty$. Thus the unknowns are

$$V_z^n, V_\theta^n \quad 0 \le n \le N-1, \tag{4.21}$$

$$V_r^n \quad 1 \le n \le N-1, \tag{4.22}$$

$$P^n \quad 0 \le n \le N-2. \tag{4.23}$$

This results in a total of $4N - 2$ unknowns. V_z and V_θ are fitted using $(N-1)$th degree interpolation polynomials:

$$h_n(x) = \prod_{k=0, k\neq n}^{N-1} \frac{x - x_k}{x_n - x_k} \quad 0 \le n \le N-1, \tag{4.24}$$

$$V = \sum_{k=0}^{N-1} V^k h_k(x), \tag{4.25}$$

where V denotes either V_z or V_θ. The numerical approximation of the derivative of V with respect to x is

$$\left(\frac{\partial V}{\partial x}\right)_{x=x_n} = \sum_{k=0}^{N-1} D_{nk} V^k, \quad D_{nk} = \frac{\mathrm{d}h_k}{\mathrm{d}x}(x_n), \tag{4.26}$$

where D_{nk} is the usual Chebyshev derivative matrix. The second-order derivatives are

$$\left(\frac{\partial^2 V}{\partial x^2}\right)_{x=x_n} = \sum_{k=0}^{N-1} D_{nk}^2 V^k. \tag{4.27}$$

Pressure is fitted by $(N-2)$th degree interpolation polynomials:

$$\hat{h}_n(x) = \frac{x_n+1}{x+1} h_n(x) \quad 0 \le n \le N-2, \tag{4.28}$$

$$P = \sum_{k=0}^{N-2} P^k \hat{h}_k(x). \tag{4.29}$$

Thus, the pressure derivative is approximated as

$$\left(\frac{\partial P}{\partial x}\right)_{x=x_n} = \sum_{k=0}^{N-2} \hat{D}_{nk} P^k, \tag{4.30}$$

$$\begin{aligned} \hat{D}_{nk} &= \frac{x_k+1}{x_n+1} h_k'(x_n) - h_k(x_n) \frac{x_k+1}{(x_n+1)^2} \\ &= \frac{x_k+1}{x_n+1} D_{nk} - \frac{1}{x_n+1}\delta_{nk} \quad 0 \le n,k \le N-2, \end{aligned} \tag{4.31}$$

where δ_{nk} is the Kronecker delta.

Finally, the radial velocity component V_r is fitted using $(N-2)$th degree interpolation polynomials:

$$\bar{h}_n(x) = \frac{x_n-1}{x-1} h_n(x) \quad 1 \le n \le N-1, \tag{4.32}$$

$$V_r = \sum_{k=1}^{N-1} V_r^k \bar{h}_k(x). \tag{4.33}$$

The derivative is

$$\left(\frac{\partial V_r}{\partial x}\right)_{x=x_n} = \sum_{k=1}^{N-1} \bar{D}_{nk} V_r^k, \tag{4.34}$$

$$\begin{aligned} \bar{D}_{nk} &= \frac{x_k-1}{x_n-1} h_k'(x_n) - h_k(x_n) \frac{x_k-1}{(x_n-1)^2} \\ &= \frac{x_k-1}{x_n-1} D_{nk} - \frac{1}{x_n-1}\delta_{nk} \quad 1 \le n,k \le N-1. \end{aligned} \tag{4.35}$$

Equations (4.7)–(4.10) are applied at the interior points, $x = x_n, 1 \le n \le N-2$, leading to $4N-8$ equations. Adding the 6 boundary conditions balances the number of equations and unknowns. There remains the question of axial discretization, needed to express the ζ-derivatives in (4.7), (4.9) and (4.10). This is addressed in the next section.

As regards to the inlet problem, (4.13)–(4.17), (4.13)–(4.15) are applied at the interior points, $x = x_n, 1 \le n \le N-2$, giving $3N-6$ equations. Adding the 5 boundary conditions, (4.16) and (4.17), gives a total of $3N-1$ equations, equal to the number of unknowns, (4.21) and (4.22). As we have seen, $P = 0$ at the inlet, completing the inlet conditions. There is, of course, no need for axial discretization of the inlet problem.

4.3.2 Axial discretization

The streamwise coordinate ζ is discretized using

$$\zeta_i = i\Delta \quad 0 \leq i \leq M. \tag{4.36}$$

The flow variables are represented as follows:

$$V_{z,i}^n = V_z^n(\zeta_i), \quad V_{\theta,i}^n = V_\theta^n(\zeta_i), \quad P_i^n = P^n(\zeta_i), \quad V_{r,i}^n = V_r^n(\zeta_{i+\frac{1}{2}}). \tag{4.37}$$

In keeping with the parabolic character of the boundary-layer equations, a marching scheme towards increasing ζ was used. The scheme was chosen to be implicit, to avoid stiffness problems near $\zeta = 0$, centred and second-order (of Crank–Nicolson type). The solution of the inlet problem provides initial conditions, while, at each ζ-step, equations (4.7)–(4.10) are discretized in the radial directions, as described in the previous subsection. Equations (4.7), (4.9) and (4.10) are applied at $\zeta_{i+\frac{1}{2}}$, while (4.8) is applied at ζ_i. ζ-derivatives are approximated by centred differencing, while quantities needed at values of ζ for which they have no direct discretized representation are approximated by the average of the surrounding ζ. The result is a set of $4N-2$ nonlinear equations in $4N-2$ unknowns, whose solution, along with that of the inlet problem, is the subject of the following subsection.

4.3.3 Newton–Raphson method

As noted above, at each step in ζ, equations (4.7)–(4.10) along with boundary conditions (4.11) and (4.12) result in a total of $4N-2$ equations in the $4N-2$ unknowns, $V_{z,i}^n$, $V_{r,i}^n$, $V_{\theta,i}^n$ and P_i^n. These equations can be represented as

$$F_l(X_j) = 0 \quad 1 \leq j, l \leq 4N-2, \tag{4.38}$$

where F represents the set of discretized equations and X the unknowns. A numerical approximation to the solution of equation (4.38) is obtained by successively applying the Newton–Raphson iteration formula

$$X^{k+1} = X^k - J^{-1}(X^k)F(X^k), \tag{4.39}$$

$$J_{lj} = \frac{\partial F_l}{\partial X_j}, \tag{4.40}$$

where X^k and X^{k+1} represent the solution at the k-th and $(k+1)$-th iteration respectively. In numerical terms, F and X are arrays of size $4N-2$. $\partial F_l/\partial X_j$ is known as the Jacobian and is a square matrix of size $(4N-2)\times(4N-2)$. At each iteration, we have to solve a linear system of equations to obtain X^{k+1}, the new approximate solution to the system of equations. The solution is deemed to have converged when

$$||X^{k+1} - X^k||_2 < \tau, \tag{4.41}$$

where τ is a convergence tolerance and $||(.)||_2$ denotes the standard L^2-norm. Note that the iteration method can also be applied to the inlet problem. Iteration requires an initial estimate of the solution that is not too far from the the actual solution. At the inlet, the estimated solution can be an arbitrary function which satisfies the boundary conditions, and the iteration method converges to the required solution. The inlet solution is then used as an initial estimate for the second step. At subsequent steps, the solution at the previous step is used as the estimated solution.

4.4 Numerical approach to linear stability analysis

Applying the transformation (4.1) of the radial coordinate, equations (3.16)–(3.21) give

$$\mathrm{i}\bar{\alpha}v_z + v_r' + \xi v_r + \mathrm{i}m\xi v_\theta = 0, \tag{4.42}$$

$$\mathrm{i}(\bar{\alpha}\bar{U}_z - \bar{\omega})v_z + \bar{U}_z' v_r + \mathrm{i}m\xi\bar{U}_\theta v_z + \mathrm{i}\bar{\alpha}q = \frac{1}{\mathrm{Re}_\delta}(v_z'' + \xi v_z' - (\bar{\alpha}^2 + m^2\xi^2)v_z), \tag{4.43}$$

$$\mathrm{i}(\bar{\alpha}\bar{U}_z - \bar{\omega})v_r + \bar{U}_\theta\xi(\mathrm{i}mv_r - 2v_\theta) + q' = \frac{1}{\mathrm{Re}_\delta}(v_r'' + \xi v_r' - (\bar{\alpha}^2 + (m^2+1)\xi^2)v_r - 2\mathrm{i}m\xi^2 v_\theta), \tag{4.44}$$

$$\mathrm{i}(\bar{\alpha}\bar{U}_z - \bar{\omega})v_\theta + (\bar{U}_\theta' + \xi\bar{U}_\theta)v_r + \mathrm{i}m\xi\bar{U}_\theta v_\theta + \mathrm{i}m\xi q = \frac{1}{\mathrm{Re}_\delta}(v_\theta'' + \xi v_\theta' - (\bar{\alpha}^2 + (m^2+1)\xi^2)v_\theta + 2\mathrm{i}m\xi^2 v_r), \tag{4.45}$$

along with the boundary conditions

$$v_z(0) = v_r(0) = v_\theta(0) = 0, \tag{4.46}$$

$$v_z(\infty) = v_r(\infty) = v_\theta(\infty) = 0, \tag{4.47}$$

where

$$\mathrm{Re}_\delta = \zeta\mathrm{Re} = \left(\frac{2U_\infty az}{\nu}\right)^{1/2}, \qquad \xi = \frac{\zeta}{1+\zeta\sigma}, \tag{4.48}$$

$$\bar{\alpha} = \zeta\alpha, \qquad \bar{\omega} = \zeta\omega. \tag{4.49}$$

Note that primes denote derivatives with respect to σ in these equations. Following the same notation as in chapter 3, $\bar{U}_z, \bar{U}_\theta$ are the basic-flow velocity profiles, obtained by solving the basic-flow equations as described in the previous section. The transformation, (4.5), to a finite radial domain is applied to (4.42)–(4.45) prior to discretization, which is described in the next section.

4.4.1 Radial discretization

The transformed radial coordinate, x, is discretized using Chebyshev collocation points, as described in section 4.2. The perturbation velocities, v_z, v_r, v_θ are represented by their values, v_z^n, v_r^n, v_θ^n, at all N collocation points. Their derivatives are approximated in the usual way by

$$\left(\frac{\partial v}{\partial x}\right)_{x=x_n} = \sum_{k=1}^{N-2} D_{nk}v^k, \tag{4.50}$$

$$\left(\frac{\partial^2 v}{\partial x^2}\right)_{x=x_n} = \sum_{k=1}^{N-2} D_{nk}^2 v^k, \tag{4.51}$$

where we have employed the boundary conditions (4.46) and (4.47) (the terms $k = 0$ and $k = N-1$ in the sums are zero).

The pressure q is represented by its values, q^n, at the interior collocation points, $x = x_n, 1 \le n \le N-2$. Fitting of an $(N-3)$th degree polynomial gives

$$q = \sum_{k=1}^{N-2} q^k \tilde{h}_k(x), \tag{4.52}$$

$$\tilde{h}_n(x) = \left(\frac{x_n+1}{x+1}\right)\left(\frac{x_n-1}{x-1}\right)h_n(x) \quad 1 \le n \le N-2. \tag{4.53}$$

Thus, the derivative of q is approximated as

$$\left(\frac{\partial q}{\partial x}\right)_{x=x_n} = \sum_{k=1}^{N-2} \tilde{D}_{nk} q^k, \tag{4.54}$$

$$\tilde{D}_{nk} = \frac{1}{x_n^2 - 1}\left((x_k^2 - 1)D_{nk} - 2x_n\delta_{nk}\right) \quad 1 \le n, k \le N-2. \tag{4.55}$$

Equations (4.42)–(4.45) are applied at all interior collocation points, yielding $4N-8$ equations for the same number of unknowns, $v_z^n, v_r^n, v_\theta^n, q^n$ $(1 \le n \le N-2)$.

4.4.2 Eigenvalue problem

Let us define a vector, $\bar{X}$, of unknowns by

$$\bar{X} = (v_z^1, ..., v_z^{N-2}, v_r^1, ..., v_r^{N-2}, v_\theta^1, ..., v_\theta^{N-2}, q^1, ..., q^{N-2}). \tag{4.56}$$

The system of equations has the form

$$\bar{\omega} A \bar{X} = B \bar{X}, \tag{4.57}$$

where

$$A = \begin{bmatrix} I & 0 & 0 & 0 \\ 0 & I & 0 & 0 \\ 0 & 0 & I & 0 \\ 0 & 0 & 0 & 0 \end{bmatrix}, \quad B = \begin{bmatrix} b_{00} & b_{01} & 0 & b_{03} \\ 0 & b_{11} & b_{12} & b_{13} \\ 0 & b_{21} & b_{22} & b_{23} \\ b_{30} & b_{31} & b_{32} & 0 \end{bmatrix}, \tag{4.58}$$

$$(b_{00})_{nk} = (\bar{\alpha}\bar{U}_z^n + m\xi_n\bar{U}_\theta^n)\delta_{nk} + \frac{\mathrm{i}}{\mathrm{Re}_\delta}\left(D_{nk}^{(2)} + \xi_n D_{nk}^{(1)} - (\bar{\alpha}^2 + m^2\xi_n^2)\delta_{nk}\right),$$

$$(b_{01})_{nk} = -\mathrm{i}\bar{U}_z'^n\delta_{nk}, \quad (b_{03})_{nk} = \bar{\alpha}\delta_{nk},$$

$$(b_{11})_{nk} = (b_{22})_{nk} = (\bar{\alpha}\bar{U}_z^n + m\xi_n\bar{U}_\theta^n)\delta_{nk} + \frac{\mathrm{i}}{\mathrm{Re}_\delta}\left[D_{nk}^{(2)} + \xi_n D_{nk}^{(1)} - \left(\bar{\alpha}^2 + (m^2+1)\xi_n^2\right)\delta_{nk}\right],$$

$$(b_{12})_{nk} = 2\xi_n\left(\mathrm{i}\bar{U}_\theta^n + \frac{m}{\mathrm{Re}_\delta}\xi_n\right)\delta_{nk}, \quad (b_{13})_{nk} = -\mathrm{i}\tilde{D}_{nk}^{(1)},$$

$$(b_{21})_{nk} = -\mathrm{i}(\xi_n\bar{U}_\theta^n + \bar{U}_\theta'^n)\delta_{nk} - \frac{2m}{\mathrm{Re}_\delta}\xi_n^2\delta_{nk}, \quad (b_{23})_{nk} = m\xi_n\delta_{nk},$$

$$(b_{30})_{nk} = \bar{\alpha}\delta_{nk}, \quad (b_{31})_{nk} = -\mathrm{i}(D_{nk}^{(1)} + \xi_n\delta_{nk}), \quad (b_{32})_{nk} = m\xi_n\delta_{nk},$$

$$D_{nk}^{(1)} = \frac{1}{2\hat{\sigma}}(1-x_n)^2 D_{nk},$$

$$D_{nk}^{(2)} = \frac{1}{4\hat{\sigma}^2}(1-x_n)^3\left((1-x_n)D_{nk}^2 - 2D_{nk}\right),$$

$$\tilde{D}_{nk}^{(1)} = \frac{1}{2\hat{\sigma}}(1-x_n)^2\tilde{D}_{nk}, \tag{4.59}$$

and n, k run over the values $1 \le n, k \le N-2$ in the above equations. The notation $\bar{U}_z^n, \bar{U}_z'^n, \bar{U}_\theta^n$, ξ_n denotes the values at the collocation point x_n. A and B are square matrices of size $4N-8$ which are divided into blocks of smaller matrices. Each block b_{ij} is a square matrix of size $N-2$, while I denotes an identity matrix of size $N-2$. (4.57) is a generalized eigenvalue problem for the determination of $\bar{\omega}$ and $\bar{X}$.

4.4.3 Elimination of pressure

Equation (4.58) can be reexpressed as

$$\bar{\omega}\underline{v}_z = b_{00}\underline{v}_z + b_{01}\underline{v}_r + b_{03}\underline{q}, \tag{4.60}$$
$$\bar{\omega}\underline{v}_r = b_{11}\underline{v}_r + b_{12}\underline{v}_\theta + b_{13}\underline{q}, \tag{4.61}$$
$$\bar{\omega}\underline{v}_\theta = b_{21}\underline{v}_r + b_{22}\underline{v}_\theta + b_{23}\underline{q}, \tag{4.62}$$
$$0 = b_{30}\underline{v}_z + b_{31}\underline{v}_r + b_{32}\underline{v}_\theta, \tag{4.63}$$

where $\underline{v}_z = (v_z^1, ..., v_z^{N-2})$ and similarly for $\underline{v}_r, \underline{v}_\theta$ and $\underline{q}$. Multiplying the first three of the above equations respectively by b_{30}, b_{31} and b_{32} and using the final one, the result can be solved for $\underline{q}$:

$$\underline{q} = P_z\underline{v}_z + P_r\underline{v}_r + P_\theta\underline{v}_\theta, \tag{4.64}$$

where

$$P_z = -(b_{30}b_{03} + b_{31}b_{13} + b_{32}b_{23})^{-1}b_{30}b_{00}, \tag{4.65}$$
$$P_r = -(b_{30}b_{03} + b_{31}b_{13} + b_{32}b_{23})^{-1}(b_{30}b_{01} + b_{31}b_{11} + b_{32}b_{21}), \tag{4.66}$$
$$P_\theta = -(b_{30}b_{03} + b_{31}b_{13} + b_{32}b_{23})^{-1}(b_{31}b_{12} + b_{32}b_{22}). \tag{4.67}$$

Equation (4.64) is used in (4.60)–(4.62) to obtain

$$\bar{\omega}\bar{Y} = \bar{B}\bar{Y}, \quad \bar{Y} = (\underline{v}_z, \underline{v}_r, \underline{v}_\theta), \tag{4.68}$$
$$\bar{B} = \begin{bmatrix} b_{00} & b_{01} & 0 \\ 0 & b_{11} & b_{12} \\ 0 & b_{21} & b_{22} \end{bmatrix} + \begin{bmatrix} b_{03}P_z & b_{03}P_r & b_{03}P_\theta \\ b_{13}P_z & b_{13}P_r & b_{13}P_\theta \\ b_{23}P_z & b_{23}P_r & b_{23}P_\theta \end{bmatrix}. \tag{4.69}$$

The generalized eigenvalue problem in equation (4.57) has been reduced to a standard eigenvalue problem and the pressure eliminated. The size of the eigenvalue problem has been decreased: $\bar{B}$ is now a square matrix of size $3N - 6$. Pressure elimination also removes spurious numerical eigenvalues that may arise from the generalized eigenvalue problem (4.57). The problem (4.68) has $3N - 6$ solutions for $\bar{\omega}$ and each solution has corresponding eigenvector $\bar{Y}$ of size $3N-6$. Note that computation of the P's using equations (4.65)–(4.67) requires matrix inversion. The above standard eigenvalue problem is solved using functions of the library LAPACK.

4.5 Validation

Convergence tests which were performed to check the basic-flow and eigenvalue calculations will be briefly discussed in this section. Some results of comparison with the existing literature will also be presented. Additional validation results and convergence checks are provided in chapters 5 and 6.

4.5.1 Basic-flow calculations

Given the finite-difference scheme used for marching in ζ, we expect second-order accuracy in the step size, Δ. This was verified by fixing a maximum of $\zeta = 2$ and varying Δ, while keeping all other parameters constant. The results are compared with a reference case, $\Delta = 0.0001$, the difference being considered as a L^2-norm measure of the error. Figure 4.1a shows a log-log plot

The second integral relation represents the balance of momentum for a small slice in ζ:

$$\int_0^\infty \left[(1+\zeta\sigma)\left(\zeta\frac{\partial V_z^2}{\partial\zeta}-\sigma\frac{\partial V_z^2}{\partial\sigma}\right)+\frac{1}{1+\zeta\sigma}\left(\zeta\frac{\partial\Pi}{\partial\zeta}-\sigma\frac{\partial\Pi}{\partial\sigma}\right)\right]\mathrm{d}\sigma+V_r\mid_{\sigma=\infty}+\frac{\partial V_z}{\partial\sigma}|_{\sigma=0}=0. \tag{4.71}$$

The left-hand side of this equation was computed up to $\zeta = 2$, the results being shown in figure 4.1c. Although not as small as the volume-flux error, the discrepancy between the numerical results and (4.71) is still small, of order 10^{-7}. Note that $N = 64$ was used in figure 4.1b and figure 4.1c. Other values of N and S were also examined. Our conclusion was that the two integral relations are well satisfied.

Lastly, the basic flow solution can be compared with the existing literature. One such comparison will be presented here (other results are given in chapter 5). Figure 4.1d shows comparison of the skin-friction coefficient C_f with the results of Jaffe & Okamura [1968] for the non-rotating case, where the skin-friction coefficient is defined as

$$C_f = \left.\frac{\partial V_z}{\partial\eta_j}\right|_{\eta_j=0}, \tag{4.72}$$

and η_j denotes the radial coordinate used by Jaffe & Okamura [1968]. Excellent agreement between the two results is evident.

4.5.2 Linear-stability code

As discussed in chapter 6 (and as expected for a problem which is semi-infinite in radial direction, see Schmid & Henningson [2001]), the eigenspectrum consists of discrete and continuous parts. Numerically, the continuous spectrum consists of many closely-spaced eigenvalues, lying along a curve in the complex-ω plane, which become more and more densely packed as N is increased. Thus, they approach a continuum in the limit $N \to \infty$. Because the continuous spectrum represents decaying modes, it is unimportant, hence neglected, for stability analysis.

The discrete eigenvalue with the maximum growth rate, ω_i, is of primary interest in stability analysis because it is this mode which controls flow stability. Thus, we studied the sensitivity of this eigenvalue to variations in the numerical parameters, $N, \hat{\sigma}$ and Δ. Note that, although Δ does not appear explicitly in the linear-stability problem, it nonetheless affects the results via the basic-flow calculation. Results of the sensitivity analysis can be found in chapter 6, section 6.3. After studying numerous cases in which both the physical/modal parameters, $\mathrm{Re}, Z, S, \alpha$ and m, and the numerical ones, $N, \hat{\sigma}$ and Δ, were varied, the eigenvalue was found to be second-order convergent in Δ (as expected), insensitive to $\hat{\sigma}$ in the range $2-6$, and rapidly convergent as N was increased. Based on these results, we chose $N = 64, \hat{\sigma} = 5$ and $\Delta = 0.001$ for the main eigenvalue computations. This choice gives better than eight decimal places accuracy for the eigenvalue.

The eigenfunctions of the mode with largest growth rate were also checked for consistency with the large-σ asymptotics (see Schmid & Henningson [2001]): $v_z(\sigma), v_r(\sigma)$ and $v_\theta(\sigma)$ are expected to behave like $\mathrm{e}^{-\bar{\alpha}\sigma}$ as $\sigma \to \infty$. Figure 4.2a shows results for the case $Z = 0.5, \alpha = 0.2, m = 1, \mathrm{Re} = 2000$ and $S = 0.01$. Good agreement is observed.

Figure 4.2b shows the maximum growth rate as a function of z (the maximum is taken over α and all discrete modes), for $\mathrm{Re} = 15000, S = 0$ and $m = 1, 2$. The results are compared with those of Tutty *et al.* [2002] and good agreement is observed.

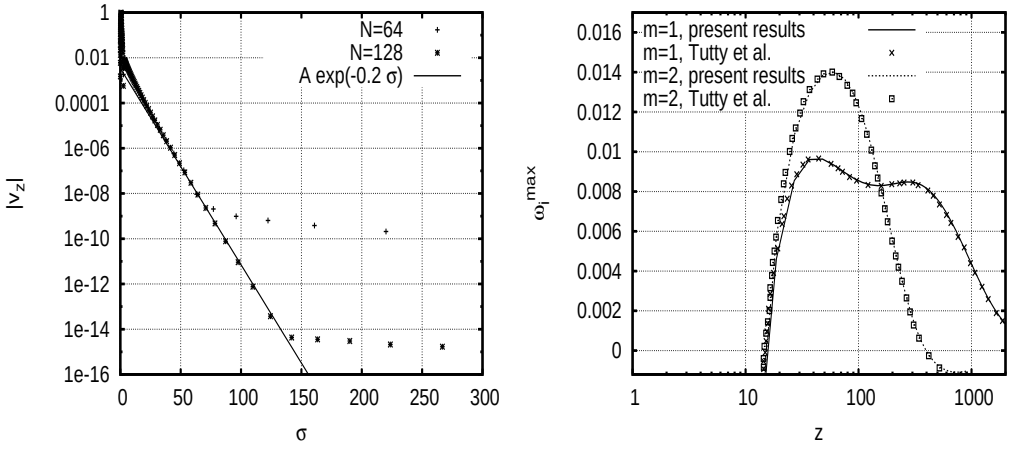

(a) (b)

Figure 4.2: a) Log-log plots of $|v_z|$ as a function of σ for $Z = 0.5, \alpha = 0.2, m = 1, \mathrm{Re} = 2000, S = 0.01$ and $N = 64, 128$ b) Comparisons of maximum growth rate for $\mathrm{Re} = 15000, S = 0, m = 1$ and $m = 2$ with results of Tutty *et al.* [2002]

	Re_c	ζ_c	α_c
T	1060	1.01	0.125
H	1054	1.00	0.125
P	1059	1.01	0.125

Table 4.1: Comparison of results from the present study (P) with those of Tutty *et al.* [2002] (T) and Herrada *et al.* [2008] (H).

In the non-rotating case, it is found that there is a Reynolds number, Re_c, below which the flow is stable (see detailed results in chapter 6) for all z. This is referred to as the global critical Reynolds number by Tutty *et al.* [2002]. Its value was calculated, along with the associated values, ζ_c and α_c. Table 4.1 compares the results with those of Tutty *et al.* [2002] and Herrada *et al.* [2008].

As discussed in section 3.5, although this thesis is devoted to temporal stability analysis of the rotating-cylinder flow, another approach, namely spatial stability, is possible. In this approach, $\bar{\omega}$ is a real parameter and $\bar{\alpha}$ and $\bar{X}$ are determined by the requirement that (4.57) has a nonzero solution (note that B depends on $\bar{\alpha}$). We do not go into details of the numerical methods used to solve this problem, but figure 4.3 shows comparisons of our results with eigenfunctions obtained by Herrada *et al.* [2008] for a particular spatial stability calculation. Note that the eigenfunctions have been scaled to match the normalization used by Herrada *et al.* [2008].

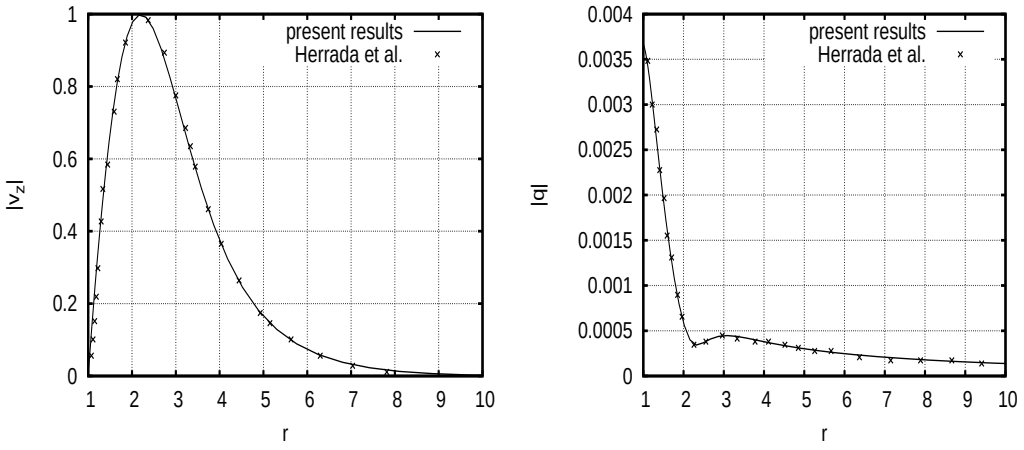

(a) (b)

Figure 4.3: Comparisons of the $|v_z|(r)$ and $|q|(r)$ for the spatial stabilty problem with Re $= 200, m = 1, Z = 0.5, \omega = 0.04$ and $S = 0.1$ with the results of Herrada *et al.* [2008]

Chapter 5

Basic-flow analysis

In this chapter, the results of basic flow around a rotating cylinder are presented in the form of an article published in Proceedings of the Royal Society of London A (Derebail Muralidhar *et al.* [2016b]). The main text, figures and notation used here are the same as in the published article, but the sections and figures are renumbered to ensure consistency with the rest of the manuscript.

Flow around a rotating, semi-infinite cylinder in an axial stream

S. Derebail Muralidhar[1], B. Pier[1], J. F. Scott[1], R. Govindarajan[2]

[1] Laboratoire de mécanique des fluides et d'acoustique (École centrale de Lyon–CNRS—Université de Lyon 1–INSA Lyon), 36 avenue Guy-de-Collongue, F-69134 Écully, France.

[2] Centre for Interdisciplinary Sciences, Tata Institute of Fundamental Research, 21 Brundavan Colony, Narsingi, Hyderabad, 500075, India

Abstract

This paper concerns steady, high-Reynolds-number flow around a semi-infinite, rotating cylinder placed in an axial stream and uses boundary-layer type of equations which apply even when the boundary-layer thickness is comparable to the cylinder radius, as indeed it is at large enough downstream distances. At large rotation rates, it is found that a wall jet appears over a certain range of downstream locations. This jet strengthens with increasing rotation, but first strengthens then weakens as downstream distance increases, eventually disappearing, so the flow recovers a profile qualitatively similar to a classical boundary layer. The asymptotic solution at large streamwise distances is obtained as an expansion in inverse powers of the logarithm of the distance. It is found that the asymptotic radial and axial velocity components are the same as for a non-rotating cylinder, to all orders in this expansion.

5.1 Introduction

When a semi-infinite rotating cylindrical body is placed in a high-Reynolds-number axial flow (see figure 5.1), an axisymmetric boundary layer develops along the cylinder. Initially thin, this layer becomes of thickness comparable with, then larger than the cylinder radius at sufficiently large axial distances. Our original motivation for studying this flow was to undertake a stability analysis. However, it soon became clear that there are very few existing studies of the underlying flow, despite its interesting features, e.g. the appearance of an axial wall jet beyond a certain threshold value of the rotation rate. The presence of curvature and rotation means that the classical Prandtl equations need to be generalized to allow for these effects. In particular, rotation leads to a centrifugal term which couples all three velocity components. This results in significant qualitative changes in the flow structure, e.g. the wall jet, compared with Blasius flow on a flat plate.

The non-rotating version of this problem was studied analytically by Seban & Bond [1951] using a series solution in powers of $z^{1/2}$, where z is the axial coordinate, non-dimensionalized using the cylinder radius. This series solution was limited to order 3, and thus only applicable close to the inlet. Kelly [1954] showed that the series solution for the displacement thickness provided by Seban & Bond [1951] was erroneous, and obtained the correct result. Glauert & Lighthill [1955] extended this work to obtain a solution at all z using the Pohlhausen approximation. At large z, Glauert & Lighthill [1955] also showed that the velocity profile had an asymptotic expansion in inverse powers of $\log(z)$. Jaffe & Okamura [1968] were the first to solve the boundary-layer equations for this problem numerically, thus covering the entire range of z, from small to large values. Boundary-layer velocity profiles have also been numerically determined by Tutty *et al.* [2002] and Vindod & Govindarajan [2012] in the context of stability analysis.

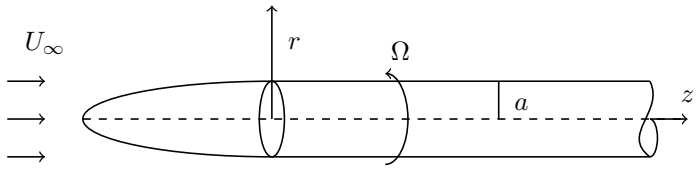

Figure 5.1: Schematic diagram of the problem.

Petrov [1976] appears to be the first to have studied the rotating case. Axial velocity profiles were obtained in the limit of small z and show the existence of a wall jet for sufficiently strong rotation, though this interesting feature was not explained in the paper. Motivated as we were by stability analysis of the flow, Kao & Chow [1991] and Herrada *et al.* [2008] solved the present problem numerically. However, both papers limit themselves to a range of rotation rates insufficiently large to produce a wall jet. Furthermore, the centrifugal term is missing in the boundary-layer equations of Kao & Chow [1991], and so they are incapable of yielding a wall jet even at large rotation rates.

In §2, we define the two non-dimensional control parameters of the problem, Re and S, the Reynolds number and non-dimensional rotation rate. The boundary-layer equations, valid for large Re, and allowing for boundary-layer thickness to be comparable with the cylinder radius are given. These equations generalise the Prandtl equations and apply for arbitrary (not necessarily small) ratios of boundary-layer thickness to cylinder radius. Suitable rescaling of the variables renders the problem independent of Re, leaving only S as control parameter. Section 3 describes the numerical scheme and its verification, while §4 gives results and discussion, in particular focussing on the wall jet. Finally, §5 gives asymptotic analyses of the limits of large $Z = z/\mathrm{Re}$ and large S. The boundary layer on the nose is discussed in the appendices. It is found that the precise shape of the nose is unimportant: the input to the boundary-layer equations of §2 being the Blasius flat-plate flow (generalized to include the azimuthal component due to rotation), independent of the nose shape.

5.2 Boundary-layer equations

A semi-infinite cylinder of radius a rotates about its axis with angular velocity Ω and is placed in an axial stream of incompressible fluid of velocity U_∞ and viscosity ν (see figure 5.1). Assuming large Reynolds number, an initially thin boundary layer develops along the cylinder. If the cylinder were sharply truncated at the nose, flow separation would occur as is usually the case at a salient edge (Batchelor [1967]). To avoid this scenario we assume there is a smooth nose, as shown in figure 5.1. Another way to avoid flow separation would be to consider a thin hollow cylinder. The boundary-layer equations formulated in this section hold good for both these cases. A detailed analysis of the nose region is given in appendix B.

The natural length and velocity scales are a and U_∞. These scales are used to non-dimensionalize the axisymmetric, steady Navier–Stokes equations in cylindrical coordinates, z, r, θ. There are two non-dimensional parameters, namely the Reynolds number

$$\mathrm{Re} = \frac{U_\infty a}{\nu}, \tag{5.1}$$

and the rotation rate

$$S = \frac{\Omega a}{U_\infty}. \tag{5.2}$$

Assuming a large Reynolds number, the length scale for axial variation of the flow is much longer than that for radial variation. This separation of scales leads to the boundary-layer approximation. Thus,

$$u_z\frac{\partial u_z}{\partial z}+u_r\frac{\partial u_z}{\partial r}=-\frac{\partial p}{\partial z}+\frac{1}{\mathrm{Re}}\left(\frac{\partial^2 u_z}{\partial r^2}+\frac{1}{r}\frac{\partial u_z}{\partial r}\right), \tag{5.3}$$

$$\frac{u_\theta^2}{r}=\frac{\partial p}{\partial r}, \tag{5.4}$$

$$u_z\frac{\partial u_\theta}{\partial z}+u_r\frac{\partial u_\theta}{\partial r}+\frac{u_\theta u_r}{r}=\frac{1}{\mathrm{Re}}\left(\frac{\partial^2 u_\theta}{\partial r^2}+\frac{1}{r}\frac{\partial u_\theta}{\partial r}-\frac{u_\theta}{r^2}\right), \tag{5.5}$$

$$\frac{\partial u_z}{\partial z}+\frac{1}{r}\frac{\partial r u_r}{\partial r}=0 \tag{5.6}$$

are obtained by dropping terms of higher order from the Navier–Stokes equations in the usual manner. Note that we have not assumed the boundary layer to be thin compared with the radius. The boundary conditions are

$$u_z=0, u_r=0, u_\theta=S \quad z>0, r=1, \tag{5.7}$$

$$u_z\to 1, u_\theta\to 0, p\to 0 \quad z>0, r\to\infty. \tag{5.8}$$

The above equations contain the azimuthal component, u_θ, of the velocity. This is due to rotation of the cylinder, which induces the centrifugal term on the left-hand side of equation (5.4), leading to a significant radial pressure gradient. Such an effect is not present in classical boundary-layer theory, which predicts near constancy of the pressure across the layer. Compared to the Prandtl equations of a classical boundary layer, equations (5.3)–(5.6) allow for the additional effects of both rotation and curvature. Near the nose the boundary layer is thin compared with the cylinder radius and curvature effects are negligible. But at large z, boundary-thickening eventually makes the thickness comparable to, then larger compared with the radius, and the full set of equations is required.

The above problem needs to be completed by inlet conditions. At distances from the nose of $O(a)$, the boundary layer is thin compared to the radius and is described by the axisymmetric Prandtl equations given in appendix B. On the cylinder (after leaving the nose), these equations become the flat-plate Prandtl equations, and as z increases, we expect the flow to forget the precise initial conditions and to approach the Blasius solution, independent of the nose shape (here, we implicitly suppose the nose length to be of the same order as its diameter). There are, in fact, two asymptotic regions, $z=O(1)$, where the equations of appendix B apply, and $z=O(Re)$, where the boundary-layer thickness is comparable to the cylinder radius and equations (5.3)–(5.8) hold. Matching between these regions requires that the inlet condition be the Blasius solution (generalized to include the azimuthal component due to rotation). The same is true for the case of the hollow cylinder. In either case, equations (5.3)–(5.8) are supplemented by Blasius initial conditions as $z\to 0$.

Introducing the scaled variables

$$R=r, \quad Z=\frac{z}{\mathrm{Re}}, \tag{5.9}$$

$$U_z=u_z, \quad U_r=Ru_r\mathrm{Re}, \quad U_\theta=Ru_\theta, \quad P=R^2p, \tag{5.10}$$

equations (5.3)–(5.8) become

$$U_z\frac{\partial U_z}{\partial Z}+\frac{U_r}{R}\frac{\partial U_z}{\partial R}=-\frac{1}{R^2}\frac{\partial P}{\partial Z}+\frac{\partial^2 U_z}{\partial R^2}+\frac{1}{R}\frac{\partial U_z}{\partial R}, \tag{5.11}$$

$$U_\theta^2=R\frac{\partial P}{\partial R}-2P, \tag{5.12}$$

$$U_z\frac{\partial U_\theta}{\partial Z}+\frac{U_r}{R}\frac{\partial U_\theta}{\partial R}=\frac{\partial^2 U_\theta}{\partial R^2}-\frac{1}{R}\frac{\partial U_\theta}{\partial R}, \tag{5.13}$$

$$\frac{\partial U_z}{\partial Z}+\frac{1}{R}\frac{\partial U_r}{\partial R}=0, \tag{5.14}$$

$$U_z=U_r=0, U_\theta=S \quad R=1, \tag{5.15}$$

$$U_z\to 1, U_\theta=0, P=0 \quad R\to\infty. \tag{5.16}$$

It is apparent that, using these scalings, Re has disappeared from the problem, leaving S as the only non-dimensional parameter. This result indicates, among other things, that the natural scaling of the axial coordinate is $z=O(\mathrm{Re})$. Thus, as noted earlier, the distance needed for the boundary-layer thickness to become comparable with the radius is Re times the radius. The factors of R appearing in equation (5.10) have been introduced to improve numerical convergence.

5.3 Numerical scheme and validation

The boundary-layer thickness goes to zero like $Z^{1/2}$ and $U_r\to\infty$ like $Z^{-1/2}$ as $Z=0$ is approached. To maintain numerical accuracy in the presence of such singular behaviour, we introduce the variables

$$\zeta=(2Z)^{\frac{1}{2}}, \quad \sigma=\frac{R-1}{\zeta}, \quad V_r=\zeta U_r, \quad V_z=U_z, \quad V_\theta=U_\theta. \tag{5.17}$$

Here, the boundary-layer thickness is prevented from going to zero in the radial coordinate σ by dividing $R-1$ by ζ. V_r is kept finite by use of the factor ζ and ζ is used in place of Z to make the solution a smooth function of the axial coordinate. Using these variables in the boundary-layer equations (5.11)–(5.16) results in

$$\zeta V_z\frac{\partial V_z}{\partial\zeta}+\left(\frac{V_r-\zeta}{R}-\sigma V_z\right)\frac{\partial V_z}{\partial\sigma}=\frac{1}{R^2}(\sigma\frac{\partial P}{\partial\sigma}-\zeta\frac{\partial P}{\partial\zeta})+\frac{\partial^2 V_z}{\partial\sigma^2}, \tag{5.18}$$

$$\frac{\zeta}{R}\left(V_\theta^2+2P\right)=\frac{\partial P}{\partial\sigma}, \tag{5.19}$$

$$\zeta V_z\frac{\partial V_\theta}{\partial\zeta}+\left(\frac{V_r+\zeta}{R}-\sigma V_z\right)\frac{\partial V_\theta}{\partial\sigma}=\frac{\partial^2 V_\theta}{\partial\sigma^2}, \tag{5.20}$$

$$\zeta\frac{\partial V_z}{\partial\zeta}-\sigma\frac{\partial V_z}{\partial\sigma}+\frac{1}{R}\frac{\partial V_r}{\partial\sigma}=0, \tag{5.21}$$

with the boundary conditions

$$V_z=V_r=0, V_\theta=S \quad \sigma=0, \tag{5.22}$$

$$V_z\to 1, V_\theta=0, P=0 \quad \sigma\to\infty. \tag{5.23}$$

These equations govern the axial evolution of the flow. The inlet condition (Blasius solution) is obtained by setting $\zeta=0$ and solving the resulting equations.

The radial coordinate σ is discretized using Chebyshev collocation points:

$$x_n = \cos\left(\frac{n\pi}{N-1}\right) \quad 0 \leq n < N, \tag{5.24}$$

$$\sigma_n = \frac{\hat{\sigma}(1+x_n)}{1-x_n}, \quad x \in [-1,1] \rightarrow \sigma \in [0,\infty]. \tag{5.25}$$

The parameter $\hat{\sigma}$ controls the distribution of points such that half of them lie between $0 \leq \sigma \leq \hat{\sigma}$. The velocities V_z and V_θ are represented by their values at all collocation points. However, since there is no boundary condition for the pressure at the surface, it is represented at all points except $\sigma = 0$. Similarly, there is no boundary condition for V_r at $\sigma = \infty$ and so it is represented at all points apart from $\sigma = \infty$. The Chebyshev derivative matrices for P and V_r are correspondingly modified (e.g. appendix A in Scott [2013]).

The coordinate ζ is discretised using small, equally-spaced steps, $\zeta_i = i\Delta$, and the variables V_z, V_r, V_θ, P are represented by their values at ζ_i. Equations (5.18), (5.20) and (5.21) are evaluated at mid-step, $\zeta_{i+\frac{1}{2}}$, using an implicit scheme that employs centered finite differencing to represent the ζ-derivatives. Equation (5.19) is evaluated at the step position ζ_i, rather than at the midstep. At each step, the equations are solved using Newton–Raphson iteration, thus allowing forward marching. The inlet solution is obtained from equations (5.18)–(5.23) using $\zeta = 0$. Following discretization in σ using the collocation points, the result is again obtained by Newton–Raphson iteration.

The code was first tested by changing the numerical parameters $N, \hat{\sigma}, \Delta$, and observing the dependence of the solution on these parameters. Based on the convergence results we decided to use $N = 128, \hat{\sigma} = 5, \Delta = 0.001$ in our computations. These values gave convergence to better than seven decimal places. The code was also tested using the volume-flux and momentum balance equations. The results respect these equations to seven decimal places. Although use of the Blasius solution at the inlet has earlier been justified by an asymptotic argument, it is interesting to see the effect of a change in inlet profile on the solution. Thus we modified the inlet profile to be $U_z^* = U_z + A\sigma\exp(-0.5\sigma)$, where U_z is the Blasius profile. Taking $A = 2$, it was found that the change in the U_z at $Z = 2$ was in the sixth decimal place. This illustrates the fact that the flow forgets the initial condition as Z increases and becomes insensitive to the precise inlet profile used.

We also validated the code by comparing our results with the existing literature. Tutty *et al.* [2002] studied the case without rotation. The axial (x_t) and radial (σ_t) coordinates used by Tutty *et al.* [2002] are related to those used here via $x_t/\mathrm{Re} = Z$ and $\sigma_t = \sqrt{2}\sigma$. Figure 4.5 shows good agreement with our results for $\mathrm{Re} = 10^4$, $x_t = 0.01$ and $x_t = 10^5$. Herrada *et al.* [2008] considered the problem of the rotating cylinder. They do not give velocity profiles, but rather the skin friction on the cylinder:

$$\tau = \left.\frac{\partial U_z(Z)}{\partial R}\right|_{R=1} = \frac{1}{\zeta}\left.\frac{\partial V_z(\zeta)}{\partial \sigma}\right|_{\sigma=0}. \tag{5.26}$$

Figure 4.5 shows τ as a function of Z for $S = 1$ and good agreement is apparent.

5.4 Results

Flow profiles were obtained for different values of S and Z. Figure 5.3 shows velocity profiles for $S = 0.1$ and different values of Z. For $Z = 0$, $V_z(\sigma)$ corresponds to the Blasius flat-plate solution. As Z increases, $V_z(\sigma)$ deviates from the Blasius profile due to cylinder curvature and rotation. It

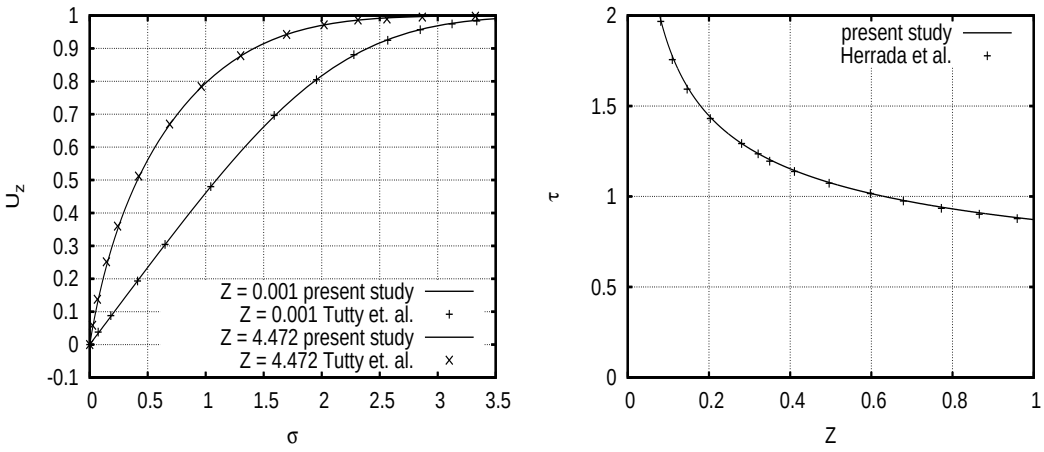

(a) (b)

Figure 5.2: Comparison of U_z for $S = 0$ at two values of Z with Tutty *et al.* [2002] and comparison of skin friction τ for $S = 1$ with Herrada *et al.* [2008].

should be borne in mind that the boundary-layer thickness increases with Z, although this is not apparent in the figure because the scaled radial coordinate $\sigma = (R-1)/\zeta$ has been used. Note that the azimuthal velocity at $Z = 0$ is $V_\theta(\sigma) = S\big(1 - V_z(\sigma)\big)$. As Z increases, small departures from this profile arise.

Figure 5.4 and figure 5.5 show results for $Z = 0.5$ and different values of S. When $S \lesssim 1$, $V_z(\sigma)$ is a modified Blasius profile. However, for $S \gtrsim 4$, $V_z(\sigma)$ is no longer monotonic having a maximum at finite σ. At large S, the maximum is large and the profile is better described as an axial wall jet, rather than a boundary layer. At first sight, it is perhaps surprising that increasing the rotation rate leads to a stronger and stronger axial flow. Increasing S causes V_θ to increase (see figure 5.4). This in turn produces an increasing radial pressure gradient due to the centrifugal force. Since the pressure is constant outside the boundary layer, the pressure within the layer drops (see figure 5.5) with Z. The development of the flow means that the axial presure gradient becomes larger and larger, thus driving a strong axial wall jet. Whereas for lower values of S, boundary-layer thickening leads to positive V_r, at large S entrainment by the wall jet gives negative V_r outside the layer (see figure 5.4).

The existence of a wall jet at large S is apparent in the axial velocity profiles given by Petrov [1976]. However, that article only gives such profiles for the case of small Z (thin boundary layer) and no explanation is provided. Petrov [1976] also gives the maximum axial velocity $U_z^{\max} = \max_R(U_z(R))$ as a function of Z. Figure 5.6 shows a comparison with our results. A small difference is apparent, the origin of which is unclear.

Figure 5.7 shows contours of constant $U_z^{\max}$ in the (S, ζ)-plane as well as the boundary (solid line) separating the region in which $U_z^{\max} = 1$ from that in which $U_z^{\max} > 1$ (which we interpret as indicating a wall jet). It will be seen that there is a threshold, $S = 4.15$, below which $U_z^{\max} = 1$. Above this value, the wall jet exists for some range of axial position. Note that, whatever the strength of rotation, the wall jet eventually disappears sufficiently far downstream.

The thickness of the boundary layer/wall jet can be measured using

$$\delta = \frac{1}{U_z^{\max}} \int_1^\infty |1 - U_z| \mathrm{d}R. \tag{5.27}$$

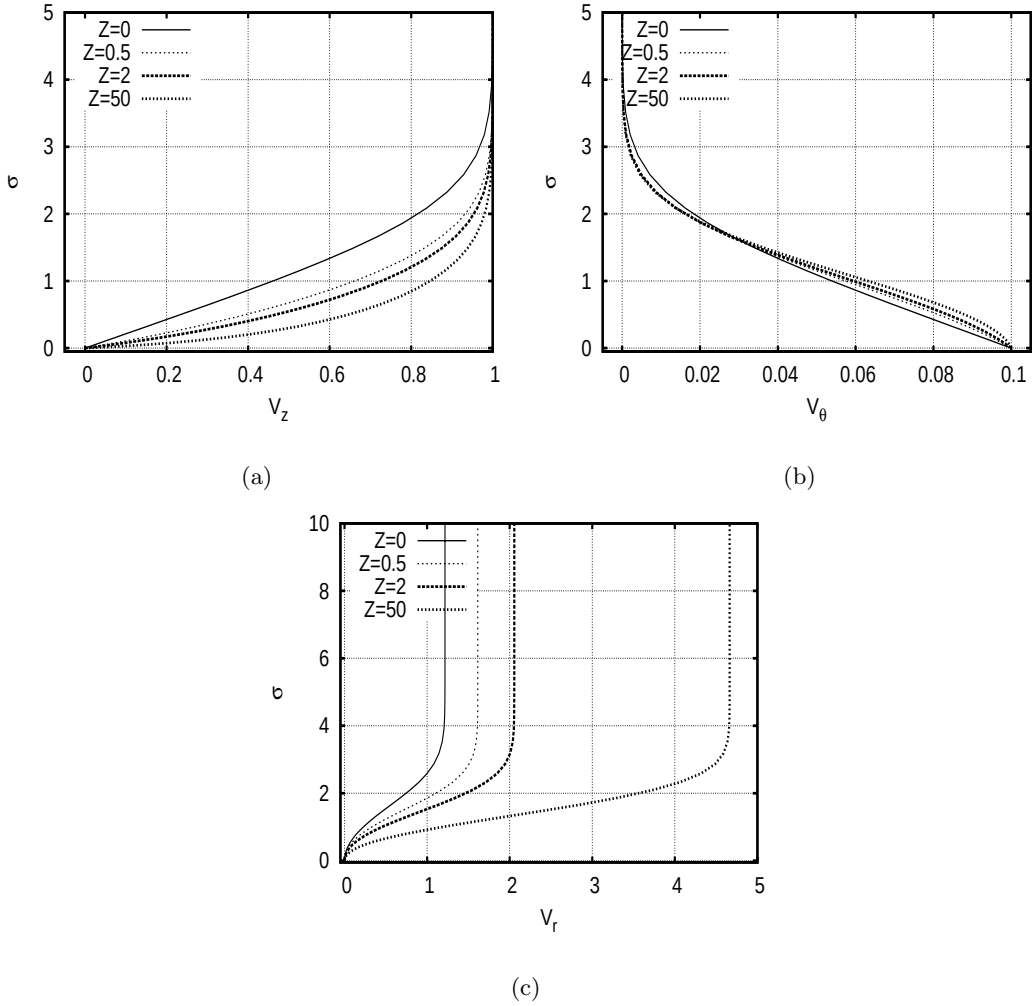

Figure 5.3: Velocity profiles $V_z(\sigma)$, $V_\theta(\sigma)$ and $V_r(\sigma)$ for different axial positions Z at $S = 0.1$.

The absolute value is taken to make the integral always positive and the division by $U_z^{\max}$ allows for the strong wall jets which arise at large S. Figure 5.8 shows $\delta(Z)$ for different values of S. The layer thickness is seen to increase with Z in a roughly parabolic manner (recall that the thickness behaves as $Z^{\frac{1}{2}}$ for small Z). Thickening of the layer is due to viscous diffusion in the usual manner. Increasing S causes the layer to become thinner. At large S, the wall jet is of increasing strength. Viscous diffusion competes with axial convection, the latter being of growing importance, hence the decrease of δ with increasing S.

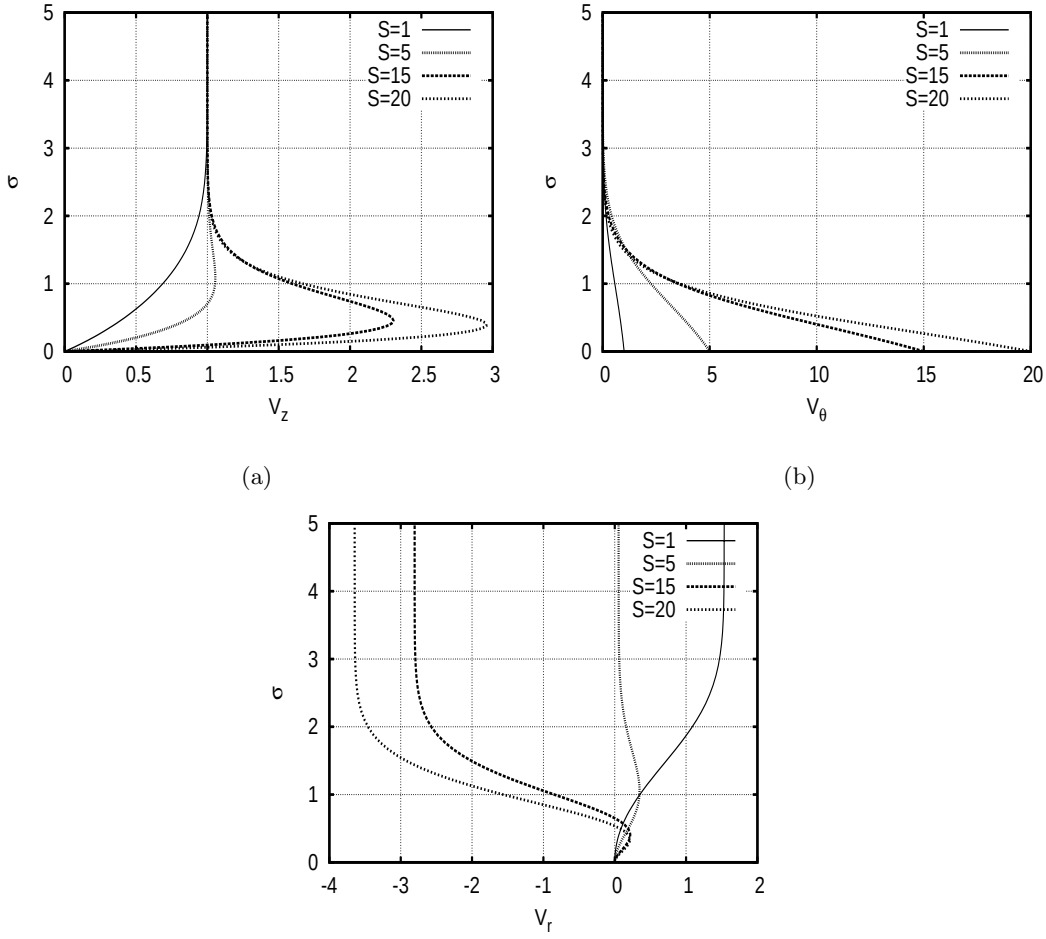

(a) (b)

(c)

Figure 5.4: Velocity profiles $V_z(\sigma)$, $V_\theta(\sigma)$ and $V_r(\sigma)$ at $Z = 0.5$ for different values of rotation rate S.

5.5 Asymptotic analysis

5.5.1 Large-Z asymptotics

Suitable coordinates are

$$\eta = R/\zeta, \quad \chi = \ln(\zeta). \tag{5.28}$$

Here, we have followed Glauert & Lighthill [1955], who used a logarithmic axial coordinate for the non-rotating cylinder problem. This coordinate reflects slower and slower evolution of the flow in the streamwise direction as Z increases. Using these coordinates, equations (5.11)–(5.16)

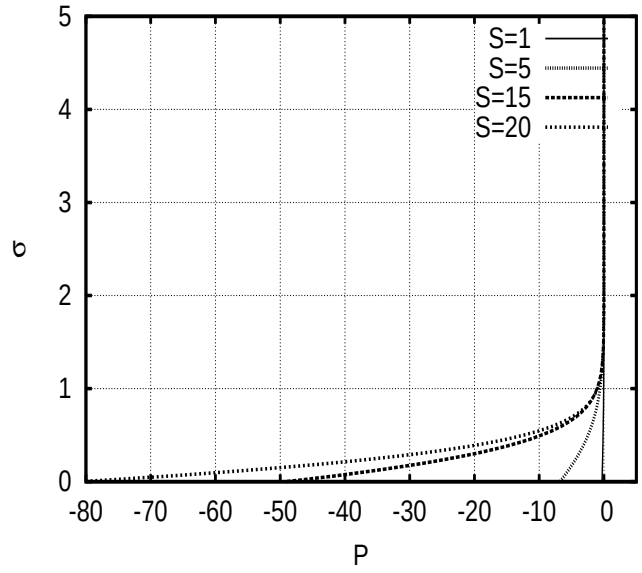

Figure 5.5: Pressure profile $P(\sigma)$ at $Z = 0.5$ for different values of S.

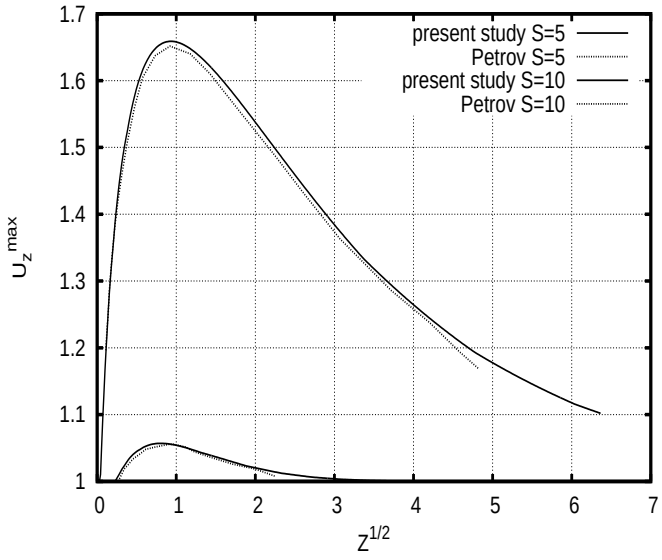

Figure 5.6: Comparison of $U_z^{\max}$ as a function of $Z^{1/2}$ obtained by the present study with Petrov [1976] for the case of $S = 5$ and $S = 10$.

become

$$U_z\left(\frac{\partial U_z}{\partial \chi} - \eta\frac{\partial U_z}{\partial \eta}\right) + \frac{U_r}{\eta}\frac{\partial U_z}{\partial \eta} = \frac{\mathrm{e}^{-2\chi}}{\eta^2}\left(\eta\frac{\partial P}{\partial \eta} - \frac{\partial P}{\partial \chi}\right) + \frac{\partial^2 U_z}{\partial \eta^2} + \frac{1}{\eta}\frac{\partial U_z}{\partial \eta}, \tag{5.29}$$

$$U_\theta^2 + 2P = \eta\frac{\partial P}{\partial \eta}, \tag{5.30}$$

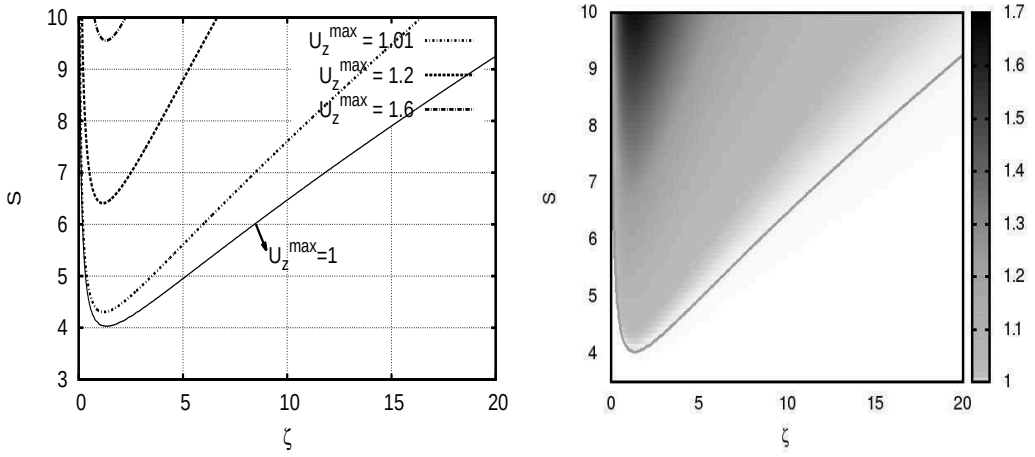

(a) (b)

Figure 5.7: Grayscale plot of $U_z^{\max}$ alongside a contour plot of $U_z^{\max}$. The figure also shows the boundary (solid line) between $U_z^{\max} = 1$ and $U_z^{\max} > 1$.

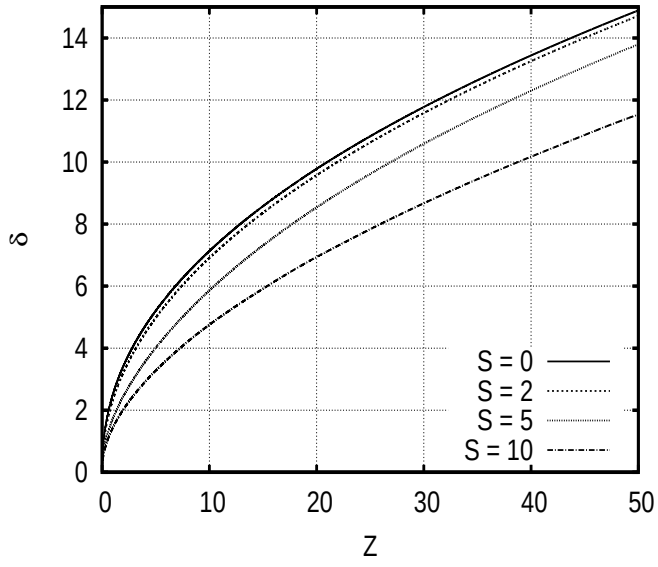

Figure 5.8: Boundary-layer/wall-jet thickness δ versus Z for different values of S.

$$U_z\left(\frac{\partial U_\theta}{\partial \chi} - \eta\frac{\partial U_\theta}{\partial \eta}\right) + \frac{U_r}{\eta}\frac{\partial U_\theta}{\partial \eta} = \frac{\partial^2 U_\theta}{\partial \eta^2} - \frac{1}{\eta}\frac{\partial U_\theta}{\partial \eta}, \tag{5.31}$$

$$\frac{\partial U_z}{\partial \chi} - \eta\frac{\partial U_z}{\partial \eta} + \frac{1}{\eta}\frac{\partial U_r}{\partial \eta} = 0, \tag{5.32}$$

$$U_z = U_r = 0, U_\theta = S \quad \eta = e^{-\chi}, \tag{5.33}$$

$$U_z \to 1, U_\theta \to 0, P \to 0 \quad \eta \to \infty. \tag{5.34}$$

It is shown in appendix A that U_z, U_r, U_θ and P have asymptotic expansions in powers of χ^{-1}. The factor of $\mathrm{e}^{-2\chi}$ in equation (5.29) is exponentially small and is hence negligible at all algebraic orders. Without the corresponding term in equation (5.29), U_z and U_r decouple from U_θ and P, though the latter depends on the former. Thus, we expect such decoupling to hold at all orders. This is indeed what is found in appendix A, where the governing equations for the coefficients of the expansions in powers of χ^{-1} are obtained for all orders. Given decoupling, rotation does not enter into the asymptotics of U_z and U_r, which are consequently the same as for the non-rotating case.

Glauert & Lighthill [1955] studied the case without rotation and obtained the expansions of U_z and U_r. Appendix A extends the analysis to include rotation and gives detailed results up to order 5. At first order, the asymptotic solution can be obtained analytically and is given by

$$U_z \sim 1 - \chi^{-1} \int_\eta^\infty \frac{\mathrm{e}^{-\xi^2/2}}{\xi} \mathrm{d}\xi, \tag{5.35}$$

$$U_r \sim \chi^{-1}(1 - \mathrm{e}^{-\eta^2/2}), \tag{5.36}$$

$$U_\theta \sim S\mathrm{e}^{-\eta^2/2}, \tag{5.37}$$

$$P \sim -S^2\eta^2 \int_\eta^\infty \frac{\mathrm{e}^{-\xi^2}}{\xi^3} \mathrm{d}\xi. \tag{5.38}$$

In figure 5.9, the results for U_z show convergence to the asymptotic form (5.35), while those for $u_\theta = U_\theta/R$ converge to $u_\theta \sim S/R$, which is the flow due to a rotating cylinder, infinite in both axial directions (rather than semi-infinite) and without axial flow.

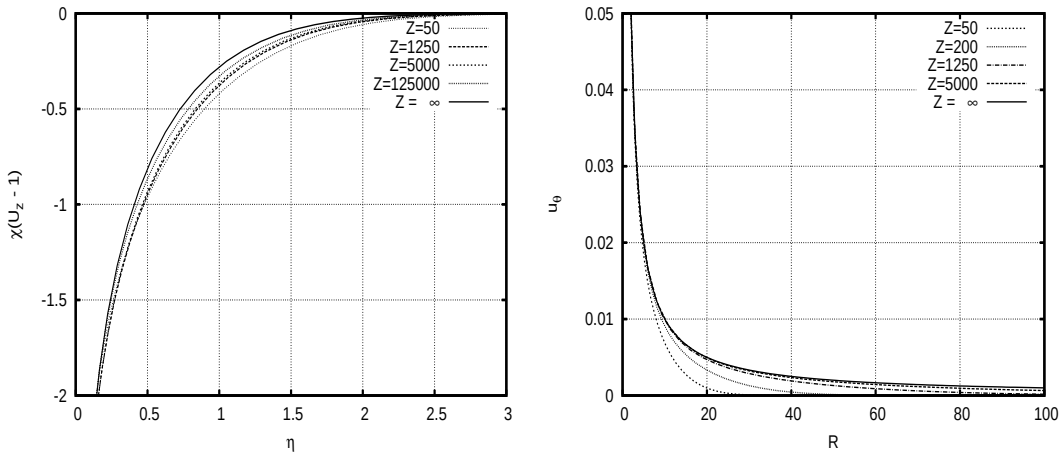

(a) (b)

Figure 5.9: Comparison of $\chi(U_z - 1)$ and $u_\theta = U_\theta/R$ for different values of Z at $S = 0.1$ with the $Z \to \infty$ solution.

5.5.2 Large-S asymptotics

As we saw in the previous section, the numerical results show the existence of a wall jet at large S. In this limit, appropriate scaled variables are

$$Z^* = \frac{Z}{S}, \quad R^* = R, \tag{5.39}$$

$$U_z^* = \frac{U_z}{S}, \quad U_r^* = U_r, \quad U_\theta^* = \frac{U_\theta}{S}, \quad P^* = \frac{P}{S^2}. \tag{5.40}$$

The scaling of Z reflects the increasing distance required for flow development as the rotation rate increases. The scaling of U_z and U_θ indicates the strengthening flow velocity as S increases. The large-S asymptotic expansions of U_z^*, U_r^*, U_θ^* and P^* proceed as powers of S^{-1}. At leading order (S^0), we find

$$U_z^* \frac{\partial U_z^*}{\partial Z^*} + \frac{U_r^*}{R^*}\frac{\partial U_z^*}{\partial R^*} = -\frac{1}{R^{*2}}\frac{\partial P^*}{\partial Z^*} + \frac{\partial^2 U_z^*}{\partial R^{*2}} + \frac{1}{R^*}\frac{\partial U_z^*}{\partial R^*}, \tag{5.41}$$

$$U_\theta^{*2} = R^*\frac{\partial P^*}{\partial R^*} - 2P^*, \tag{5.42}$$

$$U_z^* \frac{\partial U_\theta^*}{\partial Z^*} + \frac{U_r^*}{R^*}\frac{\partial U_\theta^*}{\partial R^*} = \frac{\partial^2 U_\theta^*}{\partial R^{*2}} - \frac{1}{R^*}\frac{\partial U_\theta^*}{\partial R^*}, \tag{5.43}$$

$$\frac{\partial U_z^*}{\partial Z^*} + \frac{1}{R^*}\frac{\partial U_r^*}{\partial R^*} = 0, \tag{5.44}$$

with the following inlet and boundary conditions

$$U_z^* = 0, U_\theta^* = 0 \quad Z^* = 0, \tag{5.45}$$

$$U_z^* = 0, U_r^* = 0, U_\theta^* = 1 \quad R^* = 1, \tag{5.46}$$

$$U_z^* = 0, U_\theta^* = 0, P^* = 0 \quad R^* \to \infty. \tag{5.47}$$

Figure 5.10 shows the solution of the above problem (solid line) compared with the numerical results discussed before for $Z^* = 0.1$ and different values of S. It is apparent that the asymptotics are indeed approached as $S \to \infty$. Figure 5.11 shows the leading-order asymptotic solution for different values of Z^*. We see that the large-Z limit ($u_\theta \sim SR^{-1}$) is approached by u_θ as $Z^* \to \infty$.

Note that the limit $S \to \infty$ can be reached in two ways: either by increasing the rotation rate, or by decreasing the velocity U_∞ to zero. Note also that u_z/S and u_θ/S are the velocity components non-dimensionalized by Ωa, rather than U_∞, and that $Z^* = z/\mathrm{Re}_\Omega$, where $\mathrm{Re}_\Omega = \Omega a^2/\nu$ is the Reynolds number based on the rotational velocity Ωa. Thus figure 5.11 can be interpreted as showing the flow due to a rotating, semi-infinite cylinder in a still fluid ($U_\infty = 0$). It can be shown that the separation of radial and axial length scales, which underlies the boundary-layer type approximation we have used, is valid if either of the Reynolds numbers, Re or Re_Ω, is large.

5.6 Conclusion

In this paper we have presented a study of the flow around a rotating cylinder in an axial stream. We have assumed a smooth nose to avoid flow separation. The two non-dimensional control parameters of the problem are: Reynolds number (Re) and rotation rate (S). The flow equations are formulated using a boundary-layer type approximation, appropriate at large

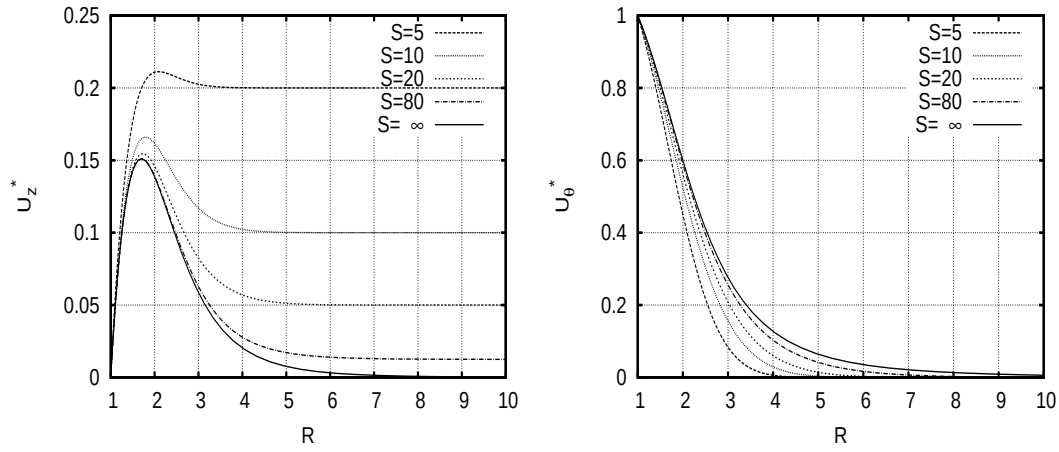

(a) (b)

Figure 5.10: Comparison of U_z^* and U_θ^* for different values of S and $Z^* = 0.1$ with the $S \to \infty$ asymptotic solution.

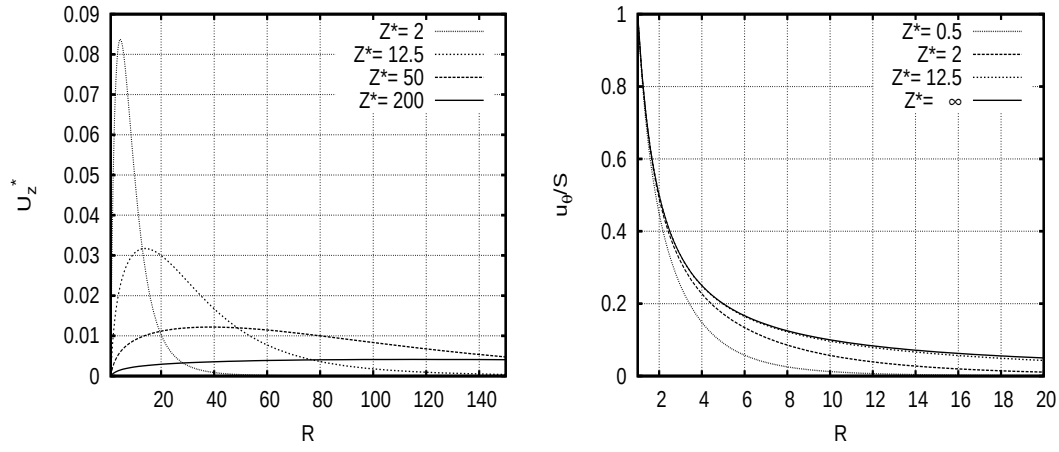

(a) (b)

Figure 5.11: $u_z/S = U_z^*$ and u_θ/S at different values of Z^* for a rotating cylinder in the limit $S \to \infty$.

Reynolds numbers and in which the flow is assumed to evolve slowly in the streamwise direction in comparison to the radial direction. The resulting equations are not limited to the case in which the boundary layer is thin compared with the cylinder radius. By using appropriate scalings we remove Re from the problem.

The results show that the boundary-layer thickness increases with axial distance, becoming comparable with the cylinder radius a at distances of $O(\mathrm{Re}\ a)$. Prior to this, the layer is thin compared to the radius and the flow is close to the Blasius profile of a flat plate. However, it differs from the Blasius solution due to effects of curvature and rotation at larger downstream distances. As S increases, the centrifugal force creates an increasing radial pressure gradient,

which combined with axial development, implies an increasing axial gradient of pressure. Above $S = 4.15$, the maximum velocity exceeds the free-stream velocity for a range of Z and we say that a wall jet exists. This jet becomes stronger and stronger as $S \to \infty$.

In the limit of large Z, we find that the axial and radial components of velocity decouple from the azimuthal velocity component and pressure. All these quantities are found to have asymptotic expansions in inverse powers of $\ln(Z)$, a result already obtained for the non-rotating case by Glauert & Lighthill [1955], and here extended to include rotation. The leading-order term in the u_θ expansion is $u_\theta \sim SR^{-1}$, which is the flow expected for a rotating cylinder, infinite in both directions. Because U_θ becomes independent of Z, the same is true of the pressure field resulting from the centrifugal force, hence the absence of an axial pressure gradient to drive the axial/radial flow. This is the reason for the decoupling.

When S is large, we introduce appropriate scalings for Z, U_z, U_θ and P. The asymptotic expansions of the scaled velocity and pressure proceed as inverse powers of S, beginning with S^0. The leading-order term describes an axial wall jet due to a rotating cylinder in a fluid at rest.

Appendix A. Large Z asymptotic expansions

The flow variables are expressed as asymptotic expansions in inverse powers of χ:

$$U_z \sim 1 + \sum_{n=1}^{\infty} \chi^{-n} U_z^{(n)}(\eta), \tag{5.48}$$

$$U_r \sim \sum_{n=1}^{\infty} \chi^{-n} U_r^{(n)}(\eta), \tag{5.49}$$

$$U_\theta \sim S \sum_{n=1}^{\infty} \chi^{-n+1} U_\theta^{(n)}(\eta), \tag{5.50}$$

$$P \sim S^2 \sum_{n=1}^{\infty} \chi^{-n+1} P^{(n)}(\eta). \tag{5.51}$$

Introducing these expansions into equations (5.29)–(5.32) gives

$$\frac{1}{\eta}\frac{\mathrm{d}}{\mathrm{d}\eta}\left(\eta \frac{\mathrm{d}U_z^{(n)}}{\mathrm{d}\eta}\right) + \eta \frac{\mathrm{d}U_z^{(n)}}{\mathrm{d}\eta} = \phi_z^{(n)}, \tag{5.52}$$

$$\eta^3 \frac{\mathrm{d}}{\mathrm{d}\eta}\left(\frac{P^{(n)}}{\eta^2}\right) = \psi^{(n)}, \tag{5.53}$$

$$\eta \frac{\mathrm{d}}{\mathrm{d}\eta}\left(\frac{1}{\eta}\frac{\mathrm{d}U_\theta^{(n)}}{\mathrm{d}\eta}\right) + \eta \frac{\mathrm{d}U_\theta^{(n)}}{\mathrm{d}\eta} = \phi_\theta^{(n)}, \tag{5.54}$$

$$\frac{1}{\eta}\frac{\mathrm{d}U_r^{(n)}}{\mathrm{d}\eta} - \eta \frac{\mathrm{d}U_z^{(n)}}{\mathrm{d}\eta} = \phi_r^{(n)}, \tag{5.55}$$

where

$$\phi_z^{(n)} = (1-n)U_z^{(n-1)} + \sum_m \left(\left(\frac{U_r^{(m)}}{\eta} - \eta U_z^{(m)} \right) \frac{\mathrm{d}U_z^{(n-m)}}{\mathrm{d}\eta} - mU_z^{(m)} U_z^{(n-m-1)} \right), \tag{5.56}$$

$$\phi_\theta^{(n)} = (2-n)U_\theta^{(n-1)} + \sum_m \left(\left(\frac{U_r^{(m)}}{\eta} - \eta U_z^{(m)} \right) \frac{\mathrm{d}U_\theta^{(n-m)}}{\mathrm{d}\eta} - (m-1)U_\theta^{(m)} U_z^{(n-m-1)} \right), \tag{5.57}$$

$$\phi_r^{(n)} = (n-1)U_z^{(n-1)}, \quad \psi^{(n)} = \sum_m U_\theta^{(m)} U_\theta^{(n-m+1)}. \tag{5.58}$$

Equations (5.52)–(5.55) are to be solved, along with appropriate boundary conditions (which will be derived shortly), for the nth-order coefficients of the expansions, $U_z^{(n)}, U_r^{(n)}, U_\theta^{(n)}$ and $P^{(n)}$ ($n \geq 1$). It should be noted that, in equations (5.56)–(5.58), $U_z^{(m)}$, $U_r^{(m)}$ and $U_\theta^{(m)}$ are to be interpreted as zero when $m \leq 0$. The governing equations for $U_z^{(n)}$ and $U_r^{(n)}$ are independent of $U_\theta^{(n)}$ and $P^{(n)}$. Thus, the asymptotics of $U_z^{(n)}$ and $U_r^{(n)}$ are the same as for a non-rotating cylinder and are governed by equations (5.52), (5.55), (5.56) and the first of the equations (5.58). $U_\theta^{(n)}$ is determined by equations (5.54) and (5.57), while $P^{(n)}$ follows from equation (5.53) and the second of the equations (5.58). Note that $\phi_z^{(n)}, \phi_r^{(n)}$ and $\phi_\theta^{(n)}$ depend only on the solution at lower orders than n, suggesting a method which proceeds from $n = 1$ to successively higher values of n.

The boundary conditions at $\eta \to \infty$ are

$$U_z^{(n)} = U_\theta^{(n)} = P^{(n)} = 0. \tag{5.59}$$

Application of the boundary conditions (5.15) at the cylinder surface requires the introduction of an inner region, $R = O(1)$, represented by the expansions

$$U_z \sim \sum_{n=1}^{\infty} \chi^{-n} \hat{U}_z^{(n)}(R), \tag{5.60}$$

$$U_r \sim \sum_{n=1}^{\infty} \chi^{-n} \hat{U}_r^{(n)}(R), \tag{5.61}$$

$$U_\theta \sim S \sum_{n=1}^{\infty} \chi^{-n+1} \hat{U}_\theta^{(n)}(R), \tag{5.62}$$

$$P \sim S^2 \sum_{n=1}^{\infty} \chi^{-n+1} \hat{P}^{(n)}(R). \tag{5.63}$$

Equations (5.11), (5.13) and (5.14) are rewritten using the axial coordinate χ in place of Z. Equation (5.14) yields

$$\frac{\partial \hat{U}_r^{(n)}}{\partial R} = 0, \tag{5.64}$$

which, together with the boundary conditions (5.15) gives $\hat{U}_r^{(n)} = 0$. Equations (5.11) and (5.13) imply

$$\frac{\partial^2 \hat{U}_z^{(n)}}{\partial R^2} + \frac{1}{R} \frac{\partial \hat{U}_z^{(n)}}{\partial R} = 0, \tag{5.65}$$

$$\frac{\partial^2 \hat{U}_\theta^{(n)}}{\partial R^2} - \frac{1}{R} \frac{\partial \hat{U}_\theta^{(n)}}{\partial R} = 0, \tag{5.66}$$

hence

$$\hat{U}_z^{(n)}(R) = A_n \ln R + B_n, \tag{5.67}$$

$$\hat{U}_\theta^{(n)}(R) = C_n R^2 + D_n. \tag{5.68}$$

The boundary conditions (5.15) imply $B_n = 0$, $C_1 + D_1 = 1$, and $C_n + D_n = 0$ for $n > 1$.

Recalling that $R = \zeta\eta = e^\chi\eta$, the inner expansions give

$$U_z \sim A_1 + \sum_{n=1}^{\infty} \chi^{-n}(A_n \ln\eta + A_{n+1}), \tag{5.69}$$

$$U_\theta \sim S\left(1 + \sum_{n=1}^{\infty} C_n\chi^{-n}(e^{2\chi}\eta^2 - 1)\right), \tag{5.70}$$

$$U_r \sim 0, \tag{5.71}$$

when expressed in terms of the outer coordinate, η. Matching requires $A_1 = 1$, $C_n = 0$ and

$$U_z^{(n)} \sim A_n \ln\eta + A_{n+1}, \tag{5.72}$$

$$U_\theta^{(1)} \to 1 \quad \text{and} \quad U_\theta^{(n)} \to 0 \quad \text{for} \quad n > 1, \tag{5.73}$$

$$U_r^{(n)} \to 0, \tag{5.74}$$

as $\eta \to 0$. It follows from (5.72) that

$$\eta\frac{\mathrm{d}U_z^{(n)}}{\mathrm{d}\eta} \to A_n \tag{5.75}$$

and

$$A_{n+1} = \lim_{\eta\to 0}\left(U_z^{(n)} - A_n\ln\eta\right). \tag{5.76}$$

Assuming A_n is known, equations (5.52)–(5.58) and the boundary conditions (5.59) and (5.73)–(5.75) can be solved for $U_z^{(n)}$, $U_r^{(n)}$, $U_\theta^{(n)}$ and $P^{(n)}$. $A_1 = 1$ gets the process started and leads to the leading-order outer solution, (5.35)–(5.38), in agreement with Glauert & Lighthill [1955]. Equation (5.76) gives A_n at the next order, allowing solution at successively higher orders. It can be shown that

$$U_z^{(n)} = A_n\ln\eta + A_{n+1} + O(\eta^2\ln^{p_n}\eta), \quad U_\theta^{(n)} = 1 - q_n + O(\eta^2), \quad U_r^{(n)} = O(\eta^2\ln^{q_n}\eta), \tag{5.77}$$

as $\eta \to 0$, where $q_n = p_{n+1} - 1, p_1 = 0, p_2 = 1$ and $p_n = 2$ for $n \geq 3$. The terms in (5.77) indicated by the $O()$ notation are exponentially small in the inner region, while the remaining ones reproduce the inner solution. Thus, the outer expansions in fact apply in the inner region.

The above procedure has been implemented numerically and results up to $n = 5$ are presented in figure 5.12. Figure 5.13 shows the comparison of numerical solution of U_z at $Z = 5000$ and $S = 1$ with the asymptotic solution obtained by truncating at different orders n. Although this result shows good convergence, and therefore further confirms both numerical and analytical results, it should be borne in mind that the expansions (5.48)–(5.51) are, in fact, asymptotic as $Z \to \infty$, rather than necessarily convergent at any finite Z.

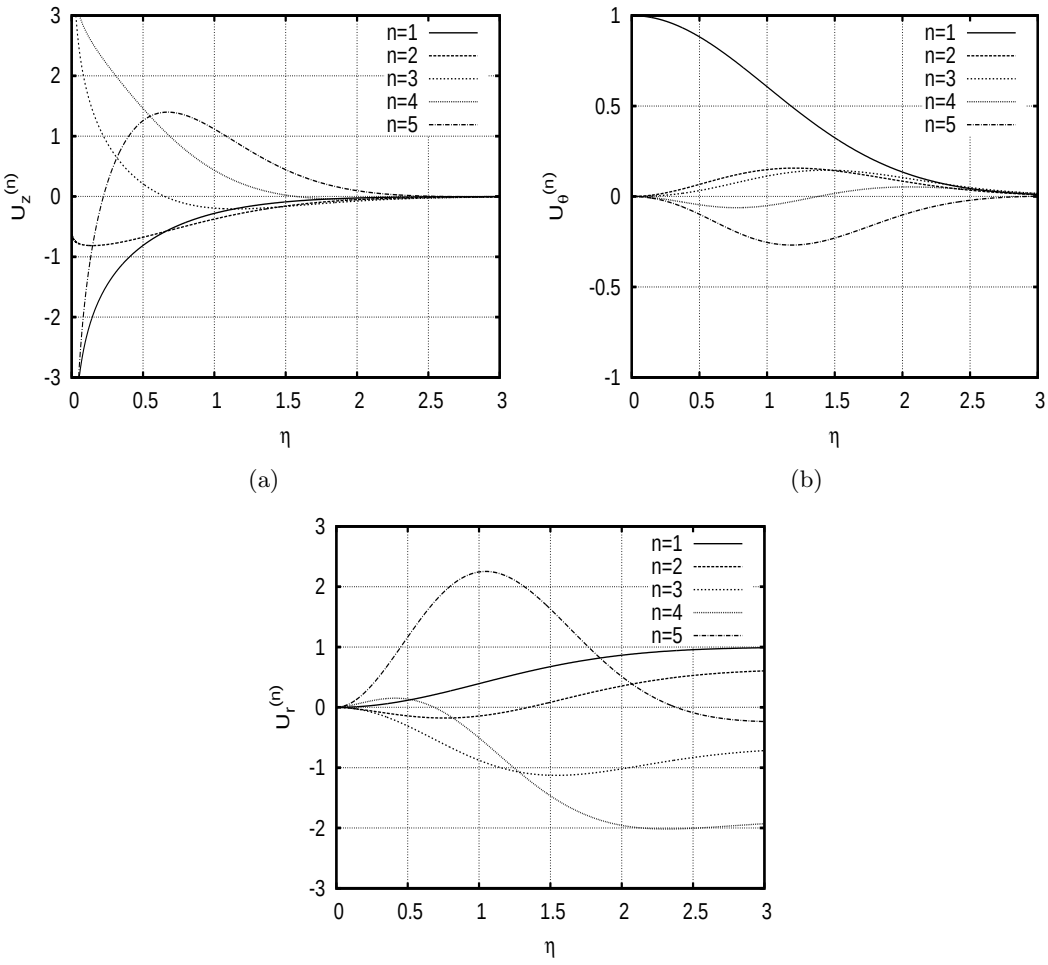

Figure 5.12: First five coefficients of the large Z asymptotic expansion of U_z, U_θ and U_r for $S = 1$.

Appendix B. Flow over the nose

Large Reynolds number implies a thin boundary layer over the nose. Schlichting [1956] gives the axisymmetric boundary-layer equations in terms of curvilinear coordinates, x, y, θ, where x is distance along the surface, and y is distance normal to the surface. Here we use the non-dimensional coordinates, velocity components and pressure:

$$\tilde{y} = \mathrm{Re}^{\frac{1}{2}} y/a, \quad \tilde{x} = x/a, \tag{5.78}$$

$$\tilde{u}_y = \mathrm{Re}^{\frac{1}{2}} u_y/U_\infty, \quad \tilde{u}_x = u_x/U_\infty, \quad \tilde{u}_\theta = u_\theta/U_\infty, \quad \tilde{p} = p. \tag{5.79}$$

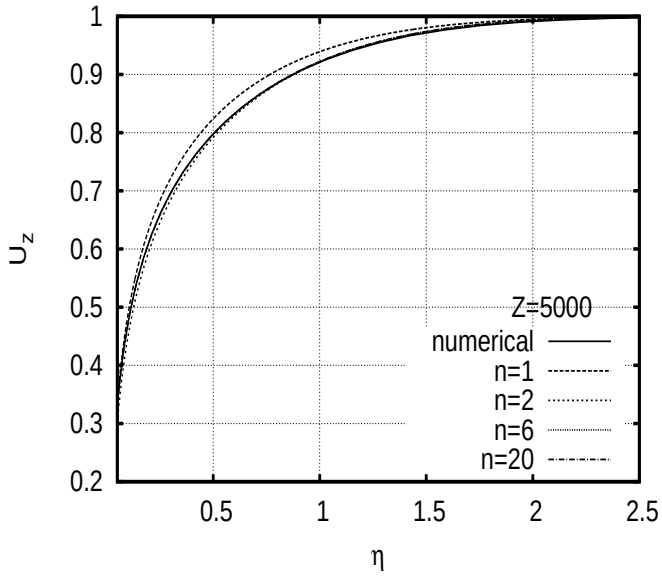

Figure 5.13: Comparison of the numerical solution of U_z with the large-Z asymptotic solution truncated at different orders for $Z = 5000$ at $S = 1$.

The boundary-layer equations in these variables are

$$\tilde{u}_x \frac{\partial \tilde{u}_x}{\partial \tilde{x}} + \tilde{u}_y \frac{\partial \tilde{u}_x}{\partial \tilde{y}} - \frac{\tilde{u}_\theta^2}{\tilde{R}} \frac{\mathrm{d}\tilde{R}}{\mathrm{d}\tilde{x}} = -\frac{\partial \tilde{p}}{\partial \tilde{x}} + \frac{\partial^2 \tilde{u}_x}{\partial \tilde{y}^2}, \tag{5.80}$$

$$\tilde{u}_x \frac{\partial \tilde{u}_\theta}{\partial \tilde{x}} + \tilde{u}_y \frac{\partial \tilde{u}_\theta}{\partial \tilde{y}} + \frac{\tilde{u}_\theta \tilde{u}_x}{\tilde{R}} \frac{\mathrm{d}\tilde{R}}{\mathrm{d}\tilde{x}} = \frac{\partial^2 \tilde{u}_\theta}{\partial \tilde{y}^2}, \tag{5.81}$$

$$\frac{\partial \tilde{p}}{\partial \tilde{y}} = 0,$$

$$\frac{\partial \tilde{u}_x}{\partial \tilde{x}} + \frac{\tilde{u}_x}{\tilde{R}} \frac{d\tilde{R}}{d\tilde{x}} + \frac{\partial \tilde{u}_y}{\partial \tilde{y}} = 0, \tag{5.82}$$

with the boundary conditions

$$\tilde{u}_x = \tilde{u}_y = 0, \tilde{u}_\theta = S\tilde{R}(\tilde{x}) \quad \tilde{y} = 0, \tag{5.83}$$

$$\tilde{u}_x \to U_{ext}(\tilde{x}), \tilde{u}_\theta \to 0 \quad \tilde{y} \to \infty, \tag{5.84}$$

where the nose geometry is represented by $r = \tilde{R}(\tilde{x})$ and $U_{ext}(\tilde{x})$ is the velocity just outside the boundary layer. Equations (5.80)–(5.82) can, in principle, be solved to obtain the flow over the nose. Note the centrifugal term in equation (5.80), which will no doubt produce a wall jet on the nose at sufficiently large S. The terms containing $\mathrm{d}\tilde{R}/\mathrm{d}\tilde{x}$ vanish on the constant-radius cylinder (where $\tilde{x}$ and z coincide to within an additive constant) and equations (5.80)–(5.82) then become those of a flat-plate. Thus, we expect the flow to approach the Blasius solution as $\tilde{x} \to \infty$. There are, in fact, two asymptotic regions, $\tilde{x} = O(1)$ and $\tilde{x} = O(\mathrm{Re})$, the former being described by equations (5.80)–(5.82) and the latter by equations (5.11)–(5.14). Matching of the regions requires the Blasius flow as inlet conditions to the latter equations, as noted in the main text. Thus, the flow in the region $Z = O(1)$, which is the subject of this paper, is insensitive to

the geometry of the nose. Note that a wall jet may appear on the nose, subsequently disappearing on the cylinder, later reappearing in the region $Z = O(1)$.

Chapter 6

Linear stability analysis

This chapter concerns the results of linear stability analysis. The results are presented in the form of an article, published in Physical Review Fluids (Derebail Muralidhar *et al.* [2016a]). As for the previous chapter, the main text and figures are the same as the accepted article, but the sections, figures, etc. have been renumbered. Slight notational changes are also introduced to avoid notational conflicts with earlier chapters.

Instability of flow around a rotating, semi-infinite cylinder

S. Derebail Muralidhar, B. Pier, J. F Scott

Laboratoire de mécanique des fluides et d'acoustique (École centrale de Lyon–CNRS—Université de Lyon 1–INSA Lyon),
36 avenue Guy-de-Collongue, F-69134 Écully, France.

Abstract

Stability of flow around a rotating, semi-infinite cylinder placed in an axial stream is investigated. Assuming large Reynolds number, the basic flow is computed numerically as described by Derebail Muralidhar *et al.* [2016b], while numerical solution of the local stability equations allows calculation of the modal growth rates and hence determination of flow stability or instability. The problem has three nondimensional parameters: the Reynolds number, Re, the rotation rate, S, and the axial location, Z. Small amounts of rotation are found to strongly affect flow stability. This is the result of a nearly neutral mode of the non-rotating cylinder which controls stability at small S. Even small rotation can produce a sufficient perturbation that the mode goes from decaying to growing, with obvious consequences for stability. Without rotation, the flow is stable below a Reynolds number of about 1060 and also beyond a threshold Z. With rotation, no matter how small, instability is no longer constrained by a minimum Re, nor a maximum Z. In particular, the critical Reynolds number goes to zero as $Z \to \infty$, so the flow is always unstable at large enough axial distances from the nose. As Z is increased, the flow goes from stability at small Z to instability at large Z. If the critical Reynolds number is a monotonic decreasing function of Z, as it is for S between about 0.0045 and 5, there is a single boundary in Z, which separates the stable from the unstable part of the flow. On the other hand, when the critical Reynolds number is non-monotonic, there can, depending on the choice of Re, be several such boundaries and flow stability switches more than once as Z is increased. Detailed results showing the critical Reynolds number as a function of Z for different rotation rates are given. We also obtain an asymptotic expansion of the critical Reynolds number at large Z and use perturbation theory to further quantify the behaviour at small S.

6.1 Introduction

The stability of three-dimensional boundary layers provides a rich subject of research (see Reed & Saric [1989], Saric *et al.* [2003] and references therein). Such flows are often due to rotating bodies as, for example, disks (Lingwood [1995]; Pier [2007]), cones (Garrett & Peake [2007], Garrett *et al.* [2010]) or spheres (Pier [2013]). Here we consider a semi-infinite cylinder, rotating about its axis and placed in a high-Reynolds-number axial stream, thus inducing a steady, axisymmetric, three-velocity-component boundary layer whose flow field depends on rotation and curvature of the cylinder, as we have already described in an earlier paper Derebail Muralidhar *et al.* [2016b], henceforth referred to as [I]. In the present paper, we study the stability of this flow for a wide range of parameters, to determine the effects of rotation and curvature.

As noted above, the basic flow around a rotating cylinder in an axial stream (see figure 6.1) has been extensively studied by the authors in preparation for the present stability analysis. To avoid the flow separation typically induced by sharp corners, a smooth nose is assumed at the front of the cylinder. The problem has two nondimensional control parameters: a Reynolds number $\mathrm{Re} = U_\infty a/\nu$, constructed using the incident velocity U_∞ and cylinder radius a, and a rotation

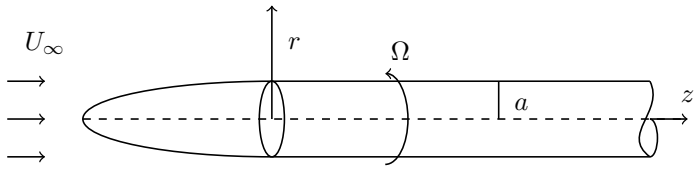

Figure 6.1: Schematic diagram of the problem.

rate $S = \Omega a/U_\infty$, where Ω is the angular velocity of the cylinder. Assuming large Reynolds number, the basic flow comprises an axisymmetric boundary layer. Initially thin compared to the cylinder radius, the boundary-layer thickness increases with axial distance, becoming comparable to the cylinder radius at large axial distances of order $a\mathrm{Re}$. The thickness nonetheless remains small compared with the downstream distance, leading to a separation of length scales (asymptotic in the assumed large Reynolds number) between the axial and radial directions and allowing use of a boundary-layer approximation. However, once the thickness is comparable to a, effects of surface curvature and the centrifugal force due to rotation become important and must be included in the boundary-layer equations. The intervention of curvature and rotation at axial distances of order $a\mathrm{Re}$ is the reason why we focus on this region. Although the basic flow depends on the nose geometry at streamwise distances of order a, boundary-layer development forgets such details and the flow becomes independent of the nose profile at larger distances, in particular those of order $a\mathrm{Re}$. Interested readers should refer to [I] for more details of the basic flow, including the appearance of a wall jet for S above about 4 and asymptotic analyses of the limits of large rotation rate and large streamwise distance.

Stability of the Blasius boundary layer on a flat plate has been extensively studied, the primary instability being due to growth of Tollmien–Schlichting waves (see, for example Tollmien [1928], Jordinson [1970], Mack [1976]). Stability analysis of a non-rotating cylinder placed in an axial stream was conducted by Tutty *et al.* [2002]. They found that nonaxisymmetric modes have a lower critical Reynolds number than axisymmetric modes and that the flow is stable at all streamwise distances for Reynolds numbers below 1060. Above this critical value, the flow is unstable only for a range of streamwise distance and reverts to being stable at sufficiently large distances. Vinod & Govindarajan [2012] studied the secondary instability and also showed that the flow is stable according to inviscid theory.

There have been few studies of the stability of a rotating cylinder placed in an axial stream. Kao & Chow [1991] appear to be the first to consider the rotating case, but their basic flow is erroneous because they do not include the centrifugal term in the radial momentum equation. They also studied the non-rotating case, but the results are in disagreement with Tutty *et al.* [2002]. This disagreement was noted by Herrada *et al.* [2008], who were the first to formulate the correct basic-flow equations. Results were obtained for a range of rotation rates between 0.1 and 1, and are in excellent agreement with our results. They observed that the critical Reynolds numbers were much lower than for the non-rotating case. This motivated us to study the rotating case in a more systematic manner, in particular the range of small rotation rates. To our surprise, we found that the stability characteristics, in particular the critical curves, were significantly dependent on the rotation rate for values of S much lower than the ones covered in Herrada *et al.* [2008]. The elucidation of these differences between the non-rotating case and the rotating case at very low S is one of the main topics of this paper.

To our knowledge, the only published experimental work on a rotating cylinder which matches the geometry of the present study is by Kegelman *et al.* [1983]. They give visualizations of different instability modes developing on the cylinder. However, the cylindrical section in their

experiments is not long enough to reach distances at which the flow forgets the details of the nose profile (let alone to reach distances at which curvature and rotation become important for the basic flow). Thus, quantitative comparison between our results and Kegelman *et al.* [1983] is inappropriate and is not attempted.

Formally, the basic flow and stability equations for the rotating cylinder are the same as those of a vortex core with axial flow (in the quasi-cylindrical approximation, see Hall [1972]). However, the two flows are quite different and it would be rash to draw parallels in terms of stability. In particular, vortex breakdown is associated with an adverse axial pressure gradient of the basic flow, whereas the rotating cylinder has a favourable pressure gradient.

The local stability equations are derived in section 6.2. The numerical scheme is described in section 6.3, along with results of validation. Section 6.4 contains the main results. In section 6.4.3, the limit of low rotation rate is examined in more detail and quantified using a perturbation method.

6.2 Problem formulation

A semi-infinite cylinder of radius a, which rotates about its axis at angular velocity Ω, is placed in an axial stream of velocity U_∞ (see Figure 6.1), the fluid being incompressible and of viscosity ν and density ρ. Lengths, times, velocities and pressures are nondimensionalized using a, a/U_∞, U_∞ and ρU_∞^2. Adopting cylindrical coordinates (z, r, θ), the basic (steady and axisymmetric) flow has velocity components U_z, U_r, U_θ and associated pressure denoted by P. As noted in the introduction, there are two control parameters, namely the Reynolds number Re and the rotation rate S, given by

$$\mathrm{Re} = \frac{U_\infty a}{\nu}, \tag{6.1}$$

$$S = \frac{\Omega a}{U_\infty}. \tag{6.2}$$

To avoid possible confusion, we remark that U_z, U_r, U_θ and P were denoted by u_z, u_r, u_θ and p in [I], whereas these lower-case quantities are used to represent the flow perturbation in the present paper.

We assume large Reynolds number from here on and restrict attention to the flow over the constant-radius part of the cylinder, $z > 0$. As discussed in the introduction, large Reynolds number leads to a separation of length scales in which streamwise evolution of the basic flow is slow compared with its radial variation. Not only does this allow use of the boundary-layer approximation to describe the basic flow, but it is also a prerequisite for local stability analysis. Boundary-layer theory implies that U_r is small compared with U_z and U_θ. Neglect of U_r is the second ingredient of local stability theory.

Under these assumptions, the steady and axisymmetric base-flow components are governed by a generalization of the classical Prandtl boundary-layer equations that allow for the additional effects of both curvature and rotation. Near the nose, the boundary layer is thin compared with the cylinder radius. Thus, in that region, curvature effects are negligible and the flow is close to the Blasius profile of a flat plate. Using a Blasius inlet condition, the entire base flow is then obtained by integrating the boundary-layer equations along the z-direction. See [I] for full theoretical and numerical details about the basic flow.

The linear stability equations are obtained in the usual manner: by adding infinitesimal perturbations (u_z, u_r, u_θ, p) to the basic flow quantities (U_z, U_r, U_θ, P), using the non-dimensionalized Navier–Stokes equations and neglecting terms which are non-linear in the perturbations. The

local approximation is then adopted: U_r is neglected, as are variations of U_z and U_θ with respect to z. Invariance with respect to z, θ and t allows modal solutions of the form

$$\begin{pmatrix} u_z \\ u_r \\ u_\theta \\ p \end{pmatrix} = \begin{pmatrix} v_z(r) \\ v_r(r) \\ v_\theta(r) \\ q(r) \end{pmatrix} \mathrm{e}^{\mathrm{i}(\alpha z + m\theta - \omega t)}. \tag{6.3}$$

Here, ω is the complex frequency, while α and m are the axial and azimuthal wavenumbers, which are respectively real and integer modal parameters. Note that modes occur in complex-conjugate pairs, related by $\alpha \leftrightarrow -\alpha$, $m \leftrightarrow -m$ and $\omega \leftrightarrow -\omega^*$, where $*$ denotes complex conjugation. It is this conjugation symmetry which allows the construction of physically meaningful (i.e. real) solutions by combining a mode and its conjugate. Conjugation symmetry allows us to restrict attention to $\alpha \geq 0$, while m can take any integer value.

Substituting the modal form for the perturbation in the local stability equations gives

$$\mathrm{i}\alpha v_z + v_r' + \frac{1}{r}v_r + \frac{\mathrm{i}m}{r}v_\theta = 0, \tag{6.4}$$

$$\mathrm{i}\left(\alpha U_z + \frac{mU_\theta}{r} - \omega\right)v_z + U_z' v_r + \mathrm{i}\alpha q = \frac{1}{\mathrm{Re}}\left[v_z'' + \frac{1}{r}v_z' - \left(\alpha^2 + \frac{m^2}{r^2}\right)v_z\right], \tag{6.5}$$

$$\mathrm{i}\left(\alpha U_z + \frac{mU_\theta}{r} - \omega\right)v_r - \frac{2U_\theta}{r}v_\theta + q' = \frac{1}{\mathrm{Re}}\left[v_r'' + \frac{1}{r}v_r' - \left(\alpha^2 + \frac{m^2+1}{r^2}\right)v_r - \frac{2\mathrm{i}m}{r^2}v_\theta\right], \tag{6.6}$$

$$\mathrm{i}\left(\alpha U_z + \frac{mU_\theta}{r} - \omega\right)v_\theta + \left(U_\theta' + \frac{U_\theta}{r}\right)v_r + \frac{\mathrm{i}m}{r}q = \frac{1}{\mathrm{Re}}\left[v_\theta'' + \frac{1}{r}v_\theta' - \left(\alpha^2 + \frac{m^2+1}{r^2}\right)v_\theta + \frac{2\mathrm{i}m}{r^2}v_r\right], \tag{6.7}$$

where the primes denote derivatives with respect to r. The boundary conditions are

$$v_z(1) = v_r(1) = v_\theta(1) = 0, \tag{6.8}$$

$$v_z(\infty) = v_r(\infty) = v_\theta(\infty) = 0. \tag{6.9}$$

The modes are determined as nonzero solutions of the above boundary-value problem. The problem contains the basic-flow velocity profiles $U_z(r)$ and $U_\theta(r)$, which are determined by solving the boundary-layer equations, as described in [I]. As noted in the introduction, the basic flow becomes independent of the nose geometry for streamwise distances much greater than a, i.e. large z, and we focus on this region. As shown in [I], $U_z(r)$ and $U_\theta(r)$ then depend only on the parameters $Z = z\mathrm{Re}$ and S, of which the former is a version of streamwise distance, scaled such that the boundary-layer thickness is of order a when Z is of order 1. Thus, the physical parameters of the problem are Re, Z and S, while it also contains the modal parameters α and m. The set of differential equations and boundary conditions given above form an eigenvalue problem for determination of possible values of the complex frequency $\omega = \omega_r + \mathrm{i}\omega_i$, whose imaginary part gives the modal growth rate. Expressing the eigenvalues in terms of the other parameters of the problem yields the dispersion relation

$$\omega = F(\alpha, m, \mathrm{Re}, Z, S). \tag{6.10}$$

Numerical solution of the eigenvalue problem is described in the next section. The physical parameters, Re, Z and S, and modal parameters, α and m, are then varied, looking for growing modes, i.e. eigenvalues with $\omega_i > 0$, which are symptomatic of local instability.

6.3 Numerical Method

Prior to numerical discretization, we transform the radial coordinate as in [I]. Because the boundary-layer thickness goes to zero like $Z^{1/2}$ at small Z, the radial coordinate is first replaced by $\sigma = (r-1)/(2Z)^{1/2}$ to improve the radial resolution in that limit. The semi-infinite range of σ is then transformed to a finite interval using

$$x = \frac{\sigma - \hat{\sigma}}{\sigma + \hat{\sigma}} \quad \sigma \in [0, \infty] \rightarrow x \in [-1, 1], \tag{6.11}$$

where $\hat{\sigma} > 0$ is a numerical parameter allowing some control over the distribution of the discrete points introduced below.

Also as in [I], rewriting the local stability equations using the coordinate x, Chebyshev collocation is used to discretize the problem. We introduce the N collocation points

$$x_n = \cos\left(\frac{n\pi}{N-1}\right) \quad 0 \leq n < N, \tag{6.12}$$

where, to avoid interpolation, N has the same value as in the calculation of the basic flow. Note that, according to (6.11), $\hat{\sigma}$ divides the flow into two ranges, $\sigma < \hat{\sigma}$ and $\sigma > \hat{\sigma}$, containing equal numbers of points. The smaller $\hat{\sigma}$, the better the resolution near the cylinder and the worse the resolution at large σ, the opposite being true if $\hat{\sigma}$ is increased. The variables v_z, v_r and v_θ are represented by their values at all collocation points, whereas only the values of q for $0 < n < N-1$ are used. As is usual in Chebyshev collocation, derivatives are expressed using polynomial fitting: $(N-1)$th degree polynomials are fitted to the discrete values of v_z, v_r and v_θ and an $(N-3)$th one to those of q. This allows approximation of derivatives as matrices obtained by differentiating the polynomials. Equations (6.4)–(6.7) are applied at x_n for $0 < n < N-1$, giving $4N-8$ equations for the $4N-2$ discrete values of v_z, v_r, v_θ and q. q is eliminated as described in appendix C1 of Leclercq [2013], as are the boundary values of v_z, v_r and v_θ using (6.8) and (6.9). The result is a $(3N-6) \times (3N-6)$ standard matrix eigenvalue problem with eigenvalue ω and eigenvector whose elements are the discrete values of v_z, v_r and v_θ at $x = x_n$ for $0 < n < N-1$.

Figure 6.2a shows an example of a numerically computed eigenspectrum in the complex phase velocity ($c = c_r + \mathrm{i}c_i$) plane (where $c = \omega/\alpha$). It consists of a discretized version of the continuous spectrum (which arises because the flow domain is semi-infinite in the radial direction) and a set of discrete eigenvalues, one of which has $c_i > 0$ and therefore represents a growing mode. We conclude that the flow is unstable for the given values of Re, Z and S. The continuous spectrum can be safely neglected as it always lies in $c_i \leq 0$, originating at $c = 1 - \mathrm{i}\alpha/\mathrm{Re}$ and extending downwards in the complex c-plane (see the asymptotic analysis in Schmid & Henningson [2001]).

The code was tested by observing the sensitivity of the most unstable (largest c_i) discrete eigenvalue (which is the one of principal interest) to changes in the numerical parameters N, $\hat{\sigma}$ and Δ, where Δ is the axial step used in the basic-flow computation (recall from [I] that the basic flow was obtained by integration of the boundary-layer equations using small steps, Δ, in $\zeta = (2Z)^{1/2}$). Figure 6.2b shows a log-log plot of the relative error, ϵ, of the computed eigenvalue with $\hat{\sigma} = 5$ and the parameters given in figure 6.2b as a function of Δ for different values of N. The error is computed by comparison with the case $N = 128$ and $\Delta = 0.0001$. It will be seen that, for $N = 64$ and 128, the accuracy is mainly limited by axial dicretization. The results are consistent with the use of a scheme which is second-order accurate in Δ to compute the basic flow, as can be seen by comparison with the reference line on the plot. The mapping parameter, $\hat{\sigma}$, was found to affect the precision at only the tenth decimal place when varied between $2-6$. After studying such convergence results for numerous sets of parameters, we decided to use

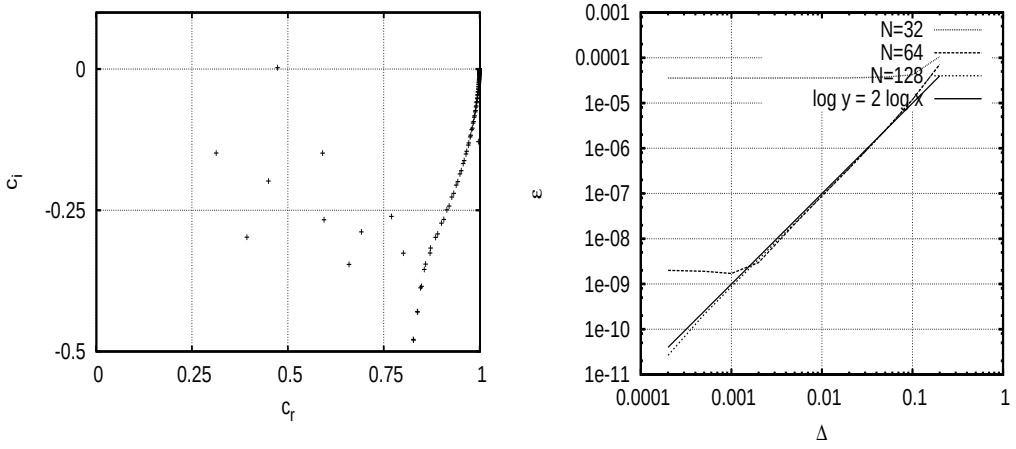

(a) (b)

Figure 6.2: a) Eigenspectrum in the complex c-plane for Re = 2000, $\alpha = 0.2$, $Z = 0.5$, $m = 1$ and $S = 0.01$. b) Relative error plot as a function of the axial discretization of the basic flow for different values of N.

$N = 64, \hat{\sigma} = 5$ and $\Delta = 0.001$ for the computations. This gives better than 8 decimal places of accuracy. Note that, even though the continuous spectrum is not well resolved, this does not significantly affect the accuracy with which the most unstable eigenvalue is computed. The numerical eigenfunctions were also validated by comparing their exponential decay rate at large radial distances with the asymptotic decay rate given by the streamwise wavenumber α (see Schmid & Henningson [2001]). Good agreement was found.

For given m and S, the neutral curve is defined as the boundary of the region in the $\mathrm{Re} - Z$ plane for which a growing mode exists. Another way of putting this is that it is the curve of zero maximum growth rate, with the maximum taken over the discrete spectrum and all α. A first approximation to the neutral curves was obtained by plotting the contour of zero maximum growth rate in the $\mathrm{Re} - Z$ plane using a rectangular grid of values. This was carried out for different values of m and S. However, obtaining accurate neutral curves with such a method requires a very fine grid, making it computationally expensive. A faster, multi-variate Newton-Raphson scheme was developed to obtain more precise results with values taken from the contour plot to initialize the iteration. The neutral point, α, Re, at a given m, Z, S is obtained by simultaneously solving the system of equations

$$\omega_i(\alpha, \mathrm{Re}) = 0, \tag{6.13}$$

$$\frac{\partial \omega_i}{\partial \alpha}(\alpha, \mathrm{Re}) = 0. \tag{6.14}$$

The Newton-Raphson scheme requires computation of derivatives of ω_i with respect to α and Re, which were obtained using centred finite differencing. The solution was considered to have converged when the norm of the residuals was less than 10^{-7}. The result was used to initialize the iteration at the next step in Z, and the process continued for a range of values of Z.

The code was validated by comparing the results for the neutral curve with $S = 0.1$ and $m = 1$ with those of Herrada *et al.* [2008]. Figure 6.3 shows good agreement. Since the results of Herrada *et al.* [2008] for the non-rotating case are known to be in agreement with those of Tutty

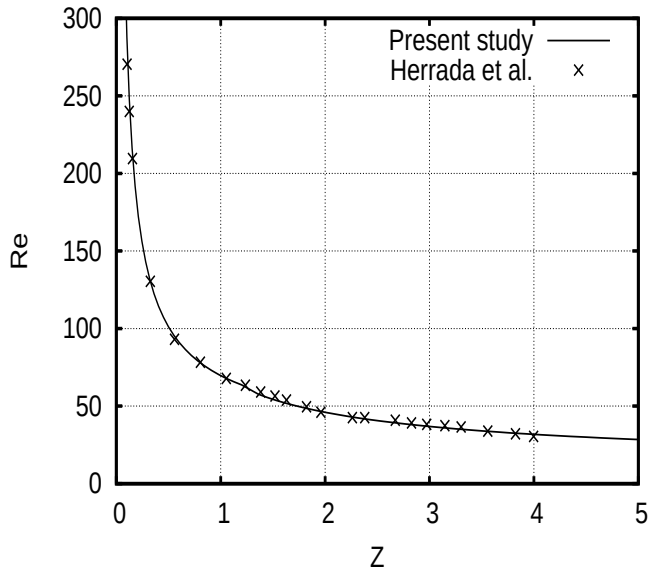

Figure 6.3: Comparison of the neutral curve for $m = 1$, $S = 0.1$ with results of Herrada *et al.* [2008].

et al. [2002], a comparison of our results with Tutty *et al.* [2002] will not be presented, though we did check they agreed.

6.4 Results

6.4.1 Eigenspectra and growth-rate plots

The eigenspectra for the non-rotating case are qualitatively similar to that of the Blasius boundary layer, there being one distinguished eigenvalue close to the real axis in the complex c-plane. This eigenvalue may lie in either $c_i > 0$ or $c_i \leq 0$, the remainder of the discrete spectrum being in $c_i < 0$ and well separated from the real c-axis. Similarity with the Blasius flow might be expected because the basic flow without rotation has a velocity profile, $U_z(r)$, whose form resembles the Blasius profile, which it approaches in the limit $Z \to 0$. It is the sign of c_i for the distinguished mode which controls flow stability in the non-rotating case, hence also for sufficiently small values of S.

Figure 6.2a shows an example with small rotation rate ($S = 0.01$): the eigenspectrum is essentially the same as for the non-rotating case at the same values of Re, α, Z and m. However, because it is close to the real c-axis, the slight perturbation of the distinguished mode at small S may suffice for c_i to change sign, with obvious consequences for flow stability. This does, in fact, happen for the values of Re, α, Z and m used in figure 6.2a: $c_i < 0$ when $S = 0$ and $c_i > 0$ when $S = 0.01$. This is a reflection of a surprising sensitivity of flow stability to small amounts of rotation, an important theme of this paper which will be further elucidated by later results.

As S is increased to larger values, the eigenspectrum changes character and one can no longer think in terms of a single distinguished mode near the real c-axis which controls stability. Figure 6.4a shows an example in which two discrete modes are unstable. Thus, for the rotating case, there can be more than one growing mode. When this occurs, the mode with the largest c_i

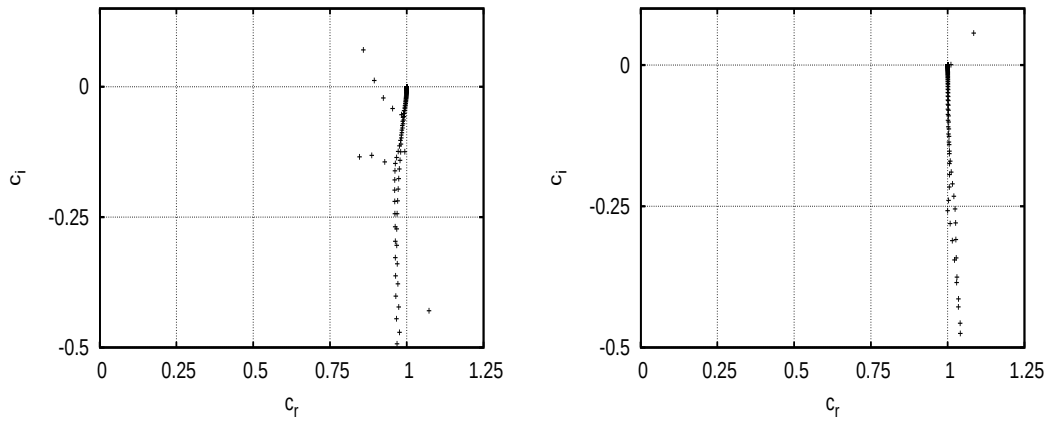

(a) (b)

Figure 6.4: Eigenspectra for: a) Re = 200, $\alpha = 0.16$, $Z = 12.5$, $m = 3$ and $S = 0.2$, b) Re = 200, $\alpha = 0.04$, $Z = 12.5$, $m = 1$ and $S = 0.5$.

is more important because it grows fastest according to the linear theory used here. Figure 6.4b gives an example in which there is a growing mode with $c_r > 1$, despite the fact that the maximum value of $U_z(r)$ is 1. Howard & Gupta [1962] have shown that a modified semi-circle theorem (which places limits on c_r) can be obtained for general swirling flows, but only for axisymmetric disturbances ($m = 0$) in the inviscid case. We are unaware of any such result for non-axisymmetric disturbances. The given example shows that the phase velocity of a mode can exceed the maximum of $U_z(r)$ when $S > 0$.

From here on, we focus on the fastest growing discrete mode. Overall instability/stability of the flow is determined by the sign of the maximum growth rate, $\omega_i^{\max}$, the maximum being taken over all m and α. However, before taking this step, it is perhaps interesting to consider the behaviour of the growth rate, ω_i, as a function of m and α. We never found a case in which $\omega_i^{\max} > 0$ arose from $m \leq 0$ modes, so we mostly restrict attention to $m > 0$ in what follows.

Figure 6.5a shows an example for which ω_i is plotted as a function of α for different values of m. We see that the m which yields the largest ω_i depends on α and that the overall maximum, $\omega_i^{\max}$, arises from $m = 1$ (it is given by the peak in the $m = 1$ curve). This is not always the case, as is apparent from figure 6.5b, for which $\omega_i^{\max}$ arises from $m = 2$. In the absence of rotation, we found that $\omega_i^{\max}$ was always associated with either $m = 1$ or $m = 2$ when the flow was unstable, in agreement with the results of Tutty *et al.* [2002] for the particular case Re = 15000. However, higher values of m can arise for nonzero S and we found no general rule concerning the m associated with $\omega_i^{\max}$ in the presence of rotation. We remark that, for the quite different case of flow in a rotating pipe, Pedley [1969] also found that the m yielding the maximum overall growth rate depends on the physical parameters of the flow.

Negative values of m were also examined. In the nonrotating case, reflection symmetry with respect to any plane containing the cylinder axis implies that the growth rates for m are the same as for $-m$. For nonzero S, we found that negative m yields lower growth rates than positive m, as illustrated by Figure 6.5c. Attention is restricted to $m > 0$ from here on.

Figure 6.5d shows cases for which $\omega_i(\alpha)$ has more than one local maximum. As the physical parameters are varied, the overall maximum can jump discontinuously from one local maximum to another, a phenomenon encountered later. The effect of such a jump is apparent in figure 6c

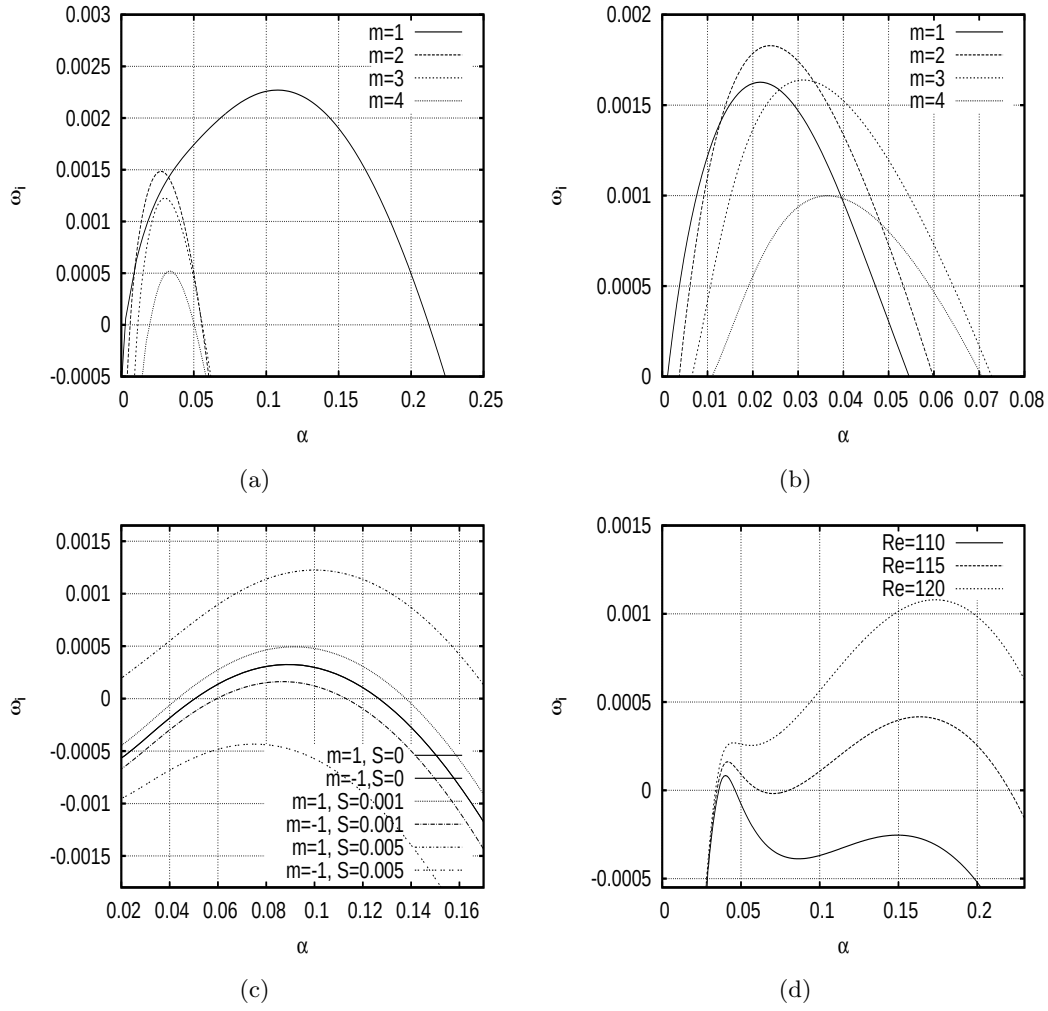

Figure 6.5: Plots of temporal growth rate as a function of α: a) Re $= 2000, Z = 0.5$ and $S = 0.01$, b) Re $= 2000, Z = 2$ and $S = 0.01$, c) Re $= 2000, Z = 0.5$ for $m = 1$ and $m = -1$ and different (small) values of S, d) $Z = 0.5$, $S = 0.1, m = 1$ for different values of Re.

of Herrada *et al.* [2008] and in results of the next subsection.

6.4.2 Overall maximum growth rate, neutral and critical curves

Contour plots of overall maximum growth rate, $\omega_i^{\max}$, in the $\mathrm{Re} - Z$ plane are shown for three values of S in figure 6.6. The contours $\omega_i^{\max} = 0$ are the critical curves, which form the boundary between flow stability and instability. (Note that we use the term neutral curve for the stability boundary of a single value of m, while a critical curve allows for all m.) Figure 6.6a shows that the non-rotating flow is always stable above a certain value of Z (0.8001), i.e. at sufficiently large downstream distances, and also below a certain value of Re (1059.5, in accord with Tutty *et al.* [2002]). The other two cases are quite different: instability has neither an upper limit in Z nor a lower limit in Re. Note the small growth rates in the unstable region for all three cases. This reflects control of small-S stability by a distinguished mode close to the real c-axis, as does figure 6.7. Note also the large differences between the contour plots, a result which is perhaps at first surprising, but is, in fact, a logical consequence of a controlling mode close to the real c-axis for $S = 0$.

As noted towards the end of section 6.3, obtaining accurate neutral curves using contour plots is computationally expensive compared to Newton–Raphson iteration and varying Z in small steps, and the same is even more true for critical curves because different m must be accounted for. For this reason, we use Newton–Raphson iteration (as described in section 6.3) to follow the neutral curves, then combine the results for different m to obtain the critical curve. This is achieved by minimisation of the neutral Reynolds number over m for given Z and S.

Figure 6.8a shows neutral curves for the first three non-axisymmetric modes and $S = 0.1$. The critical Reynolds number arises from the $m = 1$ mode for $Z > 1.3$ and from $m = 2$ for Z between $0.05 - 1.3$. Higher m take over for Z less than about 0.05. These do not contribute to the plots of figure 6.8a because the critical Reynolds number lies above the range shown. As noted earlier, $m = 1$ and $m = 2$ control stability in the non-rotating case and here we see that they are the most important modes for small S as well. Indeed, we found that, when $Z > 0.1$, criticality was associated with $m = 1$ or $m = 2$ in all cases studied.

Figure 6.8b shows plots of the axial wavenumber corresponding to neutrality. The jumps are a consequence of the existence of two local maxima in $\omega_i(\alpha)$, a scenario discussed earlier and illustrated by figure 6.5d. As Z is varied, neutrality is controlled first by one of the maxima, then by the other. At the jump, both maxima give $\omega_i = 0$.

Figure 6.9 shows critical curves and corresponding wavenumber plots for values of S between $0 - 0.012$. The sensitivity of flow stability to small amounts of rotation is again apparent. As noted earlier, when $S = 0$ there is a minimal Reynolds number and a maximal Z for instability, neither of which persist to the rotating case. A given value of the Reynolds number corresponds to a horizontal line in figure 6.9a, whose intersections with the critical curve yield boundaries in Z separating regions of stability and instability. With or without rotation, the flow is stable at sufficiently small Z, but each time the critical curve is crossed, the flow changes stability. In the non-rotating case, stability at small Z can either persist to all Z (if $\mathrm{Re} \leq 1059.5$) or there is a range of instability, beyond which the flow is again stable. The rotating case is quite different because the critical Reynolds number decreases to zero at large Z. As a result, the flow is unstable for sufficiently large Z. If the critical Reynolds number is a monotonically decreasing function of Z, as it is for small S above a certain threshold value equal to about 0.0045, there is a single intersection of the critical curve with any given line of constant Re, resulting in stability at small Z, followed by instability once the critical curve is crossed. On the other hand, the critical curve is non-monotonic for S below the threshold, as illustrated by figure 6.9a for three such values of $S > 0$. For values of Re between the local minimum and maximum of the curve, there are then

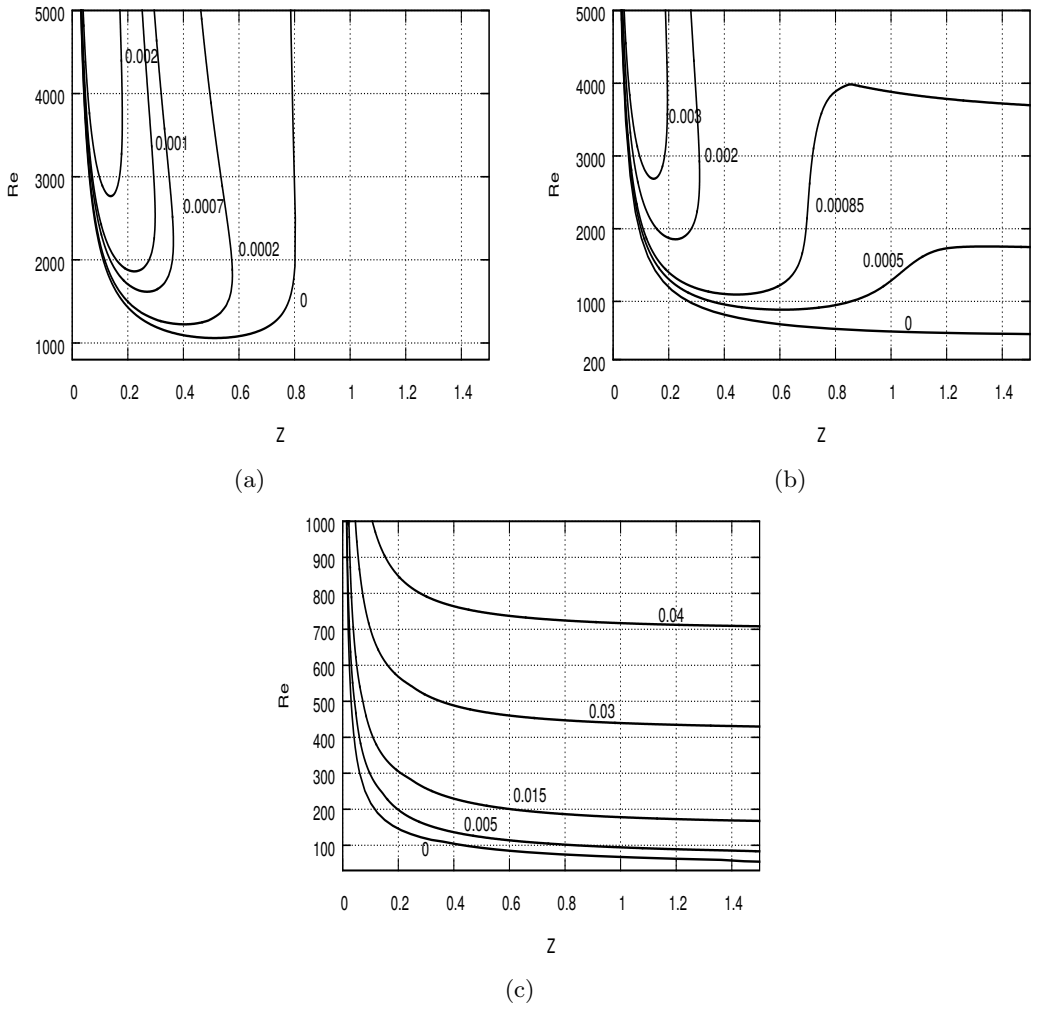

Figure 6.6: Contour plots of $\omega_i^{\max}$ for a) $S = 0$, b) $S = 0.005$ and c) $S = 0.1$.

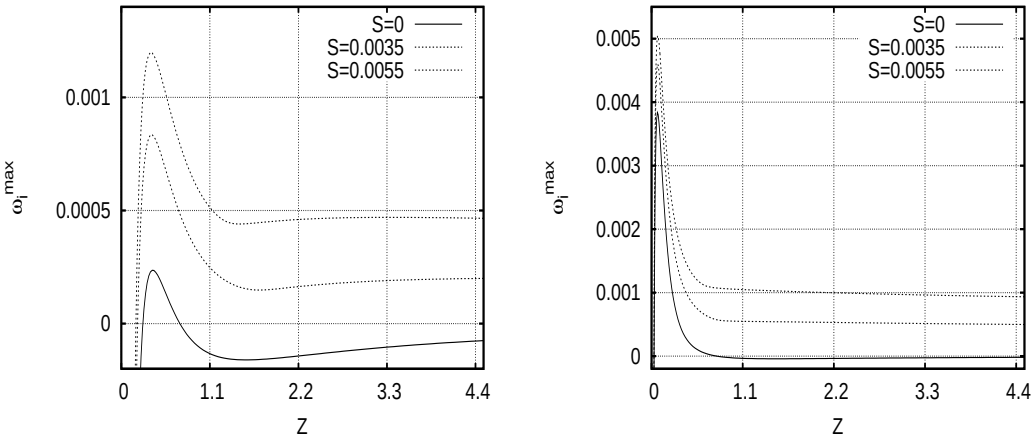

(a) (b)

Figure 6.7: Plots of $\omega_i^{\max}$ as a function of Z for different (small) values of S and: a) $\mathrm{Re} = 1250$, b) $\mathrm{Re} = 5000$.

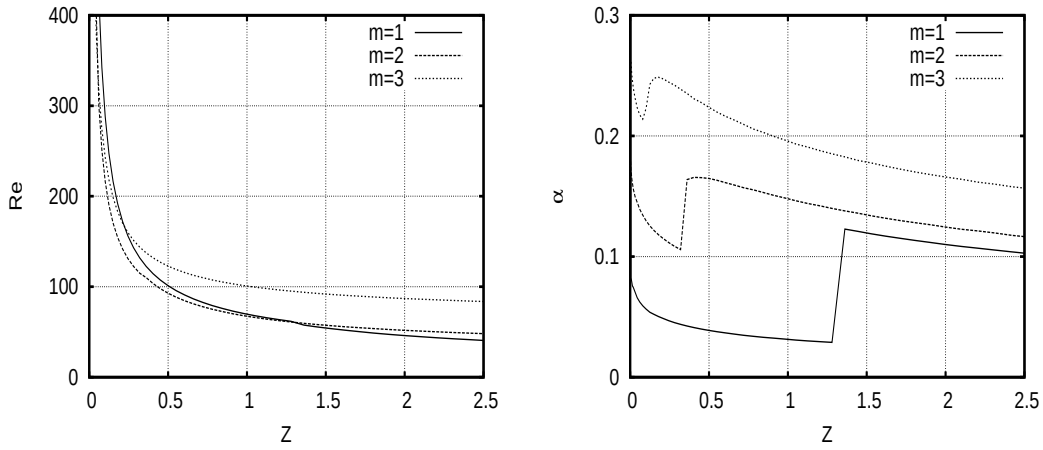

(a) (b)

Figure 6.8: a) Neutral curves and b) corresponding wavenumber plots for $m = 1, 2$ and 3 and $S = 0.1$.

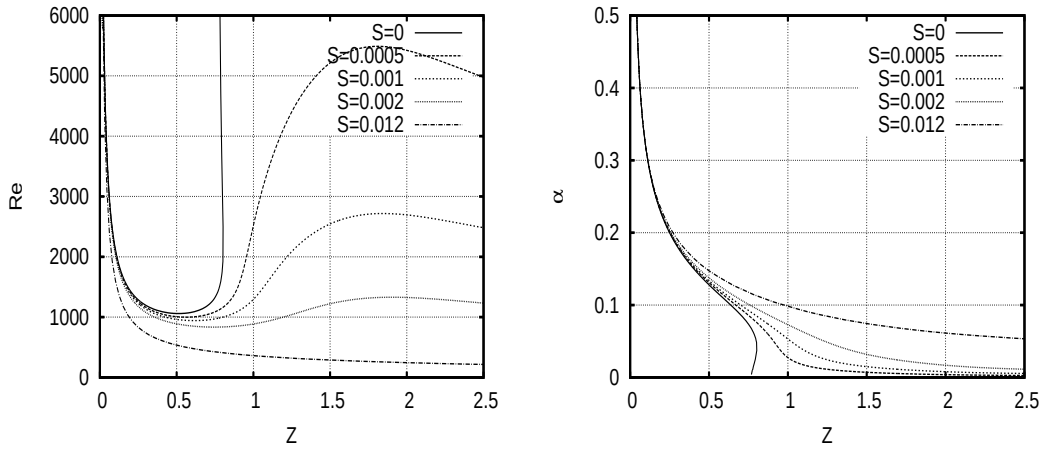

(a) (b)

Figure 6.9: a) Critical curves and b) corresponding wavenumber plots for values of S between 0 and 0.012.

three stability boundaries, hence four distinct regions in Z: stable/unstable/stable/unstable as Z increases. Note that increasing S lowers the critical Reynolds number, i.e. rotation has a destabilising effect.

Figure 6.10 concerns S between 0.1 and 1. According to figure 6.10a, the critical Reynolds number remains a decreasing function of Z and S, while figure 6.10b shows jumps in the critical wavenumber. Some of these jumps were identified as between local maxima of $\omega_i(\alpha)$ for a single m, while others correspond to jumps between different m.

Figure 6.11 gives results for higher values of S. Close inspection of figure 6.11a reveals that the critical Re is no longer a monotonic decreasing function of Z for $S = 10$ and $S = 15$. This is more apparent in figure 6.12, which extends the range of Z to much higher values using a logarithmic scale. For S exceeding a threshold value of about 5, the critical curve is non-monotonic, as it is for S below the small-S threshold of about 0.0045. This leads to the same qualitative conclusion concerning stability, namely the possibility, depending on Re, of more than one stability/instability boundary in Z. Note the sharp cusp in the critical curve for $S = 6$, apparent in figure 6.12, which is a consequence of a jump between different local maxima of $\omega_i(\alpha)$ for $m = 1$.

Figure 6.11a shows that the critical Re continues to be a decreasing function of S for fixed Z less than about 3. However, as is apparent from figure 6.12, this is no longer the case at larger Z when S exceeds a certain threshold value (which we found to be about 2.5). At such values of S, no general statement, covering all values of Z, concerning the effects of increasing rotation on flow stability can be made.

Figure 6.13a shows critical curves for $5 < Z < 100000$ and illustrates the statement, made earlier, that the critical Reynolds number tends to 0 as $Z \to \infty$. Figure 6.13b shows the same results, but it is $Z^{1/2}$Re, rather than Re, which is plotted as a function of Z. It appears that the curves asymptote to straight lines at large Z, corresponding to the asymptotic expansion $\mathrm{Re} \sim Z^{-1/2}(A \ln Z + B)$ for the critical Reynolds number as $Z \to \infty$. It is interesting to note that the coefficient A (corresponding to the slope of the asymptote in the figure) appears to have the same value (close to 18) for different S. On the other hand, B is a decreasing function of S, so increasing rotation destabilizes the flow at large Z, as it does at small Z. Although asymptotic

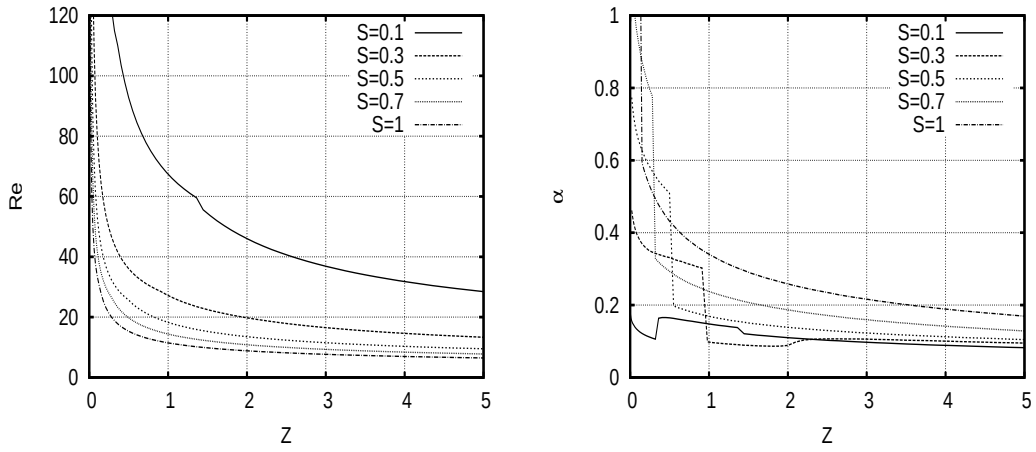

(a) (b)

Figure 6.10: a) Critical curves and b) corresponding wavenumber plots for values of S between 0.1 and 1.

analysis of the large-Z limit of the stability problem has not been attempted, the form of the expansion given above is a logical consequence of that of the asymptotic expansions of the basic flow velocity profiles, which were derived in [I] (section 5a and appendix A). These expansions proceed in inverse powers of $\ln Z$, hence the appearance of $\ln Z$ in the expansion of the critical Reynolds number. The coefficients of the basic-flow expansions are functions of $r/Z^{1/2}$, leading to the factor of $Z^{-1/2}$.

Finally, some caveats concerning the results at large S. Figure 6.11a shows that the critical Reynolds number is rather low (of order 5) except at small Z. Such moderate values of Re raise questions concerning the basis of the present work: both the boundary-layer equations used to compute the basic flow and the local stability equations for the perturbation are predicated on the assumption of large Re. Thus, accurate quantitative values of the critical Reynolds number should not be expected at large S. We might, nonetheless, hope that qualitative trends resemble the present results.

6.4.3 Small-S perturbation analysis

As we have seen (recall figures 6.6 and 6.9), flow stability is significantly affected by small amounts of rotation. This suggests using the Taylor's series

$$\omega_i = \omega_{i0} + \frac{\partial \omega_i}{\partial S} S + \frac{1}{2} \frac{\partial^2 \omega_i}{\partial S^2} S^2 + ... \tag{6.15}$$

to express the effects of rotation. Here, ω_{i0} and the derivatives of ω_i denote $S = 0$ values for given m, Z, Re and α. As discussed earlier, small-S stability is controlled by a single distinguished mode, having small ω_{i0} and to which we specialize in this subsection (as noted earlier, other discrete eigenvalues are well below the real ω-axis and hence unimportant).

Figure 6.14 shows a plot of $\omega_i(S)$ for particular values of m, Z, Re and α. The full numerical results are compared with the Taylor's series truncated at different orders (the derivatives in (6.15) being determined using second-order, centred finite differencing). Second- and higher-order terms can be neglected to a first approximation. Note the small value of ω_{i0}, here negative,

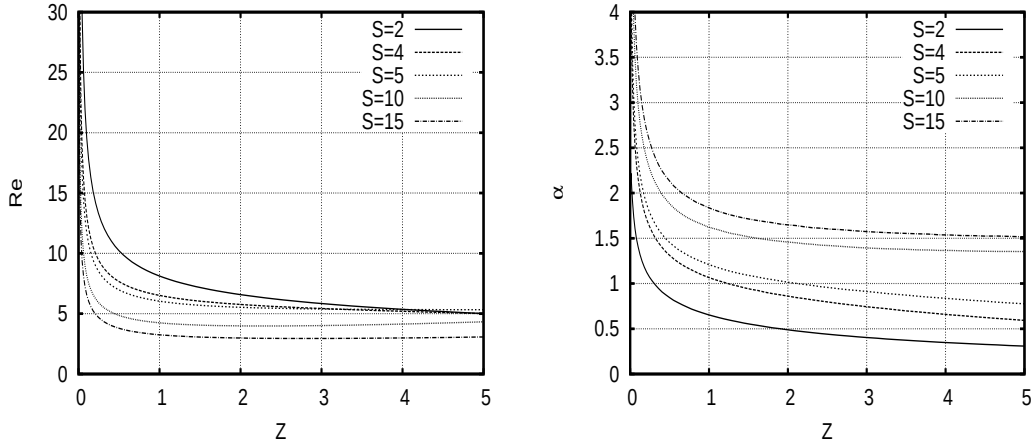

(a) (b)

Figure 6.11: a) Critical curves and b) corresponding wavenumber plots for values of S between 2 and 15.

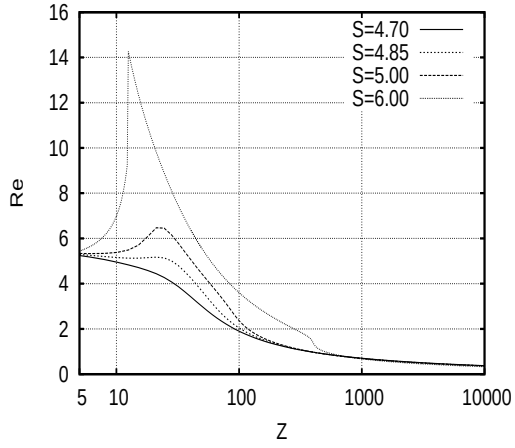

Figure 6.12: Critical curves for $5 < Z < 10000$.

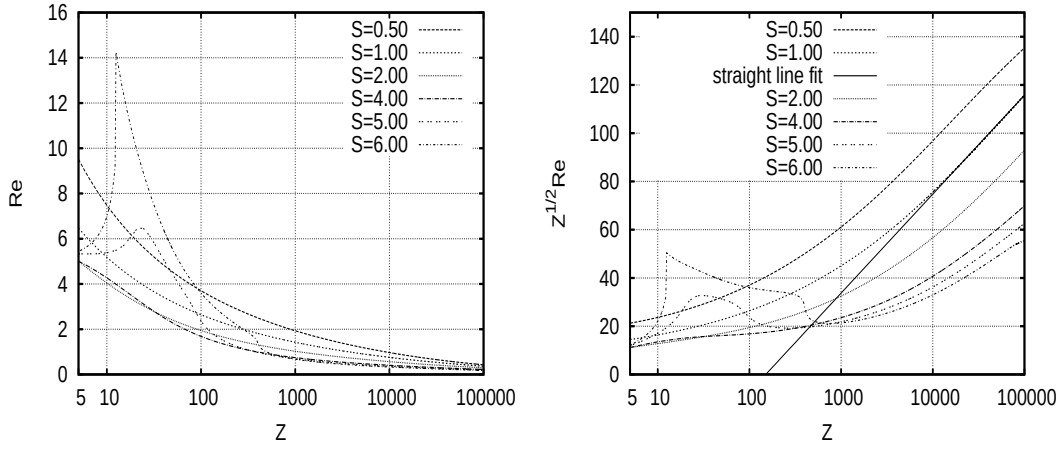

(a) (b)

Figure 6.13: Critical curves for $5 < Z < 100000$: a) Re, b) $Z^{1/2}\mathrm{Re}$ as functions of Z.

which is characteristic of the distinguished mode, and the order 1 value of $\partial\omega_i/\partial S$. It is the combination of these two ingredients which makes flow stability sensitive to small amounts of rotation. As noted earlier, increasing small S destabilizes the flow, a result which is a consequence of positive $\partial\omega_i/\partial S$ for the distinguished mode when $S = 0$.

6.5 Conclusion

In this paper, we have studied the local, linear stability of flow around a semi-infinite, rotating cylinder placed in an axial stream. Assuming large values of the Reynolds number, the basic flow is determined numerically using a boundary-layer approximation (as described in [I]). Large Reynolds number also justifies local stability analysis. The stability problem depends on three nondimensional physical parameters: the Reynolds number, Re, the rotation rate, S, and the axial location, Z. Modal analysis introduces two additional parameters: namely α, the axial wavenumber, and m, which is an integer whose value identifies the azimuthal Fourier component of the mode. The local stability equations are solved numerically to obtain the complex frequency $\omega = \omega_r + \mathrm{i}\omega_i$ of modes via solution of a matrix eigenvalue problem. The numerics were checked by studying the sensitivity of the results to variations of the numerical parameters of the problem and also by comparison with the few results available in the literature. The eigenspectrum consists of a discrete part and a numerical approximation (many closely spaced eigenvalues lying along a curve in the complex ω plane) of the continuous spectrum. The latter lies in $\omega_i < 0$ and thus represents a decaying contribution which is unimportant from a stability point of view. Discrete eigenvalues in $\omega_i > 0$ represent growing modes and are symptomatic of instability. Let $\omega_i^{\max}$ be the maximum growth rate, where only discrete eigenvalues contribute and the maximum is taken over α and m. If $\omega_i^{\max} > 0$, the flow is unstable for the given values of Re, S and Z. This allows the determination of the stability boundary in physical-parameter space. The most important results of the paper consist of critical curves representing this boundary in the Z-Re plane for different values of S (see figures 6.9–6.13).

An important conclusion of the paper is that flow stability is surprisingly sensitive to small amounts of rotation. This is apparent in figures 6.6 and 6.9(a) and is further quantified by the

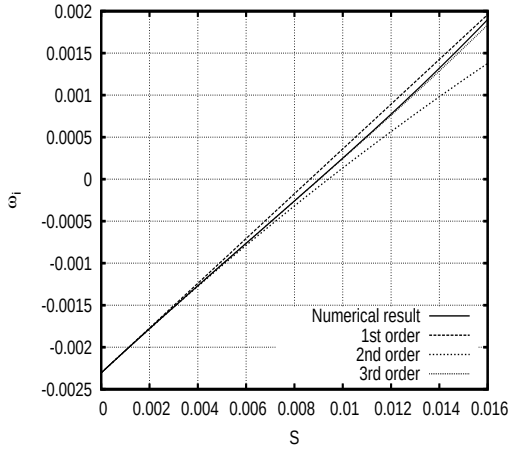

Figure 6.14: Comparison of the growth rate of the most unstable mode obtained from the full numerical calculation and perturbation theory of different orders: $m = 1, Z = 1, \mathrm{Re} = 2000, \alpha = 0.1$.

perturbation analysis of section 6.4.3. It is the consequence of a nearly neutral mode for $S = 0$ which controls stability at small S. Even a small amount of rotation can produce a sufficient perturbation that ω crosses the real axis and flow stability/instability switches for the given values of Re and Z. Rotation is destabilizing for small S, i.e. the critical Reynolds number decreases for fixed Z as S is increased.

As is apparent from figure 6.9a, in the absence of rotation the flow is stable beyond a certain value of Z (close to 0.8) and also below a Re threshold (close to 1060). No such constraints on instability apply when rotation is added. As for $S = 0$, the critical Reynolds number goes to infinity at small Z, but, for nonzero S, it approaches zero as $Z \to \infty$. Thus, as in the non-rotating case, the flow is stable at sufficiently small Z, but, with rotation, it is unstable at large enough downstream distances.

Between small and large Z there is at least one boundary separating stable/unstable portions of the flow. The simplest case is when the critical Reynolds number is a monotonic decreasing function of Z. There is then a single stability boundary in Z, below which the flow is stable, and above which it is unstable. On the other hand, a non-monotonic critical curve implies the possibility, dependent on Re, of more than one stability boundary in Z. We found that the critical curve was monotonic for S between about 0.0045 and 5.

As noted above, rotation is destabilizing at small S. This was found to persist up to about $S = 2.5$, but beyond that there were cases for which the critical Reynolds number increases with increasing S at fixed Z. Even above this threshold, the destabilizing trend continues for Z below about 3 and at sufficiently large values of Z. Destabilization by rotation can thus be considered as the norm.

Finally, the limit of large Z was also examined. We found that the critical Reynolds number has the asymptotic expansion $\mathrm{Re} \sim Z^{-1/2}(A \ln Z + B)$, where the factor A has the same value for all S and B is a decreasing function of S. The expansion is consistent with the earlier statement that critical Re goes to zero as $Z \to \infty$, while decreasing B means that rotation destabilizes the flow at large Z, as stated above.

Chapter 7

Conclusion

This final chapter summarizes results on the basic flow around a rotating cylinder and its stability analysis. It also suggests directions for future work.

7.1 Summary of results

7.1.1 Basic flow

Chapter 5 concerned the steady, incompressible, axisymmetric flow around a rotating cylinder. At large Reynolds number, this flow is essentially an axisymmetric boundary layer which is initially thin, but eventually grows to be comparable to and then larger than the cylinder radius. The boundary layer evolves slowly in the streamwise direction in comparison to the radial direction, leading to a separation of length scales. This in turn, means that certain terms in the Navier–Stokes equations can be neglected, yielding the boundary-layer equations, which are used to calculate the basic flow. Because we want to study the flow at distances for which the boundary-layer thickness is comparable to the cylinder radius, curvature and centrifugal terms are significant at leading order and must be retained. The problem depends on two non-dimensional parameters: Reynolds number (Re) and rotation rate (S). As usual, Re compares inertial forces to viscous forces, while S is defined as the ratio of the rotational velocity on the cylinder to the free-stream velocity. Using the scaled axial variable $Z = z/\mathrm{Re}$ (with z non-dimensionalized by the cylinder radius), Re disappears from the problem, leaving S as the only control parameter.

The limit $Z \to 0$ corresponds to the Blasius flow with an additional transverse velocity component. This flow is used as an inlet condition for integration of the boundary-layer equations in Z. The flow was numerically computed for a range of values of Z and S using Chebyshev collocation in the radial coordinate and second-order, finite-difference marching in Z. As Z increases, the streamwise velocity profile ($U_z(r)$) deviates from the Blasius profile due to the combined effects of cylinder curvature and rotation.

As S is increased, the centrifugal force generated by rotation also increases. The centrifugal term induces a radial pressure gradient through the radial momentum equation. This causes an axial pressure gradient in the boundary layer, even though the pressure is constant in the outer flow. When S is sufficiently large, the axial pressure gradient is large enough that it yields a wall jet over a certain range of Z. The non-monotonic behaviour of the velocity profile observed by Petrov [1976] at large value of S near the inlet is indeed this wall-jet flow. The wall jet appears first at S of 4.15 and $Z = 0.87$. Increasing S leads to strengthening of the wall jet, i.e. the maximum value of $U_z(r)$ increases. The range of Z for which there is a wall jet also widens as S

is increased.

The basic-flow solution at large values of Z was obtained using an asymptotic expansion in inverse powers of $\log Z$. These results extend the asymptotic analysis of the non-rotating case by Glauert & Lighthill [1955] to include rotation. Perhaps surprisingly, the large-Z analysis shows that U_z, U_r are decoupled from U_θ, P at all orders. In particular, the asymptotic expansion of U_z and U_r are as in the non-rotating case. Thus, no matter how large S is, the wall jet is absent at large enough Z.

The limit of large S was also investigated by introducing scaled variables appropriate in this limit. At leading order, we find that $U_z(r)$ represents an axial wall jet whose strength is maximal around $Z = 0.5$ and decreases as Z increases to larger values. The limit of large S describes a purely rotating flow (without an axial flow). The limit $S \to \infty$ can be thought of as a rotating cylinder without incident flow from upstream. Thus, the asymptotic results show that even a purely rotating cylinder develops an axial wall jet which first strengthens and then eventually weakens as Z increases.

We also found that the presence of a nose has an effect on the flow only when z is $O(1)$ or less. Thus, the shape of the nose effects the boundary-layer flow only in a relatively small region close to the inlet. As the experimental results of Kegelman *et al.* [1983] are within this region (z around 0.98), the instability modes observed in their experiments are likely affected by the shape of the nose. On the other hand, the boundary-layer development for $Z = O(1)$ and larger is unaffected by the nose geometry. This is a result of the parabolic nature of the boundary-layer equations, which forget the initial conditions, becoming less and less sensitive to these conditions as z increases.

7.1.2 Linear stability analysis

Following the detailed study of the steady boundary-layer flow around a rotating cylinder, chapter 6 concerned linear stability analysis using the boundary-layer solution as the basic flow. Large Re justifies the use of a local approximation since the basic flow has streamwise evolution on a scale much longer than the boundary-layer thickness. The linearized local stability problem depends on Re, S and Z, where Z becomes a control parameter following local approximation. Thus, the basic-flow profiles at fixed Z are used, and the stability of the resulting homogeneous flow is studied. A normal-mode decomposition leads to an eigenvalue problem for ω, the complex modal frequency, with parameters α and m, the axial and azimuthal wavenumbers. If the imaginary part of ω (ω_i), known as temporal growth rate, is positive then the mode grows, and the flow is unstable.

An important result is the set of critical curves which separate the unstable region from the stable region in the (Z, Re) plane. The critical curve for a given value of S represents the contour of maximum $\omega_i = 0$ equal to zero, where the maximization is over all α, m and all the eigenvalues. For $S = 0$, the critical curve is bounded in Z: the unstable region is limited to $Z < 0.81$ and the flow is stable for all $Z > 0.81$, and all values of Re. Critical curves for low values of rotation rate, $S < 0.001$, have been found to be highly sensitive to rotation rate. This phenomenon has been attributed to the existence of a nearly neutral mode in the non-rotating case. Rotation acts as a destabilizing mechanism, and a small amount of rotation is sufficient to destabilize such modes, leading to drastic changes in the critical curves for small rotation rates (say $S < 0.001$). Through this mechanism, the introduction of small rotation strongly destabilizes the flow in the range $Z > 0.81$, which is stable in the absence of rotation. This effect was further quantified using a perturbation analysis for small S.

At large Z, we observed that the critical Re tends to zero asymptotically for all non-zero values of S. As Z increases, the critical Re tends to zero in a monotonic way for $0.0045 < S < 5$,

and in a non-monotonic manner for $S < 0.0045$ and $S > 5$. A monotonically decreasing critical curve means that, for a given Re, the flow is stable at small Z, and undergoes a single transition to instability as Z increases. On the other hand, non-monotonic critical curves imply that, for a given Re, the flow can have several regions of stability separated by regions of instability as Z increases. Note that the value of S around 5 for the reappearance of non-monotonicity is not far from the value of S for the appearance of a wall jet in the basic flow. However, we observed that the range of Z where non-monotonicity occurs is beyond the range of Z for the wall jet. Thus, surprisingly, we do not observe any significant impact on the stability characteristics when the wall jet appears in the basic flow.

Rotation has a clear destabilizing effect on the flow for all values of $S < 2.5$: the critical Re decreases monotonically on increasing S at every Z. However, for $S > 2.5$, increasing S is found to increase critical Re for a certain range of values of Z. Nonetheless, for values of Z above this range, increasing S is destabilizing. Thus, one may say that rotation has an overall destabilizing effect on the flow.

On examining the critical curves at larger Z (Z up to 100000), we observed that the critical Re depends on Z as $\ln Z/Z^{1/2}$. This is consistent with the earlier statement that the critical Re tends to zero as Z increases, so the flow is always unstable at sufficiently large Z for any given Re and $S > 0$.

7.2 Suggestions for future work

7.2.1 Experimental work

As already pointed out in chapter 1, there have been few experimental studies of the flow around a rotating cylinder. The results of Kegelman *et al.* [1983] are affected by the shape of the nose as the length of the cylindrical section is not sufficiently long (z being of $O(1)$) for the nose effects to be neglected. Thus, it would be interesting to conduct an experiment with a longer cylinder. It would also be interesting to use experimental Reynolds numbers in the range studied here (rather than much higher ones considered by Kegelman *et al.* [1983]). The experimentally observed critical Reynolds number could then be compared with the ones computed here.

Similarly, velocity and pressure profiles could be compared with the basic-flow solution in the stable region. It would be interesting to conduct experiments for $S > 4.2$, to observe wall-jet behaviour in the U_z velocity profile.

7.2.2 Inviscid analysis

One of the limits that has not been addressed in this thesis is the limit $\mathrm{Re} = \infty$ of the linear-stability problem, also known as inviscid analysis. The Blasius boundary layer is known to be inviscidly stable, a consequence of Rayleigh's criterion. Vinod [2005] obtained such a criterion for the non-rotating cylinder and showed that the flow is inviscidly unstable. However, at present there are no such criterion or inviscid numerical results for the rotating-cylinder case.

Howard & Gupta [1962] carried out the inviscid analysis of a vortex flow with an axial component and concluded that a criterion for stability cannot be inferred from the inviscid equations. As the stability equations of the rotating cylinder have the same form as such a vortex flow, their inference is applicable to the present problem. Thus, one would have to resort to numerical techniques to understand the inviscid behaviour for the rotating case.

The inviscid equations have singularities known as critical layers. In the Blasius boundary layer problem, such critical layers lead to viscous instabilities at large but finite Reynolds number (see Drazin [2002]). As the stability equations for the cylinder problem are similar to those of

vortex flow, the locations of critical layers can be obtained by solving $\omega - \alpha\bar{U}_z(r) - (m\bar{U}_\theta(r)/r) = 0$ for r (see Le Dizès [2004] for details). The inviscid equations would have to be carefully solved to avoid numerical integration through critical points. We have performed some preliminary calculations for a few large values of Re to verify that near singularities are indeed present in the viscous eigenfunctions at locations that correspond to critical layers.

7.2.3 Absolute stability analysis

Having studied temporal stability, it seems a logical next step to conduct a spatio-temporal analysis (discussed in chapter 3) of the rotating-cylinder flow. We have already obtained some preliminary results on the absolute stability of the flow using the cusp-map method (see Kupfer *et al.* [1987]) for the case of azimuthal wavenumber $m = 1$. No instance of absolute instability was found for the range of parameters (Re up to 10000, Z up to 50 and S up to 5) covered. Although this reduces the likelihood of absolute instability in the flow, it does not completely exclude the possibility of it. It would be interesting to continue the analysis for higher values of m and for values of the remaining parameters larger than those covered so far, to check if the flow becomes absolutely unstable.

The absolute/convective nature of the flow can also be studied using Direct Numerical Simulation (DNS) method (e.g. Delbende *et al.* [1998]). The steady flow is computed using DNS and the flow is numerically perturbed (linearised DNS of the perturbation equations). The resulting wavepacket behaviour is studied to understand whether the flow is convectively/absolutely unstable. The physical and modal parameters corresponding to the absolute instability, if any, can be recovered from the DNS results. If an instance of absolute instability is observed, the normal-mode parameters corresponding to this could then be used as a starting point to characterize the region of absolute instability in control-parameter space using faster methods such as the cusp-map method.

7.2.4 Transient growth

In the present work we have studied the temporal stability of the flow based on analysis of the eigenvalues. Such a spectral analysis only describes the large-time behaviour of the perturbation. However, spectral analysis alone may not fully capture the dynamics of the disturbances, as the stability equations have the potential to exhibit short-term growth followed by exponential decay. This phenomenon is known as transient growth, and is attributed to the non-normality of the eigenvectors (see Schmid & Henningson [2001] for details). If the transient growth is large enough, nonlinear effects might become significant, leading to a different path to turbulence known as bypass transition. The Blasius boundary layer is known to exhibit transient growth, strongly hinting that the rotating cylinder has a potential to exhibit the same. As the transient-growth analysis is based on reformulating the linear stability equations as an initial-value problem, and as the mathematical techniques required for such an analysis are well-known, it should be easy to numerically implement transient-growth analysis based on the present work.

Rather than looking at the transient growth in the temporal framework, spatial transient growth analysis (see e.g. Schmid *et al.* [1994], Tumin & Reshotko [2001]) might be undertaken. Such analyses focus on the spatial evolution of the perturbation, and the possibility of short-range growth due to non-normality of the eigenvectors.

7.2.5 Nonlinear stability

All the previous suggestions for future work are based on linear-stability theory. Linear theory is applicable only when the disturbances are sufficiently small. When the magnitude of the per-

turbation becomes sufficiently large, as it inevitably does when instability occurs, the nonlinear terms can no longer be neglected. When the full nonlinear equations are considered, the wave-like disturbances are no longer independent but interact with each other leading to more complicated evolution of the disturbance.

Two approaches to nonlinear stability analysis suggest themselves. In the first, the local approximation of a basic flow which is homogeneous in z is retained, while the nonlinear perturbation equations are solved using DNS. Starting from the unstable linear regime, the growth of a mode can be followed as it becomes affected by nonlinearity, for different Re, S and Z. One could also study the effects of starting the calculation with a finite-amplitude disturbance and different types of initial spatial distribution for the perturbation. The basic-flow profile could either be calculated using the boundary-layer approximation or from the full steady, axisymmetric Navier–Stokes equations. This would quantify the errors due to the boundary-layer approximation of the basic flow and could also be used with the linearized perturbation equations and modal analysis.

In the second approach, the local approximation would be dropped and the full Navier–Stokes equations used to simulate the total flow. Different perturbations could be introduced via the incident flow or the initial conditions, and the spatio-temporal evolution studied. Of course, such DNS would incur much longer computer runs and storage requirements than the methods used in the present work.

Bibliography

G. K. Batchelor. *An Introduction to Fluid Dynamics*. Cambridge University Press, 1967.

T. Cebeci. Laminar and turbulent incompressible boundary layers on slender bodies of revolution in axial flow. *Journal of Basic Engineering*, 92:545–550, 1970.

I. Delbende, J. M. Chomaz, and P. Huerre. Absolute/convective instabilities in the Batchelor vortex: a numerical study of the linear impulse response. *Journal of Fluid Mechanics*, 355: 229–254, 1998.

S. Derebail Muralidhar, B. Pier, and J. F. Scott. Instability of flow around a rotating, semi-infinite cylinder. *Physical Review Fluids*, 1:053602, 2016a.

S. Derebail Muralidhar, B. Pier, J. F. Scott, and R. Govindarajan. Flow around a rotating, semi-infinite cylinder in an axial stream. *Proceedings of the Royal Society of London A: Mathematical, Physical and Engineering Sciences*, 472:20150850, 2016b.

P. G. Drazin. *Introduction to Hydrodynamic Stability*. Cambridge University Press, 2002.

S. J. Garrett and N. Peake. The absolute instability of the boundary layer on a rotating cone. *European Journal of Mechanics B/Fluids*, 26:344–353, 2007.

S. J. Garrett, Z. Hussain, and S. O. Stephen. Boundary-layer transition on broad cones rotating in an imposed axial flow. *AIAA Journal*, 48:1184–1194, 2010.

M. B. Glauert. The wall jet. *Journal of Fluid Mechanics*, 1:625–643, 1956.

M. B. Glauert and M. J. Lighthill. The axisymmetric boundary layer on a long thin cylinder. *Proceedings of the Royal Society of London. Series A. Mathematical and Physical Sciences*, 230:188–203, 1955.

H. Görtler. Decay of swirl in an axially symmetrical jet, far from the orifice. *Revista matemática hispanoamericana*, 14:143–178, 1954.

M. G. Hall. Vortex breakdown. *Annual Review of Fluid Mechanics*, 4:195–218, 1972.

M. A. Herrada, C. Del Pino, and R. Fernandez-Feria. Stability of the boundary layer flow on a long thin rotating cylinder. *Physics of Fluids*, 20:034105, 2008.

L. N. Howard and A. S. Gupta. On the hydrodynamic and hydromagnetic stability of swirling flows. *Journal of Fluid Mechanics*, 14:463–476, 1962.

P. Huerre and P. A. Monkewitz. Local and global instabilities in spatially developing flows. *Annual review of fluid mechanics*, 22:473–537, 1990.

N. A. Jaffe and T. T. Okamura. The transverse curvature effect on the incompressible laminar boundary layer for longitudinal flow over a cylinder. *Zeitschrift für angewandte Mathematik und Physik*, 19:564–574, 1968.

R. Jordinson. The flat plate boundary layer. Part 1. Numerical integration of the Orr–Sommerfeld equation. *Journal of Fluid Mechanics*, 43:801–811, 1970.

K. H. Kao and C. Y. Chow. Stability of the boundary layer on a spinning semi-infinite circular cylinder. *Journal of Spacecraft and Rockets*, 28:284–291, 1991.

J. T. Kegelman, R. C. Nelson, and T. J. Mueller. The boundary layer on an axisymmetric body with and without spin. *AIAA Journal*, 21:1485–1491, 1983.

H. B. Keller and T. Cebeci. Accurate numerical methods for boundary-layer flows. II: Two dimensional turbulent flows. *AIAA Journal*, 10:1193–1199, 1972.

H. R. Kelly. A note on the laminar boundary layer on a circular cylinder in axial incompressible flow. *Journal of the Aeronautical Sciences (Institute of the Aeronautical Sciences)*, 21, 1954.

K. Kupfer, A. Bers, and A. K. Ram. The cusp map in the complex-frequency plane for absolute instabilities. *Physics of Fluids*, 30:3075–3082, 1987.

S. Le Dizès. Viscous critical-layer analysis of vortex normal modes. *Studies in Applied Mathematics*, 112:315–332, 2004.

C. Leclercq. *Instabilités convectives et absolues dans l'écoulement de Taylor–Couette–Poiseuille excentrique*. PhD thesis, École centrale de Lyon, 2013.

R. J. Lingwood. Absolute instability of the boundary layer on a rotating disk. *Journal of Fluid Mechanics*, 299:17–33, 1995.

L. G. Loitsyanskii. The spreading of a swirling jet in unbounded space, filled with the same fluid. *Prikladnaya Matematika i Mekhanika*, 17:3–16, 1953.

L. M. Mack. A numerical study of the temporal eigenvalue spectrum of the Blasius boundary layer. *Journal of Fluid Mechanics*, 73:497–520, 1976.

W. Mangler. Boundary layers on bodies of revolution in symmetrical flow. *Berichte Aerodynamischen Versuchanstatt Göttingen*, 1945.

T. Miyazaki, K. Mukaiyama, Y. Komori, K. Okawa, S. Taguchi, and H. Sugiura. Aerodynamic properties of an archery arrow. *Sports Engineering*, 16:43–54, 2013.

T. J. Pedley. On the instability of viscous flow in a rapidly rotating pipe. *Journal of Fluid Mechanics*, 35:97–115, 1969.

G. V. Petrov. Boundary layer on a rotating cylinder in axial flow. *Journal of Applied Mechanics and Technical Physics*, 17:506–510, 1976.

B. Pier. Primary crossflow vortices, secondary absolute instabilities and their control in the rotating-disk boundary layer. *Journal of Engineering Mathematics*, 57:237–251, 2007.

B. Pier. Periodic and quasiperiodic vortex shedding in the wake of a rotating sphere. *Journal of Fluids and Structures*, 41:43–50, 2013.

L. Prandtl. Über Flüssigkeitsbewegung bei sehr kleiner Reibung. In *Verhandlungen III Internationalen Mathematiker-Kongresses*, pages 484–491, 1904.

H. L. Reed and W. S. Saric. Stability of three-dimensional boundary layers. *Annual Review of Fluid Mechanics*, 21:235–284, 1989.

H. L. Reed, W. S. Saric, and D. Arnal. Linear stability theory applied to boundary layers. *Annual review of Fluid Mechanics*, 28:389–428, 1996.

O. Reynolds. An experimental investigation of the circumstances which determine whether the motion of water shall be direct or sinuous, and of the law of resistance in parallel channels. *Proceedings of the Royal Society of London*, 35:84–99, 1883.

L. Rosenhead. *Laminar Boundary Layers*. Dover books on engineering and engineering physics. Dover Publications, 1963.

W. S. Saric, H. L. Reed, and E. B. White. Stability and transition of three-dimensional boundary layers. *Annual Review of Fluid Mechanics*, 35:413–440, 2003.

H. Sawada, K. Umezawa, T. Yokozeki, A. Watanabe, and T. Otsu. Wind tunnel test of Japanese arrows with the JAXA 60-cm magnetic suspension and balance system. *Experiments in Fluids*, 53:451–466, 2012.

S. P. Sawchuk and M. Zamir. Boundary layer on a circular cylinder in axial flow. *International Journal of Heat and Fluid flow*, 13:184–188, 1992.

H. Schlichting. Berechnung der Anfachung kleiner Störungen bei der Plattenströmung. *Zeitschrift für Angewandte Mathematik und Mechanik*, 13:171–174, 1933.

H. Schlichting. Laminar flow about a rotating body of revolution in an axial airstream. *Ingenieur-Archives*, 21:227–244, 1956.

H. Schlichting. *Boundary layer theory*. McGraw-Hill, 1979.

P. J. Schmid and D. S. Henningson. *Stability and Transition in Shear Flows*. Applied Mathematical Sciences. Springer, 2001.

P. J. Schmid, A. Lundbladh, and D. S. Henningson. Spatial evolution of disturbances in plane Poiseuille flow. In *Transition, Turbulence and Combustion: Volume I Transition*, pages 287–297. Springer Netherlands, 1994.

G. B. Schubauer and H. K. Skramstad. Laminar-boundary-layer oscillations and transition on a flat plate. *NASA TR-909*, 1948.

J. F. Scott. Moffatt-type flows in a trihedral cone. *Journal of Fluid Mechanics*, 725:446–461, 2013.

R. A. Seban and R. Bond. Skin-friction and heat-transfer characteristics of a laminar boundary layer on a cylinder in axial incompressible flow. *Journal of the Aeronautical Sciences (Institute of the Aeronautical Sciences)*, 18:671–675, 1951.

W. Tollmien. Über die Entstehung der Turbulenz. 1. Mitteilung. *Nachrichten von der Gesellschaft der Wissenschaften zu Göttingen, Mathematisch-Physikalische Klasse*, 1929:21–44, 1928.

A. Tumin and E. Reshotko. Spatial theory of optimal disturbances in boundary layers. *Physics of Fluids*, 13:2097–2104, 2001.

O. R. Tutty, W. G. Price, and A. T. Parsons. Boundary layer flow on a long thin cylinder. *Physics of Fluids*, 14:628, 2002.

N. Vinod. *Stability and transition in boundary layers: Effect of transverse curvature and pressure gradient*. PhD thesis, Jawaharlal Nehru Centre for Advanced Scientific Research, 2005.

N. Vinod and R. Govindarajan. Secondary instabilities in incompressible axisymmetric boundary layers: Effect of transverse curvature. *Journal of Fluids Engineering, Transactions of the ASME*, 134:024503, 2012.

H. Werle, 1970. URL `http://www.onera.fr/en/dmae/intrinsic-stability-of-flows`.

dernière page de la thèse

AUTORISATION DE SOUTENANCE

Vu les dispositions de l'arrêté du 7 août 2006,

Vu la demande du Directeur de Thèse

Monsieur J. SCOTT et Monsieur B. PIER

et les rapports de

M. N. PEAKE
Professeur - DAMTP - Cambridge University - Wilberforce Road - Cambridge CB3 0WA
Royaume-Uni

et de

M. F. GALLAIRE
Professeur - LMFI - Ecole Polytechnique Fédérale de Lausanne - Station 9 - CH-1015 Lausanne
Suisse

Monsieur DEREBAIL MURALIDHAR Srikanth

est autorisé à soutenir une thèse pour l'obtention du grade de **DOCTEUR**

Ecole doctorale MECANIQUE, ENERGETIQUE, GENIE CIVIL ET ACOUSTIQUE

Fait à Ecully, le 2 novembre 2016

P/Le directeur de l'E.C.L.
La directrice des Etudes

ECOLE CENTRALE DE LYON
Service Scolarité
ECULLY

M-A. GALLAND